



## AN ABSTRACT OF THE DISSERTATION OF

Ehsan Shams Sobhani for the degree of Doctor of Philosophy in  
Mechanical Engineering presented on November 13, 2009.

Title: Numerical Simulation of Cavitating Bubble-Laden Turbulent Flows

Abstract approved: \_\_\_\_\_

Sourabh V. Apte

Many engineering devices and propulsion systems suffer from undesirable effects of cavitation; such as degradation in the efficiency of pumps and turbines, generation of noise and vibration on ship propeller, increased drag and erosion of propeller blade, etc. In spite of decades of research on this problem, detailed study of cavitation physics is still a technical challenge for the current experimental and numerical approaches. Further development of robust and accurate numerical methods for cavitating flow simulation, is the basis of this research.

The main objective of this research is to investigate traveling bubble cavitation in turbulent flows. Variable density Navier-Stokes equations are solved in an unstructured grid finite volume solver. Large Eddy Simulation technique with dynamic Smagorinsky subgrid model is used for turbulence modeling. Bubble cavitation is modeled in a Lagrangian framework with subgrid models for forces acting on bubbles. Bubble size variation is modeled using local flow field hydrodynamic pressure for solving Rayleigh-Plesset equation. An adaptive time stepping method is devised for the efficient solution of this highly non-linear equation. Turbulent flow over an open cavity is reproduced numerically from the experimental work by [Liu and Katz, *PoF*, 08]. Flow statistics agreed very well to those of experiment. Cavitation inception was studied using two different models: (i) discrete bubble model, and (ii) scalar transport model. Severe cavitation was predicted near on top of the trailing edge for cavitation index of  $\sigma < 0.4$ , in agreement to experiments. Dynamics of inception from both models are in good agreement with experiment. A

parametric study is performed to study effect of initial gas nuclei size and cavitation number. Cavitation inception is found to occur on top of the trailing edge, which is in agreement with experiment. Inception happens in different pressure coefficient ( $C_p$ ) values expected from the classical inception criterion. A PDF analysis on the bubble distribution shows that the larger bubbles are more susceptible to cavitation. Most of the cavitating bubbles are in the regions of negative  $C_p$ .

©Copyright by Ehsan Shams Sobhani  
November 13, 2009  
All Rights Reserved

# Numerical Simulation of Cavitating Bubble-Laden Turbulent Flows

by

Ehsan Shams Sobhani

A DISSERTATION

submitted to

Oregon State University

in partial fulfillment of  
the requirements for the  
degree of

Doctor of Philosophy

Presented November 13, 2009

Commencement June 2010

Doctor of Philosophy dissertation of Ehsan Shams Sobhani presented on  
November 13, 2009.

APPROVED:

---

Major Professor, representing Mechanical Engineering

---

Head of the School of Mechanical, Industrial, and Manufacturing Engineering

---

Dean of the Graduate School

I understand that my dissertation will become part of the permanent collection of Oregon State University libraries. My signature below authorizes release of my dissertation to any reader upon request.

---

Ehsan Shams Sobhani, Author

## ACKNOWLEDGEMENTS

The financial support of this work was provided by Office of Naval Research (ONR) under grant number N000140610697. The program manager is Dr. Ki-Han Kim. Computer resources were provided by San Diego Super Computing Center (SDSC), Texas Advanced Computing Center (TACC), and local computing cluster at Oregon State University.

This work has received major benefits from useful discussions and experimental data provided by Prof. Joseph Katz and Dr. Xiaofeng Liu from Johns Hopkins University. It has also benefited from discussions with other graduate students in the Computational Flow Physics Lab and Thermal Fluid Science group at OSU, among them Justin Finn, Mathieu Martin, Andrew Cihonski, Daniel Peterson, Stephen Snider, Daniel Morse, and Benjamin T. Dickinson.

I would especially like to thank my advisor, Dr. Sourabh V. Apte, for guiding me through research with excellent patience and for the given encouragements. I would also like to thank my committee members Prof. James Liburdy, Dr. Deborah Pence, Dr. Vinod Narayanan, and Dr. John Nash for their suggestions and reviewing this work.

## DEDICATION

To my wife Negar and my parents.

# TABLE OF CONTENTS

	<u>Page</u>
1 Introduction	1
1.1 Motivation and Objective . . . . .	1
1.2 What is cavitation? . . . . .	2
1.3 Physics of Cavitation . . . . .	2
1.4 Cavitation Studies . . . . .	6
1.5 Numerical Efforts . . . . .	7
2 Discrete Bubble Model (DBM) for Cavitation	9
2.1 Fluid Phase Equations . . . . .	9
2.2 Disperse Phase Equations . . . . .	10
2.3 Discretization of Fluid Phase Equation . . . . .	12
2.4 Numerical Algorithm . . . . .	14
2.4.1 Disperse-Phase Solution . . . . .	14
2.4.2 Fluid-Phase Solution . . . . .	20
3 Verification Test Cases for Bubble-laden Flows	24
3.1 Oscillating Bubbles . . . . .	24
3.2 Bubble Dynamics Under Imposed Pressure Variations: . . . . .	26
3.3 Terminal Velocity Test . . . . .	27
3.4 Bubble Trajectory in a Line Vortex . . . . .	30
3.4.1 Motion Analysis of a Single Bubble . . . . .	30
3.4.2 Numerical Results . . . . .	33
3.4.3 Non-Cavitating Bubble . . . . .	34
3.4.4 Cavitating Bubble . . . . .	38
4 Bubble Interactions with Vortical Flows	40
4.1 Taylor-Green vortex . . . . .	40
4.2 Rankine Vortex . . . . .	44
4.2.1 Numerical Simulations of Bubble-Laden Rankine Vortex . . . . .	44
4.2.2 Effect of $St$ and $g^*$ on the bubble accumulation with one-way coupling . . . . .	47
4.2.3 Coupling Effect on Bubble Concentration . . . . .	48
4.2.4 Coupling Effect on Pressure . . . . .	53

## TABLE OF CONTENTS (Continued)

	<u>Page</u>
4.2.5 Coupling Effect on flow Vorticity . . . . .	54
4.3 Summary and Conclusions . . . . .	57
5 Cavitation Inception in a Turbulent Flow Over an Open Cavity	59
5.1 Introduction . . . . .	59
5.2 Turbulent Channel Flow . . . . .	60
5.3 Numerical Setup for Flow Over Cavity . . . . .	61
5.3.1 Boundary Conditions . . . . .	64
5.4 Flow Velocity Statistics . . . . .	66
5.4.1 Leading Edge . . . . .	68
5.4.2 Shear Layer . . . . .	71
5.4.3 Trailing Edge . . . . .	71
5.5 Pressure Distribution . . . . .	78
5.6 Instantaneous Flow Field . . . . .	83
5.7 Cavitation Inception . . . . .	83
5.7.1 Scalar Transport Model . . . . .	85
5.7.2 Discrete Bubble Model . . . . .	87
5.7.3 Bubble Trajectories . . . . .	94
5.7.4 Data Sampling . . . . .	94
5.7.5 Effect of Cavitation Index . . . . .	96
5.7.6 Effect of Initial Bubble Size . . . . .	99
5.7.7 Sampling Results Based on Growth Ratio . . . . .	99
5.8 Scalar Transport Model versus Bubble Cavitation Model . . . . .	102
5.9 Summary and Conclusion . . . . .	104
6 Summary, Conclusions and Future Directions	108
6.1 Summary . . . . .	108
6.2 Conclusions . . . . .	109
6.3 Future Directions . . . . .	111
Literature Cited	113

## LIST OF FIGURES

Figure	Page
1.1 Traveling bubble cavitation on a NACA 4412 hydrofoil, showing traveling bubble cavitation and different scales and forms of cavitation (from water tunnel tests by Kermeen (1956)). . . . .	4
1.2 Schematic of different bubble sizes near a solid wall on a computational grid. . . . .	5
2.1 Schematic of the grid stencil: (a) time staggering of variables, (b) velocity ( $u_i$ ) and pressure fields ( $p$ ) are co-located at the control volume center, $u_N$ is the face-normal velocity, (c) control volume and face connectivity. . . . .	12
3.1 Flow developed by an oscillating bubble: (a) Pressure distribution caused by volume displacement around the bubble compared with analytical solution (dashed line shows the pressure field if the void fraction variations are neglected), (b) instantaneous velocity vector field due to bubble oscillations. . . . .	25
3.2 Doublet generated by bubbles oscillating in tandem. Streamlines and pressure contours (dashed line) are shown. . . . .	26
3.3 Time variation of bubble radius and $\lambda$ values for a cavitating bubble with imposed pressure variations. . . . .	28
3.4 Rising velocity of a single bubble in a liquid column from direct integration of ODE (symbols) and numerical simulation (solid line). . . . .	29
3.5 Falling velocity of a glass bead in air from direct integration of ODE (symbols) and numerical simulation (solid line). . . . .	29
3.6 Effect of Stokes number on bubble trajectory . . . . .	32
3.7 Unstructured grid for the Rankine vortex simulations (coarse grid is shown.)	33
3.8 Rankine vortex . . . . .	35
3.9 Time evolution of L2 error of the horizontal velocity component in Rankine vortex on different grid sizes . . . . .	36

## LIST OF FIGURES (Continued)

<u>Figure</u>	<u>Page</u>
3.10 Trajectory of single bubble using small (dash-dotted red line), medium (dashed green line), and large (solid blue line), in comparison to the results from direct integration of equations of motion in Rankine vortex model (solid cyan line). . . . .	36
3.11 Trajectory error for a single bubble in Rankine vortex. Grid sizes found in table 3.3. . . . .	37
3.12 Convergence of the force calculation error . . . . .	38
3.13 Trajectory of cavitating (solid line) versus non-cavitating (dashed line) bubbles in Rankine vortex . . . . .	39
4.1 Bubble concentration (normalized by maximum initial value) at the vortex center from one-way coupling (solid line), and volumetric coupling (dashed line), in comparison to one-way (squares) and two-way (circles) coupling simulation from FE07 (Ferrante and Elghobashi, 2007). . . . .	41
4.2 Flow vorticity (normalized by maximum initial value) from one-way coupling (solid line), and volumetric coupling (dashed line), in comparison to one-way (squares) and two-way (circles) coupling simulation from FE07 (Ferrante and Elghobashi, 2007). . . . .	42
4.3 Correlation between changes in fluid phase acceleration and material derivative of the bubble concentration at $t = 0.2$ ; using one-way (dashed lines) and volumetric coupling (solid lines). . . . .	43
4.4 Difference in flow pressure, using one-way (dashed line) coupling and volumetric coupling (solid line), at time $t = 0, 5$ . . . . .	43
4.5 Rankine vortex . . . . .	45
4.6 Initial distribution of bubbles around the vortex core . . . . .	46
4.7 Comparing bubble accumulation with different Stokes number at the vortex center for $St = 0.25$ (solid line), $St = 0.5$ (dashed line), and $St = 1.0$ (dash-dotted line). $n$ is number of vortex revolution, $d$ is distance to the center normalized by $a_c$ , and $C_0$ is the concentration at the center normalize by maximum initial concentration. . . . .	47

## LIST OF FIGURES (Continued)

Figure	Page
4.8 Bubble distance to the center for case G (solid line), case H (dashed line), and case I (dash-dotted line). . . . .	48
4.9 Time evolution of the bubble concentration at the vortex center (a) and radial distribution of concentration at time $n = 25$ for case C (b); with one-way (solid line), two-way (dashed line), and volumetric (dash-dotted line) coupling models. . . . .	49
4.10 Radial velocity component in the Rankine vortex generated by phase coupling effect (a) and (b), and rate of change of bubble concentration in time $D\Theta_b/Dt$ (normalized by initial concentration $\Theta_{b,0}$ and bubble response time $\tau_b$ ); showing one-way (solid line), two-way (dashed line), and volumetric (dash-dotted line) couplings. . . . .	51
4.11 Flow radial acceleration (normalized by $a_c\omega_0^2$ ) and its variation with two-way (dashed line) and volumetric (dash-dotted line) coupling. . . . .	52
4.12 Correlation between $D\Theta_b/Dt$ (contours) and $D\mathbf{u}/Dt$ vectors in case c at $n = 15$ , using volumetric coupling. . . . .	52
4.13 Radial pressure distribution with one-way (solid line), two-way (dashed line), and volumetric (dash-dotted line) coupling and the differences with one-way coupling (the curves in the middle). Pressure is normalized as $\hat{p} = (p - p_\infty)/(a_c\omega_0^2)$ . . . . .	53
4.14 Radial distribution of pressure gradient . . . . .	54
4.15 $\alpha$ , using one-way (square), two-way (delta), and volumetric (circle) coupling. . . . .	55
4.16 Time evolution of vorticity at the vortex center for case C, using one-way (solid line), two-way (dashed line), and volumetric (dash-dotted line) coupling. . . . .	56
4.17 Radial distribution of the vorticity difference (upper curves) for two-way coupling (solid line), and volumetric coupling (dashed line) with one-way coupling, along with the velocity divergence $\nabla \cdot \mathbf{u}$ , at time $n = 25$ . $\nabla \cdot \mathbf{u}$ is normalized by $\omega_0$ . . . . .	57
5.1 Schematic top and side views of the test case for flow over cavity, from the experiments by Liu and Katz (2006, 2008). . . . .	60

## LIST OF FIGURES (Continued)

Figure	Page
5.2	Flow in a periodic channel . . . . . 60
5.3	Velocity in a periodic channel flow with $Re_\tau = 395$ . . . . . 61
5.4	Computational domain and grid: (a) three-dimensional domain with Cartesian grid, (b) refined grids (dimensions shown are in mm) are used in the shear layer and near the cavity leading and trailing edges. A zoomed-in view of the grid near the trailing edge is shown in wall co-ordinates. . . 63
5.5	Comparison of vertical variations of mean and <i>rms</i> axial velocity fields in the inflow section (obtained from a stand-alone LES computation of a periodic duct flow) with the experimental data (Liu and Katz, 2008). For inlet conditions, the mean velocity from the experiment and fluctuating velocity field from the periodic duct flow are used. . . . . 65
5.6	Convergence of mean velocity, showing contour lines of time-averaged velocity components at different time snaps corresponding to 3.9 (dashed-dotted), 5.9 (dashed), and 7.5 (solid) flow-through-times, calculated based on the cavity length and free stream velocity. . . . . 67
5.7	Comparison of vertical variations of mean and <i>rms</i> of stream-wise velocity component near the leading edge with (solid lines) and without (dashed lines) inflow fluctuations with the experiment data of LK2008 (symbols). . . . . 69
5.8	Effect of grid refinement on the mean and <i>rms</i> of stream-wise flow velocity component. Shown in the figures are the results from the base (solid line), coarse (dashed line) computational grid, and experimental results (symbols). . . . . 70
5.9	Contours of flow velocity statistics on the shear layer, showing mean ( $\bar{U}/U_\infty$ and $\bar{V}/U_\infty$ ), rms ( $\sqrt{u^2}/U_\infty$ and $\sqrt{v^2}/U_\infty$ ), and Reynolds Stress ( $\overline{uv}/U_\infty^2$ ) from both LES (color contours), and experimental data (dashed contour lines) from LK2008. . . . . 73
5.10	Comparison of vertical variations of mean ( $\bar{U}/U_\infty$ ) and <i>rms</i> ( $\sqrt{u^2}/U_\infty$ ) of stream-wise velocity component and Reynolds Stress ( $\overline{uv}/U_\infty^2$ ), on the shear layer with (solid lines) and without (dashed lines) inflow fluctuations with the experiment data of LK2008 (symbols). . . . . 74

## LIST OF FIGURES (Continued)

<u>Figure</u>	<u>Page</u>
5.11 Contours of flow velocity statistics on the trailing edge, showing mean ( $\bar{U}/U_\infty$ and $\bar{V}/U_\infty$ ), rms ( $\sqrt{u'^2}/U_\infty$ and $\sqrt{v'^2}/U_\infty$ ), and Reynolds Stress ( $\overline{u'v'}/U_\infty^2$ ) from both LES (color contours), and experimental data (dashed contour lines) from LK2008. . . . .	76
5.12 Distribution of flow velocity statistics on top of the shear layer with basic grid (solid line), coarse grid (dashed line), and experimental (symbols) results. . . . .	77
5.13 Contours of mean ( $\bar{C}_p$ ) and rms ( $\sqrt{C_p'^2}$ ) of pressure coefficient near the trailing edge. Shown is the LES results (color contours) and experimental results (dashed lines) from LK2008. . . . .	79
5.14 Time-averaged contours of pressure coefficient ( $\bar{C}_p$ ) near the trailing edge.	80
5.15 Probability distribution functions for $C_p'$ at the eight probe locations (p1–p8) shown in Figure 5.14. . . . .	81
5.16 Eddy viscosity $\mu_T$ calculated by subgrid scale model . . . . .	82
5.17 Instantaneous pressure contours and stream traces (based on removing $0.5U_\infty$ from the streamwise velocity):(a) $t = 53$ ms (high pressure above the trailing edge), (b) $t = 55$ ms (low pressure above the trailing edge), (c) $t = 65$ ms, (d) $C_p(t)$ at a probe above the trailing edge ( $x/L = 1.01$ , $y/L = 0.0035$ , $z/L = 0$ ). . . . .	84
5.18 Time evolution of vapor fraction and $C_p$ just above the trailing edge at $\bar{x} = (38.0, 0.3, 0.0)$ for $\sigma_i = 0.9$ . . . . .	86
5.19 Evolution of vapor fraction ( $\phi = 1 - \Theta_\ell = 0.2$ ) above the trailing edge as predicted by the scalar transport model. Periodic growth and decay of the local vapor fraction is correlated with the variations in $C_p$ just above the trailing edge. . . . .	89
5.20 Time evolution of vapor fraction and $C_p$ just above the trailing edge at $\bar{x} = (38.1, 0.01, 0.0)$ for $\sigma_i = 0.4$ . . . . .	90
5.21 Time evolution of liquid vapor fraction ( $\phi = 1 - \Theta_\ell$ ) on the shear layer with $\sigma_i = 0.1$ from the scalar transport model. Shown in the figure are iso-surfaces of $\phi = 0.2$ (cyan), $0.4$ (light green), and $0.8$ (yellow). . . . .	91

## LIST OF FIGURES (Continued)

<u>Figure</u>	<u>Page</u>
5.22 Temporal evolution of bubble distribution (initial size 50 $\mu\text{m}$ ) on the shear layer (side view) for $\sigma_i = 0.4$ . . . . .	92
5.23 Top view of the instantaneous snapshot of bubbles above in the shear layer and near the trailing edge: (a) absolute value of outside pressure based on $\sigma_i = 0.4$ , (b) outside pressure based on $\sigma_i = 0.9$ . . . . .	93
5.24 Temporal evolution of bubble radius (normalized by initial radius) and outside pressure coefficient ( $C_p$ ) seen by the bubbles for two sample trajectories of bubbles released near the leading edge. The upstream pressure level is set based on $\sigma_i = 0.8$ for the top panel and $\sigma_i = 0.1$ for the bottom panel: (a) bubble released at $y = 0.2$ mm, (b) released at $y = 0.1$ mm from the leading edge surface. . . . .	95
5.25 Effect of cavitation index $\sigma_i$ on the PDFs and average number of bubbles ( $N_b$ ) sampled based on the growth ratio ( $d/d_{\text{initial}}$ ) and pressure coefficient $C_p$ for case C2 (triangle symbols), C4 (diamond symbols), C5 (filled circles), and C6 (filled square): (a,b) PDF of all bubbles over the region of interest; (c,d) bubbles in zone 1; (e,f) bubbles in zone 2, and (g,h) bubbles in zone 3. . . . .	98
5.26 Effect of initial bubble size on the PDFs and average number of bubbles sampled based on growth ratio ( $d/d_{\text{initial}}$ ) and pressure coefficient $C_p$ at bubble location for cases C1 (10 $\bar{\text{m}}$ square symbols), C2 (50 $\bar{\text{m}}$ triangle symbols), and C3 (100 $\bar{\text{m}}$ circle symbols): (a,b) PDF for all bubbles over the region of interest; (c,d) bubbles in zone 1; (e,f) bubbles in zone 2, and (g,h) bubbles in zone 3. . . . .	101
5.27 Average number of conditionally sampled bubbles based on pressure coefficient at bubble location for case C1 (square), C2 (triangle), and C3 (circle): (a) medium size group ( $0.8 < d/d_{\text{initial}} < 1.25$ ), (b) large size group ( $1.25 < d/d_{\text{initial}}$ ). . . . .	101
5.28 Average number of conditionally sampled bubbles for large size group ( $1.25 < d/d_{\text{initial}}$ ) based on vorticity magnitude at bubble location for case C1 (square), C2 (triangle), and C3 (circle). . . . .	102

## LIST OF FIGURES (Continued)

<u>Figure</u>		<u>Page</u>
5.29	Schematic of instantaneous comparison between cavitation prediction from scalar transport model (iso surfaces of vapor fraction) and bubble cavitation model (discrete bubbles). . . . .	103
5.30	Average expansion ratio from scalar transport model (solid lines) and bubble cavitation model (dashed line). . . . .	105

## LIST OF TABLES

<u>Table</u>		<u>Page</u>
3.1	Physical parameters and computational settings for the oscillating bubble	25
3.2	Rankine vortex configuration . . . . .	33
3.3	Grid sizes for Rankine vortex simulations . . . . .	34
4.1	Parameters in Rankine vortex flows . . . . .	46
5.1	Computational domain and grid size (+ denotes wall units) for the periodic channel (verification case). . . . .	61
5.2	Properties for flow over cavity (+ denotes wall units, $y^+ = yu_\tau/\nu$ ). . . . .	62
5.3	Cavity geometry and computational grid (+ denotes wall units, $y^+ = yu_\tau/\nu$ ). . . . .	62
5.4	Case studies to analyze cavitation inception using the Discrete Bubble Model. . . . .	89

## Nomenclature

### Roman Symbols

$A_{face}$	cv face area
$C_D$	coefficient of drag
$C_L$	coefficient of lift
$C_p$	coefficient of pressure; $C_p = (p - p_\infty)/0.5\rho_\ell U_\infty^2$
$N_b$	number of bubbles
$p$	pressure
$p_0$	reference pressure
$p_v$	vapor pressure
$R_b$	radius of bubble
$S$	surface tension
$St$	Stokes number; $St = \omega\tau_b$ in a vortex
$T$	reference time scale
$t$	time
$t^*$	non-dimensionalized time
$u'$	turbulent velocity fluctuation
$u_N$	cv face normal velocity
$V$	volume
$V_b$	volume of bubble
$V_{cv}$	volume of control volume
$\mathbf{D}$	deformation tensor
$\mathbf{f}$	inter-phase coupling force
$\mathbf{F}_D$	drag force
$\mathbf{F}_L$	lift force

$\mathbf{F}_P$	pressure gradient force acting on a bubble
$\mathbf{F}_{\dot{R}_b}$	force acting on a bubble caused by its size variation
$\mathbf{f}_{\ell \rightarrow b}$	force acting on a bubble by liquid; $\mathbf{F}_{\ell \rightarrow b} = \mathbf{F}_G + \mathbf{F}_P + \mathbf{F}_D + \mathbf{F}_L + \mathbf{F}_{AM} + \mathbf{F}_{coll} + \mathbf{F}_{\dot{R}_b}$
$\mathbf{F}_{AM}$	added mass force on a bubble
$\mathbf{f}_{b \rightarrow \ell}$	force acting on the liquid by bubbles
$\mathbf{F}_{coll}$	collision force between bubbles
$\mathbf{g}$	gravitational force per unit mass
$\mathbf{u}$	velocity vector
$\mathbf{u}_\ell$	liquid velocity vector
$\mathbf{u}_b$	bubble velocity vector
$\mathbf{x}$	coordinate vector
$\mathbf{x}_b$	position of bubble center
$\mathbf{x}_{cv}$	position of control volume center
PDF( )	Probability Density Function

### Greek Symbols

$\Delta t$	computation time step for the fluid flow
$\Delta y$	grid length in $y$ direction
$\Delta y^+$	grid length in $y$ direction and in wall units; $y^+ = yu_\tau/\nu$
$\Delta$	width of interpolation kernel
$\Gamma$	flow circulation
$\lambda_i$	$i$ th eigenvalue of a square matrix
$\mathcal{G}$	interpolation kernel
$\mu$	molecular viscosity; $\mu = \rho\nu$
$\mu_\ell$	molecular viscosity of liquid
$\mu_T$	eddy viscosity
$\mu_{eff}$	$\mu_{eff} = \mu_\ell + \mu_T$

$\nu$	kinematic viscosity
$\omega$	vorticity $\omega = \nabla \times \mathbf{u}$
$\pi$	3.14159...
$\rho$	mass density
$\rho_b$	bubble density
$\rho_\ell$	liquid density
$\rho_{cv}$	liquid density at the center of control volume
$\sigma$	cavitation index
$\tau_b$	bubble time scale based on Stokes drag model; $\tau_b = d^2/36\nu$
$\Theta_b$	bubble volume fraction
$\Theta_\ell$	liquid volume fraction

#### Other Symbols

$\frac{D}{Dt}$	material derivative $\frac{D}{Dt} = \frac{\partial}{\partial t} + \mathbf{u} \cdot \nabla$
$\nabla$	gradient operator
$\nabla \cdot$	divergence operator
$\nabla \times$	curl operator
$\nabla^2$	Laplacian operator
$\bar{u}$	time averaged flow velocity
$\dots^n$	variable $\dots$ at computation time level $n$

## Chapter 1 – Introduction

### 1.1 Motivation and Objective

Cavitation has been the subject of studies in different science and engineering problems, for more than 100 years. It may occur in any liquid handling instrument, such as turbomachinery, ship propellers, measurement devices, etc. Degrading performance of pumps, reducing the thrust of propellants, and causing undesirable noise and vibration are some of detrimental effects caused by cavitation. Whereas, controlled cavitation can be beneficial in engineering, biomedical, and chemical applications. It has been used in drag reduction on the ship hull, enhancing chemical reactions, removal of kidney stones, ultrasonic surface cleaning, and many others.

In spite of different known problems as well as benefits, cavitation physics is not completely understood. Complex phase change process, involving mass, momentum and heat transfer, as well as wide range of time and length scales are part of the complication. Different experimental, analytical, and numerical techniques have been presented for study of cavitation. Numerous efforts on studying cavitation phenomenon, have been listed in a chain of review papers by Plesset and Prosperetti (1977), Arndt (1981), Blake and Gibson (1987), Rood (1991), and Arndt (2002). They show decades of efforts to explore the cavitation physics in analytical, experimental, and more recently numerical ways.

Cavitation problems always deal with flow turbulence. Having an accurate predictive flow simulation computational tool based on Large Eddy Simulation (LES) technique is the emphasis of this work. Combining Navier-Stokes flow solver and LES capability with Lagrangian bubble tracking technique for simulation of cavitation inception complex flow geometries is the objective of this research. Most of the studies on the cavitation problem use Reynolds Averaging Navier-Stokes (RANS) RANS techniques for turbulence modeling. It has been shown that the time dependent and dynamic features of flow are not captured very well by RANS models.

The main objective of this research is to investigate traveling bubble cavitation in

turbulent flows and complex geometries. An unstructured finite volume solver is used to solve the liquid phase flow field. Governing equations account for the presence of bubbles through both momentum transfer and volumetric liquid displacement by them. Predictive capability of large eddy simulation is being employed to model unresolved scales. Discrete bubble phase is being tracked by integrating equation of motion in Lagrangian framework. Forces acting on bubbles are modeled using standard mapping techniques from Eulerian liquid framework to Lagrangian. Bubble size variation has been modeled by solution of Rayleigh-Plesset equation and using hydrodynamic pressure data. An adaptive time stepping approach is being devised to numerically solve this highly non-linear second order ODE.

## 1.2 What is cavitation?

*Cavitation* generally refers to the whole sequence of generation, expansion, and destruction of vapor in a liquid flow, due to variation in pressure, while temperature does not change significantly (Knapp et al., 1970). It is in contrast with *boiling* where vapor generation is mainly due to heat transfer and temperature rise.

Bubble growth in cavitation can be the result of both diffusive process of evaporation and expansion of dissolved gases. This growth process is often followed by a violent collapse of the bubble which is known to be the source of structural damage and noise (Blake and Gibson, 1987).

## 1.3 Physics of Cavitation

### Inception Mechanisms

Cavitation essentially takes place when the local pressure in the liquid is less than the vapor pressure (Knapp et al., 1970). Thermal effects on the inception can be neglected for liquids such as water with a large density ratio between liquid and vapor (Tseng and Shyy, 2009). For the cryogenic liquids, however, this is very different since the other physical properties such as latent heat and thermal conductivity are also important and the vapor pressure is a function of temperature.

Joseph (1995, 1998) proposed a cavitation threshold based on the total stress in a liquid  $\mathbf{T} = -p\mathbf{I} + \mathbf{S}$ , where  $p$  is pressure and  $\mathbf{S}$  is the stress associated with the liquid motion. This relies on determination of maximum tensile stress a liquid can withstand. In a pure liquid, the cavitation inception may occur in a pressure far below the vapor pressure (Rood, 1991). Effect of impurities in the liquid, such as micro bubbles or particles has been recognized in changing maximum tensile stress of liquid.

## Different Forms of Cavitation

Depending on the geometry, flow regime, cavity size and density, air/vapor content, etc., cavitation may take different forms. Cavitation can occur either on a solid boundary or in the body of liquid. It is often generated as a result of hydrodynamic pressure variations, but can also be the result of acoustic pressure, vibrations, or even laser induced thermal effects. It can be categorized into traveling or fixed (attached) cavitation, based on the temporal variation of cavity size and location.

*Traveling bubble cavitation* is one of the forms of cavitation, which has been of considerable research interest. Traveling bubble cavitation is often referred to the process of explosive growth and collapse of bubbles (cavities) due to being convected to the zones of different pressure (Brennen, 1995). The bubble collapse process has been believed to be the source of acoustic wave propagation (Blake, 1986). Bubble collapse near a solid boundary is speculated to be the origin of strong jet formation which may cause surface damages (Blake and Gibson, 1987). Ceccio and Brennen (1991) have reported a detailed experimental observation on traveling bubble cavitation near the surface of axisymmetric headforms.

Number of cavitating bubbles may increase due to decreased pressure (cavitation number) or increased number of air bubble nuclei in the flow. Figure 1.1 shows a clear example of *dense traveling bubble cavitation* reported by Kermeen (1956). It shows cavitation nuclei on the leading edge of a NACA 4412 hydrofoil. Small bubbles grow in the separation region and then collapse once the pressure increases in the reattachment. More complicated events such as bubble interactions, deformation, and split may happen as a consequence of formation of large cavitation structures.

Other reported and studied forms of cavitation near a solid wall include *cloud cavitation* (Hosangadi and Ahuja, 2005), *attached (sheet) cavitation* (Kermeen, 1956; Gopalan

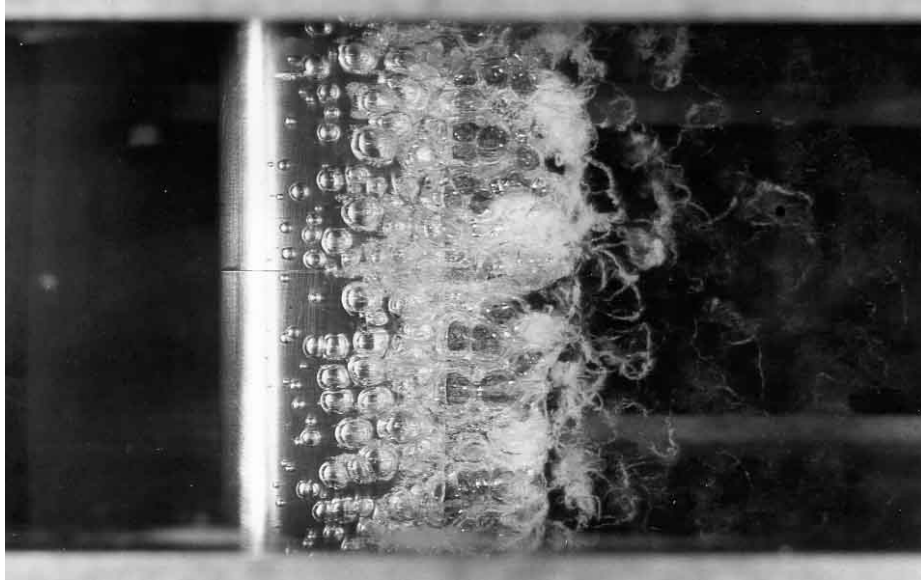


Figure 1.1: Traveling bubble cavitation on a NACA 4412 hydrofoil, showing traveling bubble cavitation and different scales and forms of cavitation (from water tunnel tests by Kermeen (1956)).

and Katz, 2000; Wang et al., 2001; Chen and Heister, 1994), and *super cavitation* (Wosnik et al., 2003; Lindau et al., 2003). Cavitation may also occur in the bulk stream and not necessarily near the solid wall. Arndt (2002) listed different forms of cavitation in the vortical flows. *Tip vortex cavitation* caused by elliptical ship propeller is an ongoing research study (Arndt et al., 1991; Hsiao and Chahine, 2004).

## Time and Length Scale

Even in its simplest form, cavitation process involves different time and length scales. Bubbles of different sizes (as shown in the figure 1.1) may appear and disappear at different rates. Transition from one length scale to another is very usual. Leger and Ceccio (1998) studied transition from sheet cavitation to clouds of bubbles on a hydrofoil. Such a problem is difficult to study with experimental or numerical techniques.

Figure 1.2 shows a typical challenge in handling different scales of the dispersed phase in a general two-phase flow simulation. It shows grid refinement near the wall

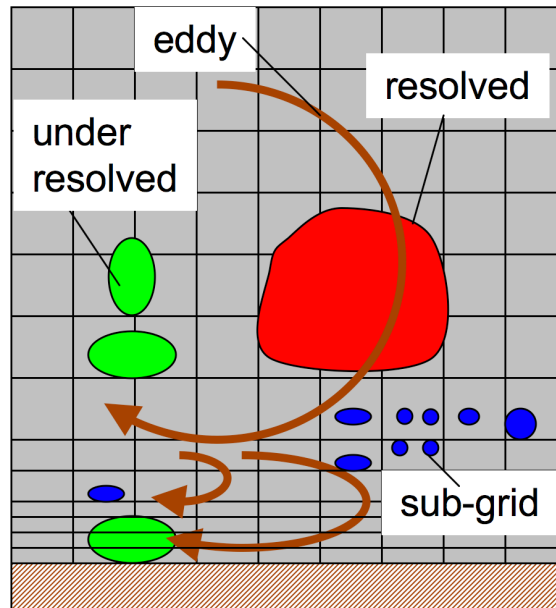


Figure 1.2: Schematic of different bubble sizes near a solid wall on a computational grid.

boundary and bubbles of different sizes on top of them. They fall into different categories of fully resolved, partially resolved, and under-resolved (sub-grid scales), based on their relative size to the local size of grid. There is not an efficient and solid numerical approach to handle this problem in the same manner, and it has to be solved using a combination of different methods.

## Interaction with Flow

An important aspect of cavitation is the feedback effects it may apply on the liquid flow. Ausoni et al. (2007) showed how cavitation on a hydrofoil can change the flow features such as the shedding frequency of von Kármán vortices.

Most of the detailed studies on cavitation inception are based on the *fully wetted flow* properties, in which the cavitation effects are neglected (Arndt, 2002). Vortex generation in the closure region of the cavity is a well known example. Gopalan et al. (2000) have shown the horseshoe vortex generation on the tail of sheet cavitation.

Belahadji et al. (1995) distinguished three types of vortices generated by cavitation

in a turbulent wake. Their observation indicates that cavitation is not a *passive agent* and it interacts with flow vortical structures.

Effect of cavitation on the flow, especially on the small scale turbulence has not been studied (Arndt, 2002) and still remains an open question.

## 1.4 Cavitation Studies

Analytical studies on cavitation start with Rayleigh (1917) who derived a spherical bubble dynamics model for bubble cavitation. The analysis is based on quasi-static equilibrium between inside and outside bubble and use of Bernoulli equation by relating pressure on the outer surface of the bubble to the far field pressure. In his model liquid surface tension and viscosity effects on the bubble dynamics were neglected. The model was later on modified by Plesset (1949) and is commonly known as Rayleigh-Plesset equation. This model does not account for the bubble deformation and stability of bubble. Other assumptions include neglecting thermal effects on the vapor content or in other words no mass transfer due to thermal condensation/vaporization.

One of the main challenges in the experimental techniques for cavitation study is the high speed nature of cavitation. The measurement techniques mainly rely on the high speed photography of the flow field (Thoroddsen et al., 2008). The other challenge is lack of direct measurement devices for example pressure and temperature in a bubble (Knapp et al., 1970).

Scaling parameters are of high importance in the experimental studies. The basic scaling parameter which is being used to describe the process is cavitation number, defined as

$$\sigma = \frac{(p_0 - p_c)}{\frac{1}{2}\rho U_0^2}, \quad (1.1)$$

where,  $P_0$  and  $U_0$  are characteristic pressure and velocity and  $P_c$  is the critical pressure at which cavitation occurs (Arndt, 1981). The critical pressure is often set to liquid vapor pressure. Interpreting scaled studies and extrapolating results to the actual geometry is not straightforward in cavitating flows (Keller, 2001; Hsiao et al., 2003).

## 1.5 Numerical Efforts

An ideal numerical method is expected to accurately predict the flow features such as unsteadiness, vortical structures, and turbulence. Compressibility of the gas phase, large density ratio between phases, different times and length scales are some of the challenging issues in the numerical techniques (Senocak and Shyy, 2004).

Various models have been proposed to incorporate the cavitation process in the flow physics. There has been a growing interest in combining Navier-Stokes equation with physics of cavitation. Wang et al. (2001) have listed different numerical attempts for study of cavitation. Numerical methods for simulation of cavitation problem fall into two major categories of interface based methods and continuum methods. In a more general sense, these are the main strategies often used in two-phase flow simulations, including cavitation problems. One may further categorize the continuum methods into subcategories based on the cavity size compared to the computational grid (see figure 1.2), into fully resolved and under-resolved schemes. A few studies from continuum based methods will be reviewed below.

Coupling transport equation model (TEM) for the vapor fraction with variable density Navier-Stokes equation (Joseph et al., 1990; Drew and Passman, 1999) is a common approach in simulating regimes such as attached cavitation (Wang et al., 2001; Senocak and Shyy, 2004). In this model the scalar transport equations are solved for the vapor fraction  $\alpha_v$  with source and sink terms that are usually functions of pressure and some empirical parameters (Senocak and Shyy, 2002a). Numerical solution may undergo severe stability problems since the inter-phase density change is usually large. Solution algorithms are either density-based with artificial compressibility and use of preconditioning techniques (Kunz et al., 2000) or pressure-based (Senocak and Shyy, 2002b). Senocak and Shyy (2004) proposed an interfacial dynamics based method to capture the baroclinic torque effect  $\nabla \frac{1}{\rho} \times \nabla P$ .

Another simulation approach is to consider the flow as a bubble-laden mixture. In this approach cavities are modeled as spherical under-resolved bubbles which may grow / collapse following Rayleigh-Plesset equation (Plesset, 1949; Plesset and Prosperetti, 1977). Bubble effects on the liquid are taken into account through momentum transfer and volumetric displacement. This technique falls into the large category of Lagrangian-Eulerian method for simulation of two-phase flows used by Druzhinin and

Elghobashi (1998); Apte et al. (2003a); Ferrante and Elghobashi (2007); Apte et al. (2008). Darmana et al. (2006) used this technique for simulation of bubble columns reactors. Cerutti et al. (2000) injected microscopic bubbles in the near field of a submerged jet to study the likelihood of cavitation inception. They used PDF analysis to locate the possible zones of cavitation. Hsiao and Pauley (1999) used bubble dynamics model for simulation of tip vortex cavitation inception on a ship propeller. They studied the sensitivity of flow field to the cavitation inception by varying cavitation number and studying bubble behavior. An advantage of this modeling technique is that subgrid scale dynamics can be more accurately captured in the Lagrangian-Eulerian calculations.

Several numerical simulations have used Reynolds Average Navier-Stokes (RANS) for the turbulence modeling in cavitating flows (Cerutti et al., 2000; Farrell, 2003; Kim et al., 2006; Hsiao and Chahine, 2008). LES has been shown to be able to capture dynamic features of the turbulent flow field more accurately and with the least dependency on the tuning parameters. Wienken et al. (2006) have recently used LES to study cavitation inception on a square cylinder.

## Chapter 2 – Discrete Bubble Model (DBM) for Cavitation

### 2.1 Fluid Phase Equations

The equations for the fluid phase are obtained by making use of the mixture theory. In this formulation, the volume occupied by the bubble in a fluid control volume is accounted for by computing the local bubble ( $\Theta_b$ ) and fluid volume fractions  $\Theta_\ell$  (such that  $\Theta_b + \Theta_\ell = 1$ ). The continuity and momentum equations account for local changes in void fractions (Joseph et al., 1990; Jackson, 1997). The continuity equation is given as:

$$\frac{\partial}{\partial t} (\rho_\ell \Theta_\ell) + \nabla \cdot (\rho_\ell \Theta_\ell \mathbf{u}_\ell) = 0. \quad (2.1)$$

Note there no summation is implied with the subscript ' $\ell$ .' The local spatio-temporal variations of bubble concentration, generate a non-divergence free velocity field,

$$\nabla \cdot \mathbf{u}_\ell = -\frac{1}{\rho_\ell \Theta_\ell} \frac{D\rho_\ell \Theta_\ell}{Dt}, \quad (2.2)$$

where  $\frac{D}{Dt}$  is the material derivative. Lagrangian quantities, such as bubble concentration, are interpolated to the Eulerian control volumes effectively, using the following interpolation function,

$$\Theta_b(\mathbf{x}_{cv}) = \sum_{b=1}^{N_b} V_b \mathcal{G}_\Delta(\mathbf{x}_{cv}, \mathbf{x}_b) \quad (2.3)$$

where  $\mathcal{G}_\Delta$  is the interpolation function,  $N_b$  is the total number of bubbles, and the summation is over all bubbles. The momentum conservation equation is (Gidaspow, 1994):

$$\frac{\partial}{\partial t} (\rho_\ell \Theta_\ell \mathbf{u}_\ell) + \nabla \cdot (\rho_\ell \Theta_\ell \mathbf{u}_\ell \mathbf{u}_\ell) = -\nabla(p) + \nabla \cdot (\Theta_\ell \mu_\ell \mathbf{D}) + \mathbf{f}_{b \rightarrow \ell}, \quad (2.4)$$

where  $p$  is the liquid phase pressure,  $\mathbf{D} = \nabla \mathbf{u}_\ell + \nabla \mathbf{u}_\ell^T$  is the deformation tensor, and  $\mathbf{f}_{b \rightarrow \ell}$  is the reaction force from the disperse phase onto the fluid phase per unit mass of

fluid and is given as:

$$\mathbf{f}_{b \rightarrow \ell}(\mathbf{x}_{cv}) = \sum_{b=1}^{N_b} \mathcal{G}_{\Delta}(\mathbf{x}_{cv}, \mathbf{x}_b) (\mathbf{F}_P + \mathbf{F}_D + \mathbf{F}_L + \mathbf{F}_{AM} + \mathbf{F}_{coll} + \mathbf{F}_{R_b}). \quad (2.5)$$

Note that the total force on the bubble includes the pressure force,  $F_P = -V_b \nabla p$  where  $V_b$  is the volume of the dispersed phase. The reaction of this force onto the fluid phase results in the force density  $+\Theta_b \nabla p$ . This reaction term related to the pressure gradient can be combined with the pressure gradient in the momentum equation (and noting that  $\Theta_b + \Theta_{\ell} = 1$ ) to obtain:

$$\frac{\partial}{\partial t} (\rho_{\ell} \Theta_{\ell} \mathbf{u}_{\ell}) + \nabla \cdot (\rho_{\ell} \Theta_{\ell} \mathbf{u}_{\ell} \mathbf{u}_{\ell}) = -\Theta_{\ell} \nabla (p) + \nabla \cdot (\Theta_{\ell} \mu_{\ell} \mathbf{D}) + \mathbf{f}'_{b \rightarrow \ell}, \quad (2.6)$$

where  $\mathbf{f}'_{b \rightarrow \ell}$  contains summation of all reaction forces in equation 2.5 except the pressure force. This formulation is commonly used in gas-fluidized beds (Kuipers et al., 1993; Darmana et al., 2006). In the absence of any fluid velocity, but in the presence of bubbles, the pressure gradient force is then appropriately balanced by the gravity force. For large-eddy simulation, the above equations are spatially filtered using density-weighted Favre averaging (Hutter and Jöhnk, 2004). Using the form in equation 2.6; however, gives rise to an unclosed term  $-\overline{\Theta_{\ell} \nabla p}$ . It is therefore advantageous to use the original form (equation 2.4), resulting in standard variable density LES equations (Moin and Apte, 2006; Mahesh et al., 2006). In this case, the reaction due to the pressure force is treated explicitly. For turbulent flows, the Favre averaged equations then have the same form as equation 2.4, except that the velocity fields are filtered  $\tilde{u}_i$  and the fluid viscosity  $\mu_{\ell}$  is changed to  $\mu_{\text{eff}} = \mu_{\ell} + \mu_T$  accounting for the eddy viscosity. The turbulent eddy viscosity can be modeled using dynamic Smagorinsky model (Germano et al., 1991; Moin et al., 1991; Moin and Apte, 2006).

## 2.2 Disperse Phase Equations

The motion of each individual bubble is computed by solving the equations of motion in a Lagrangian frame. The bubble size variations are modeled by the incompressible Rayleigh-Plesset equations. The position, momentum equations and bubble radius

equations are given as:

$$\frac{d}{dt}(\mathbf{x}_b) = \mathbf{u}_b \quad (2.7)$$

$$m_b \frac{d}{dt}(\mathbf{u}_b) = \mathbf{F}_{\ell \rightarrow b} \quad (2.8)$$

$$\rho_\ell \left[ R_b \frac{d^2 R_b}{dt^2} + \frac{3}{2} \left( \frac{dR_b}{dt} \right)^2 \right] = p_B - p_\infty - \frac{2S}{R_b} - \frac{4\mu_\ell}{R_b} \frac{dR_b}{dt} \quad (2.9)$$

where  $\mathbf{x}_b$  and  $\mathbf{u}_b$  are the bubble position and velocity,  $m_b$  is the mass,  $\mathbf{F}_{\ell \rightarrow b}$  is the total force acting on the bubble,  $R_b$  is the bubble radius,  $p_B$  and  $p_\infty$  are the pressures inside and outside of the bubble,  $S$  is the surface tension coefficient, and  $\mu_\ell$  and  $\rho_\ell$  are the liquid viscosity and densities, respectively. To estimate  $p_B$ , it is typically assumed that the bubble contains some contaminant gas which expands or contracts according to adiabatic or isothermal processes (Chahine et al., 1993; Brennen, 1995). Pressure inside bubble consists of contribution from the gas pressure  $p_g$  and the vapor pressure  $p_v$ . The net force acting on each individual bubble is given as (Johnson and Hsieh, 1966):

$$\mathbf{F}_{\ell \rightarrow b} = \mathbf{F}_G + \mathbf{F}_P + \mathbf{F}_D + \mathbf{F}_L + \mathbf{F}_{AM} + \mathbf{F}_{coll} + \mathbf{F}_{\dot{R}_b} \quad (2.10)$$

where  $\mathbf{F}_G = (\rho_b - \rho_\ell)V_b \mathbf{g}$  is the gravitational force,  $\mathbf{F}_P = -V_b \nabla p$  is the pressure force due to far-field pressure gradients,  $\mathbf{F}_D = -\frac{1}{2}C_D \rho_\ell \pi R_b^2 |\mathbf{u}_b - \mathbf{u}_\ell| (\mathbf{u}_b - \mathbf{u}_\ell)$  is the drag force,  $\mathbf{F}_L = -C_L \rho_\ell V_b (\mathbf{u}_b - \mathbf{u}_\ell) \times \nabla \times \mathbf{u}_\ell$  is the lift force,  $\mathbf{F}_{AM} = -\frac{1}{2} \rho_\ell V_b \left( \frac{D\mathbf{u}_b}{Dt} - \frac{D\mathbf{u}_\ell}{Dt} \right)$  is the added mass force, and  $\mathbf{F}_{coll}$  is the inter-bubble or bubble-wall collision forces. The force  $\mathbf{F}_{\dot{R}_b} = -4\pi \rho_\ell R_b^2 (\mathbf{u}_b - \mathbf{u}_\ell) \frac{dR_b}{dt}$  represents momentum transfer due to variations in bubble size. Here,  $V_b$  is the bubble volume and subscripts ' $b$ ' and ' $\ell$ ' correspond to the bubble and liquid, respectively. Several different models for the drag ( $C_D$ ) and lift ( $C_L$ ) coefficients have been used that account for bubble deformation and variations in bubble Reynolds numbers ( $Re_b = \rho_\ell |\mathbf{u}_b - \mathbf{u}_\ell| 2R_b / \mu_\ell$ ) (Darmana et al., 2006). The collision forces can be computed using the standard collision models typically used in the discrete element method and are described later.

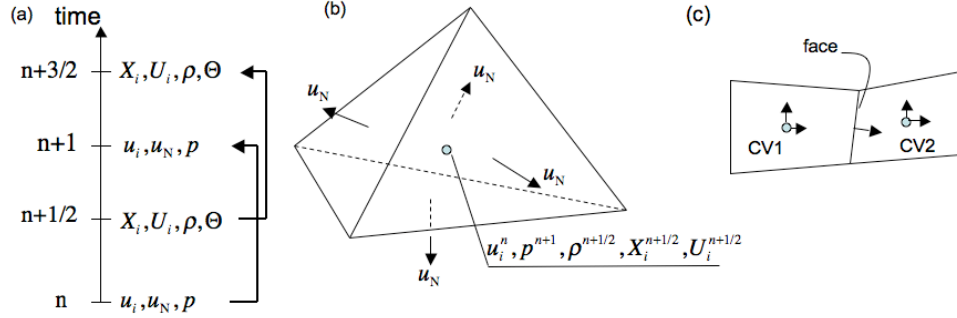


Figure 2.1: Schematic of the grid stencil: (a) time staggering of variables, (b) velocity ( $u_i$ ) and pressure fields ( $p$ ) are co-located at the control volume center,  $u_N$  is the face-normal velocity, (c) control volume and face connectivity.

### 2.3 Discretization of Fluid Phase Equation

The numerical scheme for unstructured, arbitrary shaped elements (Mahesh et al., 2006) is modified to take into account the liquid volume fraction. The changes in local liquid volume fractions requires solution of a *variable density* flowfield as opposed to the constant density, incompressible flows studied by Apte et al. (2003c); Mahesh et al. (2004). The steps in solving the coupled fluid-particle equations are given below. A semi-implicit scheme is used for the fluid solver, however, the interphase momentum exchange terms are treated explicitly.

Figure 2.1 shows the schematic of variable storage in time and space. The dispersed phase positions, density, pressure and volume fractions are staggered in time with respect to the fluid and particle velocity fields,  $u_i$  and  $U_i$ , respectively. All variables are stored at the control volume ( $cv$ ) center with the exception of the face-normal velocity  $u_N$ , located at the face centers. The face-normal velocity is used to enforce continuity equation. Capital letters are used to denote disperse phase. The time-staggering is done so that the variables are located most conveniently for the time-advancement scheme. Collocated spatial arrangement for velocity and pressure field, used by Kim and Choi (2000); Mahesh et al. (2004, 2006), is followed. The main reason to use this arrangement as opposed to spatial-staggering is its easy application to unstructured grids and/or adaptive mesh refinement. Accordingly, the dispersed phase positions ( $X_i$ ), density ( $\rho$ ), volume fraction ( $\Theta$ ), and viscosity ( $\mu$ ) are located at time level  $t^{n+1/2}$  and  $t^{n+3/2}$  whereas

the fluid velocity ( $u_i, u_N$ ) and the dispersed phase velocity ( $U_i$ ), and the pressure ( $p$ ) are located at time level  $t^n$  and  $t^{n+1}$ . This makes the discretization symmetric in time, a feature important to obtain good conservation properties of the numerical scheme as emphasized and used by Pierce and Moin (2004) for low-Mach number, reactive flows.

Using these variable locations, integrating the governing equations over the control volume and applying Gauss' divergence theorem to transport volume integrals to surface integrals wherever possible, the discrete governing equations are derived. Accordingly, the continuity equation is

$$\frac{\rho_{cv}^{n+3/2} - \rho_{cv}^{n+1/2}}{\Delta t} + \frac{1}{V_{cv}} \sum_{\text{faces of cv}} \rho_{cv}^{n+1} u_N^{n+1} A_{\text{face}} = 0, \quad (2.11)$$

where  $\rho_{cv} = \rho_{\ell, cv} \Theta_{\ell, cv}$  is the density at the CV-center,  $\Delta t$  is the flow solver time-step,  $V_{cv}$  is the volume of the CV,  $A_{\text{face}}$  is the area of the face of a CV,  $u_N$  is the face-normal velocity, and  $\rho_{\text{face}}$  is the density at face of a CV. The density at the face can be readily obtained by using the arithmetic averages of the densities of the adjacent CVs (see figure 2.1), that is,  $\rho_{\text{face}} = \frac{1}{2}(\rho_{cv1} + \rho_{cv2})$ . However, for the present co-located grid finite volume scheme the critical difference between the density and the face-normal velocity is that, the face-normal velocity  $u_N$  is obtained through a projection scheme rather than interpolation. Furthermore, the density at time level  $t^{n+1}$  is also obtained from interpolation,  $\rho_{\text{face}}^{n+1} = (\rho_{\text{face}}^{n+3/2} + \rho_{\text{face}}^{n+1/3})/2$ .

The discrete momentum equation for the  $i^{\text{th}}$  component of velocity can be written as

$$\begin{aligned} \frac{g_{i, cv}^{n+1} - g_{i, cv}^n}{\Delta t} + \frac{1}{V_{cv}} \sum_{\text{faces of cv}} g_{i, \text{face}}^{n+1/2} u_N^{n+1/2} A_{\text{face}} &= -\frac{\partial}{\partial x_i} p_{cv}^{n+1} + \\ &\frac{1}{V_{cv}} \sum_{\text{faces of cv}} (\tau_{ij})_{\text{face}}^{n+1/2} N_{j, \text{face}} A_{\text{face}} + f_{i, cv}^{n+1/2}, \end{aligned} \quad (2.12)$$

where  $g_i = \rho u_i$  represents the momentum in the  $i^{\text{th}}$  direction,  $(\tau_{ij})_{\text{face}}$  is the viscous stress at the faces of control volume, and  $N_{j, \text{face}}$  represents the components of the outward face-normal. Similarly to the face density ( $\rho_{\text{face}}$ ), the velocity field ( $u_{i, \text{face}}$ ), and the momentum  $\rho u_{i, \text{face}}$  at the faces are obtained using arithmetic averages of the corresponding fields at two control volumes associated with the face. The values at time level

$t^{n+1/2}$  are obtained by time-averaging. The interface coupling force is represented by  $f_{i,cv}$ . The pressure field  $p_{cv}^{n+1}$  is unknown and is obtained using the best available guess at the current iteration. This gets updated during the solution of the pressure Poisson equation. The above discretization is implicit and thus the time-steps are not limited by viscous stability limits. The use of symmetric centered differences in space and time makes the algorithm second order on uniform Cartesian grids. The above formulation can also handle variations in the fluid density (due to say temperature variations in a gaseous fluid) by relating the fluid density  $\rho_\ell$  to state variables through proper equation of state.

## 2.4 Numerical Algorithm

The coupled ordinary-differential equations for the subgrid dispersed phase are solved first. The fluid-phase equations are solved using a pressure-based scheme for variable-density (due to void fraction variations), low-Mach number formulation as described below. The interaction forces between the two phases are treated explicitly.

### 2.4.1 Disperse-Phase Solution

The equations for position and velocity of the dispersed phase are solved first using explicit time advancing. This involves interpolation of the fluid velocity (for drag force calculation), pressure gradient (for pressure force), and vorticity (for lift force) to the disperse phase location. The interpolation is performed using the same Eulerian-Lagrangian interpolation kernel used for computation of the void fraction.

#### 2.4.1.1 Collision Force

The collision force is computed using a discrete element model of Cundall and Strack (1979). Accordingly, the force  $F_{pj}$  on bubble  $p$  due to collision with bubble  $j$  is given by

$$F_{\text{coll}}^{pj} = \begin{cases} 0 & \text{for } d^{pj} \geq (R_p + R_j + \alpha) \\ \left( k_c \delta_{pj}^{3/2} - \eta_c (\mathbf{u}_p - \mathbf{u}_j) \cdot \mathbf{n}_{pj} \right) \mathbf{n}_{pj} & \text{for } d^{pj} < (R_p + R_j + \alpha) \end{cases} \quad (2.13)$$

where  $d^{pj}$  is the distance between the centers of the  $p^{th}$  and  $j^{th}$  bubbles,  $\mathbf{n}_{pj}$  is the unit vector from the center of bubble  $j$  to that of bubble  $p$ ,  $\alpha$  is the force range,  $k_c$  the stiffness parameter, and  $\eta_c$  the damping parameter,  $R_p$  and  $R_j$  are the equivalent radii of bubbles,  $\delta^{pj} = (R_p + R_j + \alpha) - d^{pj}$ . Also, in order to conserve the binary collision forces,  $F_{\text{coll}}^{jp} = -F_{\text{coll}}^{pj}$ . Tsuji et al. (1993) used the following expressions to compute the damping parameter

$$\eta_c = 2\alpha \sqrt{\frac{m_p k_c}{1 + \alpha^2}}; \quad \alpha = -\ln(e/\pi) \quad (2.14)$$

where  $e$  is the coefficient of restitution,  $m_p$  is the mass of the bubble ( $p$ ). Similarly, the collision force ( $F_{\text{coll}}^{pw}$ ) between the bubble ( $p$ ) and the wall ( $w$ ) is given

$$F_{\text{coll}}^{pw} = \begin{cases} 0 & \text{for } d^{pw} \geq (R_p + \alpha) \\ \left( k_c \delta_{pw}^{3/2} - \eta_c (\mathbf{u}_p) \cdot \mathbf{n}_{pw} \right) \mathbf{n}_{pw} & \text{for } d^{pw} < (R_p + \alpha) \end{cases} \quad (2.15)$$

where  $d^{pw}$  is the distance between the bubble center and the wall, and  $\mathbf{n}_{pw}$  is the unit vector from the wall to the center of the parcel.

### 2.4.1.2 Solution of Rayleigh-Plesset Equation

In this section, an adaptive time stepping method for the solution of Rayleigh-Plesset equation based on the numerical stability criteria is proposed. This equation is a highly non-linear second order ODE, which shows sharp variation of solution ( $R_b$ ) near the collapse region of the bubble. It shows singular behavior when the bubble radius tends to zero. An ideal numerical scheme should be able to handle the rebound behavior of the bubble after it collapses. The solution may become unstable if the time step  $\Delta t$  is not chosen properly small. Use of a simple explicit scheme with very small time-step can be prohibitively expensive even for a single bubble computation. An adaptive time-stepping strategy is necessary such that the bubble collapse and rapid expansion regions utilize small time-steps, but a much larger time-step can be used for relatively slow variations in bubble radius. So we adaptively resize the time step based on stability threshold which is explained below. This minimizes the overall number of loops in the numerical solution process.

The equation for bubble radius variations (equation 2.9) can be cast into two first

order ODEs Alehossein and Qin (2007):

$$\frac{dR_b}{dt} = y; \quad \frac{dy}{dt} = -\frac{3y^2}{2R_b} + \frac{p_B - p_\infty - 2S/R_b}{\rho_\ell R_b} - \frac{4\mu_\ell y}{\rho_\ell R_b^2}. \quad (2.16)$$

These can be written in a matrix notation  $[X]' = [F]$  where  $[X]$  and  $[F]$  are  $2 \times 1$  matrices defined below:

$$[X] = \begin{bmatrix} R_b \\ y \end{bmatrix}; \quad [F] = \begin{bmatrix} y \\ -\frac{3y^2}{2R_b} + \frac{p_B - p_\infty - 2S/R_b}{\rho_\ell R_b} - \frac{4\mu_\ell y}{\rho_\ell R_b^2} \end{bmatrix}. \quad (2.17)$$

Following the above notation, a simple first order blended Euler scheme can be derived:

$$[X]^{n+1} = [X]^n + h \left( \theta [F]^n + (1 - \theta) [F]^{n+1} \right) \quad (2.18)$$

where  $h$  is the step size,  $n$  and  $n + 1$  denote the current and next time steps, respectively. The blending parameter ( $\theta$ ) can be changed between 0 and 1 to change the scheme from fully implicit backward Euler to fully explicit forward Euler method. Using Taylor series and chain rule,  $[F]^{n+1}$  can be linearized:

$$[F]^{n+1} = ([I] + h[J]^n) [F]^n + O(h^2) \quad (2.19)$$

where  $[J] = \partial[F]/\partial[X]$  is the Jacobian matrix calculated at time step  $n$ . Substituting in equation 2.18 gives the discretized form of the linearized ODE using first order Euler method:

$$[X]^{n+1} = [X]^n + h[F]^n + h^2(1 - \theta)[J]^n[F]^n. \quad (2.20)$$

In presence of large variations in the outside pressure ( $P_\infty$ ), the bubble radius  $R_b$  and its time derivative  $\dot{R}_b$  can change rapidly, which may give rise to numerical instability. Following the notion of simplified ODE for the stability analysis (Moin, 2001),  $[X]' = [F] = [J][X]$ , one can derive the general stability criteria for any system of first order ODE. By discretization in first order blend scheme,

$$\frac{[X]^{n+1} - [X]^n}{h} = \theta [J]^n [X]^n + (1 - \theta) [J]^n [X]^{n+1} \quad (2.21)$$

so,

$$[X]^{n+1} = [A]^n [X]^n \quad (2.22)$$

where  $[A]^n = \{1 - h(1 - \theta)[J]^n\}^{-1} (1 + h\theta[J])$ . This equation can be diagonalized to give

$$[Z]^{n+1} = [\lambda]^n [Z]^n \quad (2.23)$$

where  $\lambda$  is the matrix of eigenvalues  $\lambda_1$  and  $\lambda_2$  associated with  $R_b$  and  $dR_b/dt$  respectively. The solution of equation 2.23 is of the form:  $Z_1^n = e^{\lambda_1} Z_1^0$  and  $Z_2^n = e^{\lambda_2} Z_2^0$ . The adaptive time-stepping strategy here is, therefore, to keep the magnitude of  $\lambda_1$  and  $\lambda_2$  close to unity. The magnitude of the eigenvalues is adjusted by resizing the time step  $h$  at each subcycling time steps for the solution of Rayleigh-Plesset equation.

The above strategy, in combination with fourth order Runge-Kutta (RK4) scheme is being used. The stability of the solution will be affected, since RK4 method has a more broad stability margin (Moin, 2001) than first order Euler method. Different steps in time step calculation are explained below:

- **Step 1:** Calculate Jacobian Matrix

$$[J] = \frac{\partial[F]}{\partial[X]} = \begin{bmatrix} \partial f_1/\partial x_1 & \partial f_1/\partial x_2 \\ \partial f_2/\partial x_1 & \partial f_2/\partial x_2 \end{bmatrix}, \quad (2.24)$$

where,  $f_1 = y = dR_b/dt$  and  $f_2 = -3y^2/2R_b + (P_B - P_\infty - 2S/R_b)/\rho R_b - 4\mu y/\rho R_b^2$ .  
so,

$$\begin{aligned} \partial f_1/\partial x_1 &= \partial y/\partial R_b = 0 \\ \partial f_1/\partial x_2 &= \partial y/\partial y = 1 \\ \partial f_2/\partial x_1 &= \frac{3}{2} \left( \frac{y}{R_b} \right)^2 - \frac{P_B - P_\infty}{\rho R_b^2} + \frac{4S}{\rho R_b^3} + \frac{8\mu y}{\rho R_b^3} \\ \partial f_2/\partial x_2 &= -\frac{3y}{R_b} - \frac{4\mu}{\rho R_b^2}. \end{aligned}$$

- **Step 2:** Calculate matrix  $[A]$  and its eigenvalues  $\lambda_1$  and  $\lambda_2$ . Then calculate deviation from unity  $\delta = \max(\text{abs}(\lambda_1 - 1), \text{abs}(\lambda_2 - 1))$ .
- **Step 3:** Compare  $\delta$  to  $\delta_{max}$  and resize  $h$  accordingly.

One can use any time step resizing strategy in this calculation. Here is a brief description of what is used here:

- **3.1:** if  $h$  is small or  $\delta < \delta_{max}$  then  $h' = 2 \times h$ .  
Keep multiplying by two until  $\delta(h) < \delta_{max} < \delta(h')$ .
- **3.2:** if  $h$  is large or  $\delta_{max} < \delta$  then  $h' = 0.5 \times h$ .  
Keep multiplying by 0.5 until  $\delta(h') < \delta_{max} < \delta(h)$ .
- **3.3:** Once  $\delta_{max}$  is between  $\delta(h)$  and  $\delta(h')$ , then average  $h$  and  $h'$  ( $h_{new} = 0.5 \times (h + h')$ ). Repeat the above calculations with the averaged value until  $\delta(h_{new})$  is close enough to  $\delta_{max}$ .

$\delta_{max}$  is a critical value in this calculation. It should be as large as possible to achieve minimum number of time steps in the computation. In the test cases presented in following sections,  $\delta_{max}$  was set to 5%.

This approach is found to be very effective even in the case of rapid and large pressure variations as shown in the validation cases in the following sections.

### 2.4.1.3 Subcycling and Adaptive Time Step Selection

Once all the forces are known for each bubble, the position and velocity field are advanced using an explicit Euler scheme from  $t^{n+1/2}$  to  $t^{n+3/2}$ . It is important to note that the time-scales associated with subgrid bubbles can be vastly different from those of the flow solver time step ( $\Delta t = t^{n+3/2} - t^{n+1/2}$ ). Thus, the time step used for integration of the dispersed phase equations can be different than the flow solver time step. The time scales associated with the bubble motion can be characterized by looking at the various forces acting on the bubbles. For example, the expression for the acceleration due to drag force ( $F_D/m_b$ ) can be rearranged to provide the particle relaxation time-scale:

$$\frac{F_D}{m_b} = -\frac{(u_b - u_\ell)}{\tau_R}; \quad \tau_R^{-1} = \frac{3}{4} C_D \frac{\rho_\ell}{\rho_b} \frac{|u_b - u_\ell|}{d_b}. \quad (2.25)$$

Likewise the time-scale associated with the lift force is proportional to the vorticity magnitude;  $\tau_L^{-1} = C_L |\nabla \times \mathbf{u}_\ell|$ . The collision force also is constrained by a time-scale which depends on the collision model and the parameters used. For the collision model

described above, Cundall and Strack (1979) propose a time step restriction given as  $\Delta t_{\text{coll}} \leq \sqrt{m_b/k_c}$ . Finally, in the presence of large variations in fluid pressure, the time-scale restrictions based on the Rayleigh-Plesset equations ( $\Delta t_{\text{RP}}$ ) can be obtained from the stability analysis described above.

Since explicit time-stepping is used, the time step ( $\Delta t_{\text{bub}}$ ) used for advancing the disperse phase equations should be comparable to the smallest time-scales governing their dynamics. Accordingly, for each flow-solver time-step ( $\Delta t$ ), the time step used for bubble dynamics is obtained as follows:

$$\Delta t_{\text{bub}} = \min \left( \frac{\Delta t}{3}, \tau_R, \tau_L, \tau_{\text{coll}}, \tau_{\text{RP}} \right). \quad (2.26)$$

Since  $\Delta t_{\text{bub}}$  can be smaller than flow solver time-step ( $\Delta t$ ), a sub-cycling procedure is used, the bubble dynamics equations are solved repeatedly until we reach one flow solver time step. The bubble dynamics equations are updated using explicit Euler scheme; the bubbles are duly transferred across processors as their positions are updated. During this sub-cycling process, it is assumed that the fluid flow quantities do not change significantly similar to a quasi-steady assumption. In addition, typically for time-resolved simulations (such as large-eddy simulation), it is necessary to use the flow solver time-step such that the convective CFL number is less than unity. Under these conditions, in most applications, the bubbles may not move significantly during one time-step. Hence, an actual update of the neighbor list for collision partners can only be done once per flow solver time-step.

#### 2.4.1.4 Interpolation Operator for Lagrangian-Eulerian Mapping

In the simulation of a coupled liquid and bubble system, mapping data from Eulerian framework (liquid phase) to Lagrangian framework (bubble/particle phase) is necessary. In the Lagrangian calculation, data sets such as flow velocity, pressure, acceleration, etc., are needed for the bubble/particle motion. On the other hand, reaction forces acting on liquid phase and bubble volume fraction are needed to be mapped into Eulerian framework.

The interpolation function should be smooth and conservative in transferring variable (Kitagawa et al., 2001). In an orthogonal structured computational grid, linear

or bilinear interpolation technique can be applied, depending on the level of accuracy needed. Snider (2001) used a trilinear interpolation technique in a staggered grid computation. McDermott and Pope (2008) have recently proposed the Parabolic Edge Reconstruction Method (PERM) for continuous velocity field reconstruction in the subgrid level.

Kernel-based interpolation techniques, typical of particle methods, can be easily applied to complex and unstructured grids. Different interpolation kernels using polynomial (Deen et al., 2004; Darmana et al., 2006) or exponential (Eldredge et al., 2002; Apte et al., 2003b) function formulation have been used. Gaussian kernel provides quadrature spectral accuracy, provided that the interpolation is being performed over a region much larger than the kernel width ( $d > \Delta$ ) (Eldredge et al., 2002), otherwise the accuracy reduces to second order. They provide smooth and accurate interpolation but do not provide compact support, which makes using this kernel computationally more expensive than the polynomial method.

The Gaussian interpolation function is given by

$$\mathcal{G}_\Delta(\mathbf{x}, \mathbf{x}_b) = \frac{1}{(\Delta\sqrt{(2\pi)})^3} \exp\left(-\frac{\sum_{k=1}^3 (x_k - x_{p,k})^2}{2\Delta^2}\right), \quad (2.27)$$

where  $\Delta$  is the kernel width,  $x$  and  $x_b$  denote the available data point on the grid and the bubble location, respectively. In order to enforce mass conservation, the kernel function is normalized over the volume of integration by

$$\int_{V_{cv}} \mathcal{G}_\Delta(\mathbf{x}_{cv}, \mathbf{x}_b) dV = 1. \quad (2.28)$$

Using the above kernel, volume fraction of the liquid can be calculated as

$$\Theta_\ell = 1 - \frac{\sum_{i=1}^{n_b} V_b \mathcal{G}_\Delta}{V_{cv}}. \quad (2.29)$$

## 2.4.2 Fluid-Phase Solution

The fluid flow solver is based on a co-located grid finite volume scheme for arbitrary shaped unstructured grids (Mahesh et al., 2006; Moin and Apte, 2006). The main steps

of the solver are described below.

- **Step 1:** Advance the bubble positions, velocities, and radii using the adaptive time-stepping algorithm described above. Compute the void fraction field at the new bubble locations using the Lagrangian-Eulerian interpolation kernel and set the density  $\rho = \rho_\ell \Theta_\ell$ .
- **Step 2:** Advance the fluid momentum equations using the fractional step algorithm, with the interphase force,  $\mathbf{F}$ , treated explicitly (the subscript  $\ell$  for fluid phase is dropped for simplicity).

$$\begin{aligned} \frac{\rho_{\text{cv}}^{n+1} u_i^* - \rho_{\text{cv}}^n u_i^n}{\Delta t} + \frac{1}{2V_{\text{cv}}} \sum_{\text{faces of cv}} \left[ \rho_{\text{face}}^{n+1} u_{i,\text{face}}^* + \rho_{\text{face}}^n u_{i,\text{face}}^n \right] u_{\text{N}}^{n+1/2} A_{\text{face}} = \\ - \frac{\delta p^n}{\delta x_i} + \frac{1}{2V_{\text{cv}}} \sum_{\text{faces of cv}} \mu_{\text{face}}^* \left( \frac{\partial u_{i,\text{face}}^*}{\partial x_j} + \frac{\partial u_{j,\text{face}}^n}{\partial x_i} \right) A_{\text{face}} + f_i^{n+1/2}, \end{aligned} \quad (2.30)$$

where  $\text{N}$  is the face-normal component, and  $A_{\text{face}}$  is the face area. The density fields at faces are obtained using simple arithmetic averages of density at adjacent CVs. Here the fluid viscosity is given as  $\mu_{\text{face}}^* = \Theta_{\ell,\text{face}} \mu_{\text{eff,face}}$  where  $\mu_{\text{eff}}$  is the summation of the dynamic viscosity and eddy viscosity obtained from the dynamic Smagorinsky model. The pressure gradient at the CV centers in the above equation is at the old time-level and is obtained as described below. The reaction force  $f_i^{n+1/2}$  is obtained through Lagrangian-Eulerian interpolation and consists of the pressure force on the disperse phase. In the above step, the viscous terms are treated implicitly, the three equations for the velocity components at the CV centers are solved using iterative scheme such as Gauss-Seidel.

- **Step 3:** Remove the old pressure gradient to obtain the velocity field,  $\hat{u}_i$ :

$$\frac{\rho_{\text{cv}}^{n+1} \hat{u}_i - \rho_{\text{cv}}^{n+1} u_i^*}{\Delta t} = + \frac{\delta p^n}{\delta x_i} \quad (2.31)$$

- **Step 4:** Interpolate the velocity fields to the faces of the control volumes and consider the corrector step:

$$\frac{\rho_{\text{face}}^{n+1} u_{\text{N}}^{n+1} - \rho_{\text{face}}^{n+1} \hat{u}_{\text{N}}}{\Delta t} = - \frac{\delta p}{\delta x_{\text{N}}}^{n+1}, \quad (2.32)$$

where  $\hat{u}_{\text{N}} = \hat{u}_{i,\text{face}} n_{i,\text{face}}$  is the approximation for face-normal velocity and  $N_{i,\text{face}}$  are the components of the face-normal. To compute the face-based pressure gradient, the face that each face has two adjacent CVs (CV1 and CV2) is used, as shown in figure 2.1c. The face-normal pressure gradient is discretized as:

$$\frac{\delta p}{\delta x_{\text{N}}}^{n+1} = \frac{p_{\text{nbr}}^{n+1} - p_{\text{cv}}^{n+1}}{|\mathbf{S}_{\text{cv} \rightarrow \text{nbr}}|}, \quad (2.33)$$

where the subscripts cv and nbr stand for the the control volume CV for which the velocity field is being solved and the neighboring CV sharing a common face, respectively and  $|\mathbf{S}_{\text{cv} \rightarrow \text{nbr}}|$  represents the magnitude of the vector connecting the two control volumes.

- **Step 5:** The pressure field and the pressure gradients at  $t^{n+1}$  are unknown in the above step. A pressure Poisson equation is derived by taking a discrete divergence of the above equations and solving for the pressure field at each control volume:

$$\sum_{\text{face of cv}} \Delta t \frac{\delta p}{\delta x_{\text{N}}}^{n+1} = \sum_{\text{faces of cv}} \rho_{\text{face}}^{n+1} \hat{u}_{i,\text{face}} A_{\text{face}} + V_{\text{cv}} \frac{\rho_{\text{cv}}^{n+3/2} - \rho_{\text{cv}}^{n+1/2}}{\Delta t}. \quad (2.34)$$

- **Step 6:** Reconstruct the pressure gradient at the CV centers. The face-normal pressure gradient  $\frac{\delta p}{\delta x_{\text{N}}}$  and the gradient in pressure at the CV-centroids are related by the area-weighted least-squares interpolation (Mahesh et al., 2004, 2006):

$$\epsilon_{\text{cv}} = \sum_{\text{faces of cv}} (P'_{i,\text{cv}} N_{i,\text{face}} - P'_{\text{face}})^2 A_{\text{face}}, \quad (2.35)$$

where  $P'_{i,\text{cv}} = \frac{\delta p}{\delta x_i}$  and  $P'_{\text{face}} = \frac{\delta p}{\delta x_{\text{N}}}$ .

- **Step 7:** Compute new face-based velocities, and update the CV-velocities:

$$u_N^{n+1} = \hat{u}_N - \frac{\Delta t}{\rho_{\text{face}}^{n+1}} \frac{\delta p^{n+1}}{\delta x_N} \quad (2.36)$$

$$u_{i,\text{cv}}^{n+1} = \hat{u}_{i,\text{cv}} - \frac{\Delta t}{\rho_{\text{cv}}^{n+1}} \frac{\delta p^{n+1}}{\delta x_{i,\text{cv}}} \quad (2.37)$$

## Chapter 3 – Verification Test Cases for Bubble-laden Flows

### 3.1 Oscillating Bubbles

The importance of volumetric displacement effect on the flow field, caused by change in local concentration of bubbles is being investigated in this test case. The variable density formulation used in these simulations accounts for changes in the local mixture density caused by bubble accumulation/scattering in the flow field due to inter-phase momentum exchanges, or size variation in a cavitating bubble due to hydrodynamic pressure of the flow. A simple case of imposed oscillation on the radius of a bubble causing a potential flow field around itself is first simulated. This phenomenon can not be simulated by only using the inter-phase momentum coupling (neglecting variations in the void fractions). It is shown here that the local variations in mixture density in momentum and continuity equations provide the correct solution. It was also found that the pressure field obtained due to bubble oscillation cannot be accurately captured by only considering two-way coupling and neglecting volumetric displacement.

Assuming the bubble radius oscillates as,

$$R_b = R_{b,0}(1 - \epsilon \sin \omega t), \quad (3.1)$$

where  $R_b$  and  $R_{b,0}$  are the instantaneous and initial bubble radii, respectively,  $\epsilon$  is the non-dimensional amplitude of oscillation, and  $\omega$  is the frequency. One can derive the analytical expression for pressure, following the potential flow theory (Panton, 2006),

$$\frac{p(R) - p(\infty)}{\rho_\ell R_{b,0}^2 \omega^2} = -\epsilon \sin \omega t + \frac{2}{3} \epsilon^2 \left( 1 - \frac{5}{2} \sin^2 \omega t \right), \quad (3.2)$$

where  $\rho_\ell$  is liquid density.

In this test case, a single air bubble is placed in water inside a cubical domain. A sinusoidal perturbation is imposed on the bubble. Bubble radius changes in time as  $R_b = R_{b,0}(1 - \epsilon \sin \omega t)$ , where  $R_b$  and  $R_{b,0}$  are the instantaneous and the initial radius,

Table 3.1: Physical parameters and computational settings for the oscillating bubble

Density of fluid $\rho_\ell$ [kg/m <sup>3</sup> ]	$10^3$
Density of bubble $\rho_b$ [kg/m <sup>3</sup> ]	1
kinematic viscosity of liquid $\nu_f$ [m <sup>2</sup> /s]	$10^{-6}$
Frequency of oscillation [Hz]	50
Perturbation magnitude	$0.1 \times R_{b,0}$
Domain size	$l_x = l_y = l_z = 100 \times R_{b,0}$
Grid	$32^3$

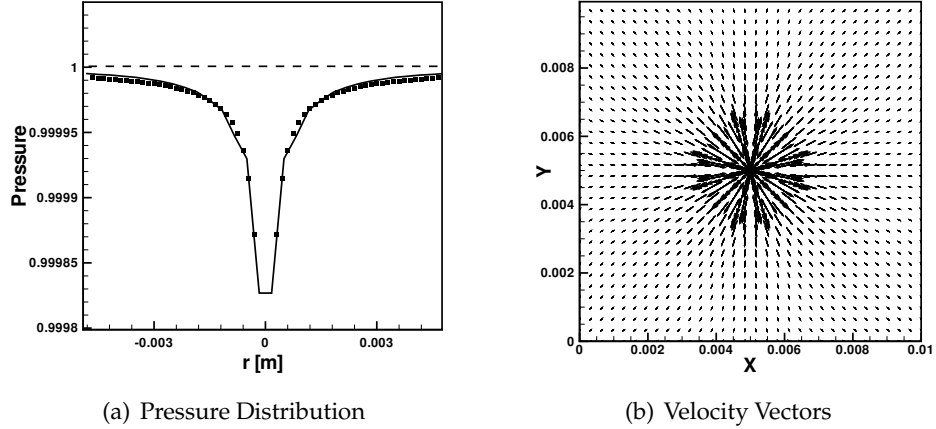


Figure 3.1: Flow developed by an oscillating bubble: (a) Pressure distribution caused by volume displacement around the bubble compared with analytical solution (dashed line shows the pressure field if the void fraction variations are neglected), (b) instantaneous velocity vector field due to bubble oscillations.

respectively,  $\epsilon$  is the perturbation magnitude,  $\omega$  is frequency and  $t$  is time. In this simulation,  $R_{b,0} = 0.01 \times D$ , where  $D$  is the cube size, and gives overall bubble concentration of  $4 \times 10^{-6}$ ,  $\epsilon = 0.1$ ,  $\omega = 50$  [Hz]. Simulation parameters and settings are listed in table 3.1.

Figure 3.1a shows the radial distribution of hydrodynamic pressure around the bubble created by the size variation at  $t^* = 0.3$  where  $t^* = t/T$  and  $T = 2\pi/\omega$ . Also shown are the instantaneous velocity vectors due to bubble oscillation (figure 3.1b). The pres-

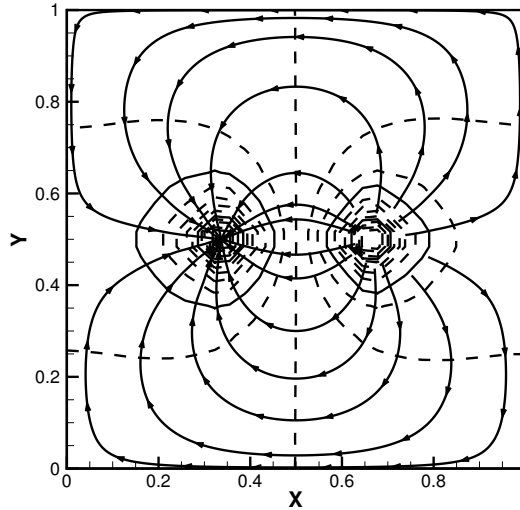


Figure 3.2: Doublet generated by bubbles oscillating in tandem. Streamlines and pressure contours (dashed line) are shown.

sure field is well predicted by the present numerical scheme.

In another example two bubbles oscillating in tandem are considered. Two similar bubbles are placed in a box and their radii change sinusoidally as above with a phase difference of  $\pi$  [rad]. All properties are similar to the single bubble case, except they are both located  $D/6$  away from the box center. The result is a doublet-like flow which is shown in figure 3.2.

### 3.2 Bubble Dynamics Under Imposed Pressure Variations:

To test the adaptive time-stepping approach, a numerical test case is considered wherein the external pressure is specified as a function of time and the bubble radius is computed using the Rayleigh-Plesset equation. This test case was also used by Alehossein and Qin (2007) in their work on simulating cavitating bubbles in a convergent divergent nozzle. Figure 3.3a shows an imposed pressure variation to a stationary bubble. The fluid properties are those for water ( $\rho_\ell = 1000 \text{ kg/m}^3$ ,  $\mu_\ell = 0.798 \times 10^{-3} \text{ kg/ms}$ ,  $S = 0.072 \text{ N/m}$ ,  $p_v = 0.00424 \text{ MPa}$ ). A bubble of initial radius ( $R_{b,0} = 100 \text{ }\mu\text{m}$ ,

$dR_{b,0}/dt = 0$ ) is subjected to the outside pressure variation shown in figure 3.3a.

The bubble undergoes growth and collapse as the outside pressure changes with time. Rapid accelerations and variations in bubble radius are observed. This test case is challenging for a numerical scheme based on constant time-steps. For an explicit Euler scheme, for example, a constant time-step on the order of  $10^{-17}$  s would be required to capture the bubble growth and collapse and maintain a stable solution. Multiple periods of bubble oscillation would be very time-consuming for such an approach and adaptive time-stepping is essential.

Figure 3.3b shows the solution obtained from the adaptive time-stepping. Also shown are the temporal variations in the eigenvalues  $\lambda_1$  and  $\lambda_2$  of the the coupled system of equations 2.23. Deviation of these eigenvalues from a value of unity correspond to rapid growth or decay period of the bubble and are good indicators for adaptive time-stepping. The time-step is thus changed if the eigenvalues depart from the unity value by 5% or more.

With this approach stable solutions are obtained for much higher time-steps and multiple periods of bubble oscillation can be easily computed. Figure 3.3c shows that only around 2000 iterations are required to compute five periods of bubble oscillation. A time-step refinement study provided little variations in the predicted variations for bubble radius.

### 3.3 Terminal Velocity Test

In order to test the accuracy of integration method for the particle equation of motion, and also show the effectiveness of the mapping procedure from Lagrangian framework to Eulerian and vice versa, the scheme is being tested on a single rising bubble in a quiescent liquid column.

Bubble density and diameter are  $\rho_b = 1 \text{ kg/m}^3$  and  $D_b = 1 \text{ mm}$ , and the liquid density and viscosity are  $\rho_\ell = 1000 \text{ kg/m}^3$  and  $\mu_\ell = 10^{-3} \text{ kg/m.s}$ , respectively. The computational domain size is  $50 \times 400 \times 50 \text{ mm}^3$  and a uniform grid with  $25 \times 200 \times 25$  elements is used. Bubble initial conditions are  $\vec{x} = (0, 25, 0) \text{ mm}$  and  $\vec{v} = (0, 0, 0) \text{ m/s}$ . The time step is  $\Delta t = 10^{-5} \text{ sec}$ , which is smaller than the bubble response time  $\tau_b = \rho_b D_b^2 / 18 \mu_\ell$ .

Figure 3.4 shows the rising velocity of the bubble in comparison to a solution ob-

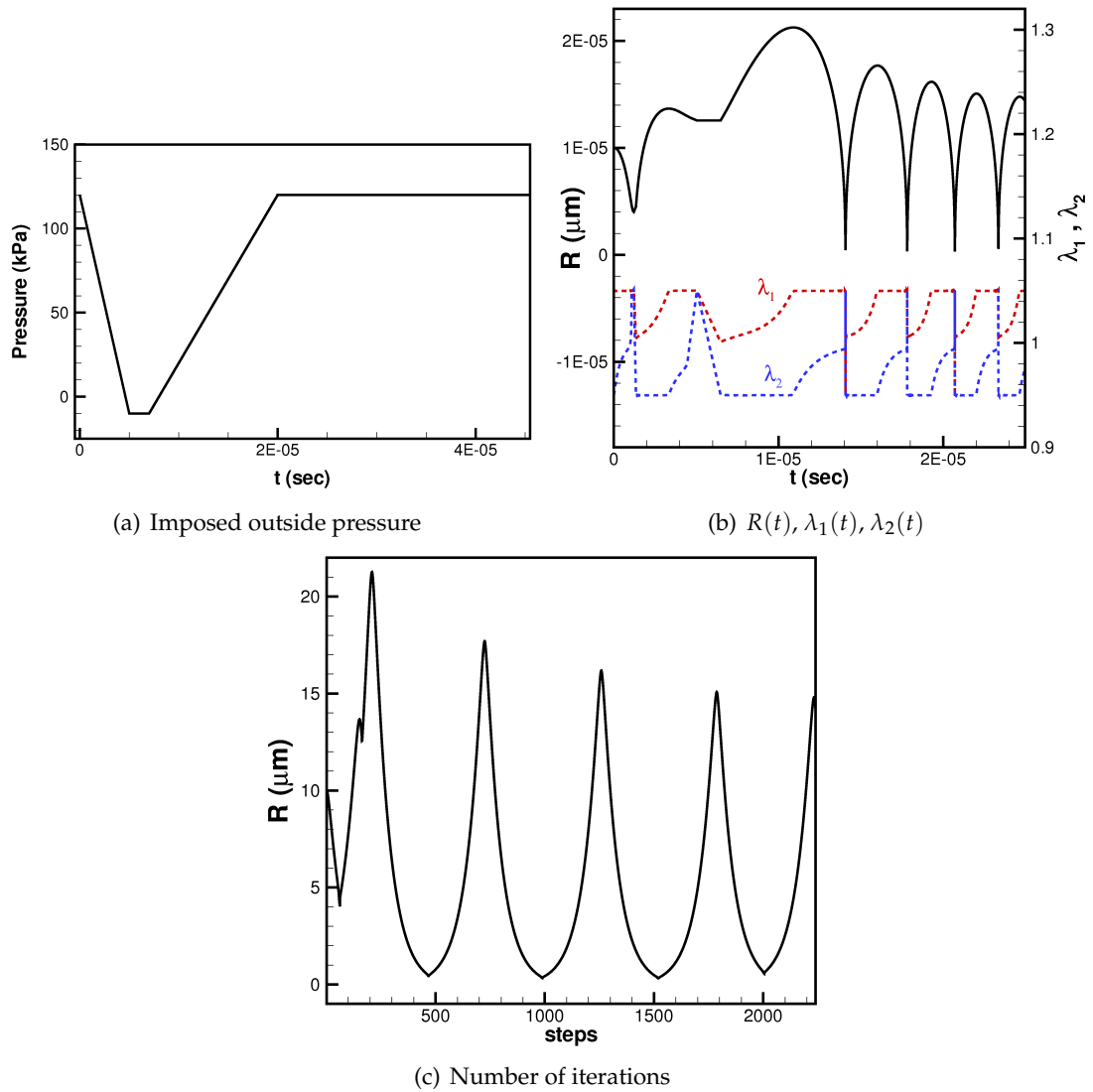


Figure 3.3: Time variation of bubble radius and  $\lambda$  values for a cavitating bubble with imposed pressure variations.

tained independently by integrating the equation of motion.

The next test case is a falling glass bead in air. Particle density is  $\rho_p = 2500 \text{ kg/m}^3$  and air density and viscosity are  $\rho_\ell = 1.0 \text{ kg/m}^3$  and  $\mu_\ell = 10^{-5} \text{ kg/m.s}$ , respectively. The same computational grid as the previous case is used here. Figure 3.5 shows the

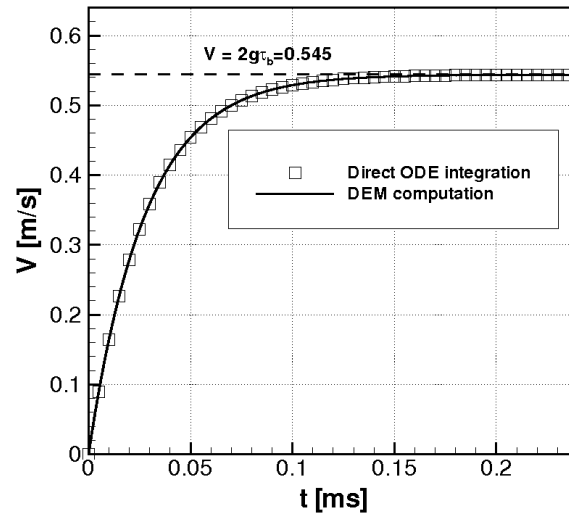


Figure 3.4: Rising velocity of a single bubble in a liquid column from direct integration of ODE (symbols) and numerical simulation (solid line).

result for the falling particle case.

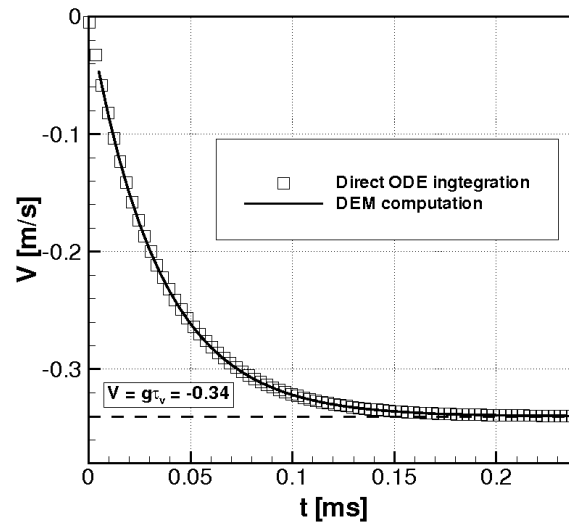


Figure 3.5: Falling velocity of a glass bead in air from direct integration of ODE (symbols) and numerical simulation (solid line).

Both test cases show very good agreement with the predicted analytical terminal

velocity as well as the results from a stand alone higher order numerical integration of particle equation of motion.

### 3.4 Bubble Trajectory in a Line Vortex

Accurate prediction of bubble motion in a vortex is highly important since forces other than drag (i.e. lift and added mass) may become significant in complex flow. A line vortex configuration is chosen to show the ability of the method in accurate calculation of different forces and trajectory. Line vortex (often called Rankine Vortex) is a model for vortical flow generated at the tip of ship propeller blades. The model consists of a forced vortex region, named core, and a free vortex region outside the core.

Flow velocity and pressure are defined as

$$u_{\theta}(r) = \left\{ \begin{array}{l} \frac{\Gamma}{2\pi a_c^2} r, r \leq a_c; \\ \frac{\Gamma}{2\pi r}, r > a_c \end{array} \right\} \quad (3.3)$$

$$p_{\omega}(r) = \left\{ p_{\infty} - \frac{\rho\Gamma^2}{4\pi^2 a_c^2} + \frac{\rho\Gamma^2 r^2}{8\pi^2 a_c^4}, r \leq a_c; \quad p_{\infty} - \frac{\rho\Gamma^2}{8\pi^2 r^2}, r > a_c \right\}, \quad (3.4)$$

where  $u_{\theta}$  is the angular component of velocity vector,  $\Gamma = \pi a_c^2 \omega$  is the vortex circulation,  $\omega$  is vorticity inside the core,  $r$  is the radial distance to the vortex center, and  $a_c$  is the vortex core radius, in which the circulation is constant, and outside of the core is zero. Vortex core size, vorticity, and circulation, are functions of free stream velocity  $V_{\infty}$  and propeller chord length  $C_0$  Hsiao et al. (2003).

A brief analysis on the motion of a single bubble in Rankine vortex, with error analysis of the numerical results are presented in the following sections. In order to analyze the accuracy of bubble motion, a single bubble moving in a line vortex is simulated.

#### 3.4.1 Motion Analysis of a Single Bubble

One can analyze the behavior of a bubble in the core region of the Rankine vortex by using the equations 3.3 and 3.4 in the bubble equation of motion ( 2.10). The bubble

acceleration inside the vortex core can be written in cylindrical coordinates,

$$\frac{dv_r}{dt} = \underbrace{-\frac{3}{4}\omega^2 r}_A + \underbrace{\omega(u_\theta - v_\theta)}_L + \underbrace{-\frac{v_r}{\tau_b} + 2g_r}_{D+B} \quad (3.5)$$

$$\frac{dv_\theta}{dt} = \underbrace{\omega v_r}_L + \underbrace{\frac{u_\theta - v_\theta}{\tau_b} + 2g_\theta}_{D+B} \quad (3.6)$$

where  $A$ ,  $L$ ,  $D$ , and  $B$  represent added mass, lift, drag, and buoyancy effects on the bubble.

The following scales are defined

$$\bar{L} = a_c \quad ; \quad \bar{t} = \tau_b \quad ; \quad \bar{u} = \omega a_c \quad ; \quad \bar{a} = \frac{\omega a_c}{\tau_b},$$

to non-dimensionalize the equations of bubble motion, where  $\bar{L}$ ,  $\bar{t}$ ,  $\bar{u}$ , and  $\bar{a}$  are scales of length, time, velocity, and acceleration respectively. The non-dimensional equations of motion then will be

$$\frac{dv_r^*}{dt^*} = -\frac{3}{4}St \cdot r^* + St \left( \frac{r^*}{2} - v_\theta^* \right) + (-v_r^* + 2g_r^*) \quad (3.7)$$

$$\frac{dv_\theta^*}{dt^*} = St \cdot v_r^* + \left( \frac{r^*}{2} - v_\theta^* + 2g_\theta^* \right) \quad (3.8)$$

In the above equations  $St = \omega \tau_b$  is the Stokes number defined here for the bubbles in the Rankine vortex flow and  $g^* = \frac{g}{\bar{a}}$  is the non-dimensional form of the gravity effect or the ratio of the terminal velocity of bubble to the maximum velocity of the vortex at the core edge. As expected, the new form of the equation shows that the Stokes number is only important on the added mass effect and the lift force.

Final location of bubble in the core can be calculated by setting bubble velocity and acceleration to zero. The static equations in radial and angular direction are

$$0 = -\frac{3St}{4} \cdot r^* + \frac{St}{2} \cdot r^* + 2g_r^* \quad (3.9)$$

$$0 = \frac{r^*}{2} + 2g_\theta^* \quad (3.10)$$

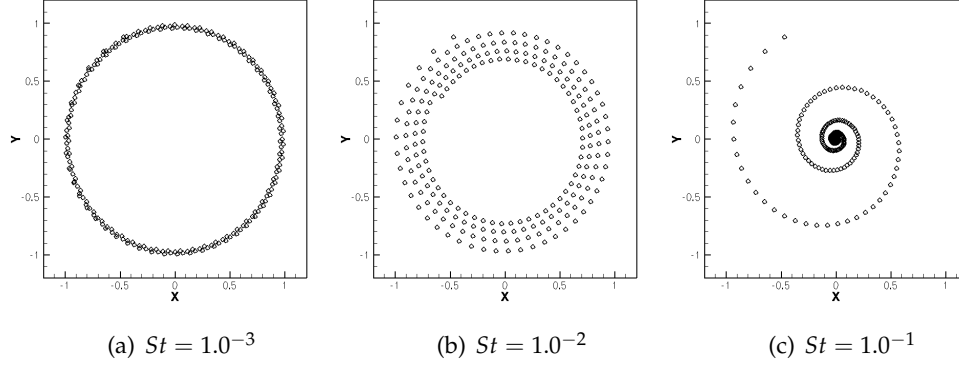


Figure 3.6: Effect of Stokes number on bubble trajectory

Equation 3.9 implies that the added mass, lift, and buoyancy are the active forces in radial direction and added mass together with buoyancy cancels the lift force. Equation 3.10 also shows that in the angular direction only drag and buoyancy effects are present and other forces are not important.

Solving equations 3.9 and 3.10 for  $r^*$  and  $\theta$  gives the final location.

$$r^* = \frac{4g^*}{\sqrt{\frac{1}{4}St^2 + 1}} \quad ; \quad \tan \theta = -\frac{1}{2}St$$

This implies that if the gravity force is negligible, the bubble goes to the vortex center. The interesting result is if the Stokes number is small, the distance is proportional to the gravity and final location is simply  $4g^*$ . Also the angle  $\theta$  is not a function of gravity.

Equations 3.7 and 3.8 are numerically solved to show the effect of Stokes number and gravity on the motion of a single bubble in the Rankine vortex. Bubble is initially located on the edge of the vortex core and  $\theta$  is chosen arbitrarily. The time step in the integration is  $\Delta t^* = 0.01$  and the the final time is  $t^* = 50$ . In this study first the gravity is set to  $g^* = 1.0^{-3}$  and three different Stokes numbers are examined. Figure 3.6 shows the effect of changing Stokes number on the bubble motion. It simply shows that the larger Stokes number is, the faster bubbles go to the center. Bubbles with  $St \sim 10^{-3}$  or less, only circulate around the core and do not cluster in this period of time.

Table 3.2: Rankine vortex configuration

$\Gamma$ (m <sup>2</sup> /sec)	$V_\infty$ (m/sec)	$C_0$ (m)	$a_c$ (m)	$Re_{C_0}$	$\rho_{fluid}$ (kg/m <sup>3</sup> )
1.91511	12.5	0.6096	0.009486	$7.62 \times 10^6$	1000

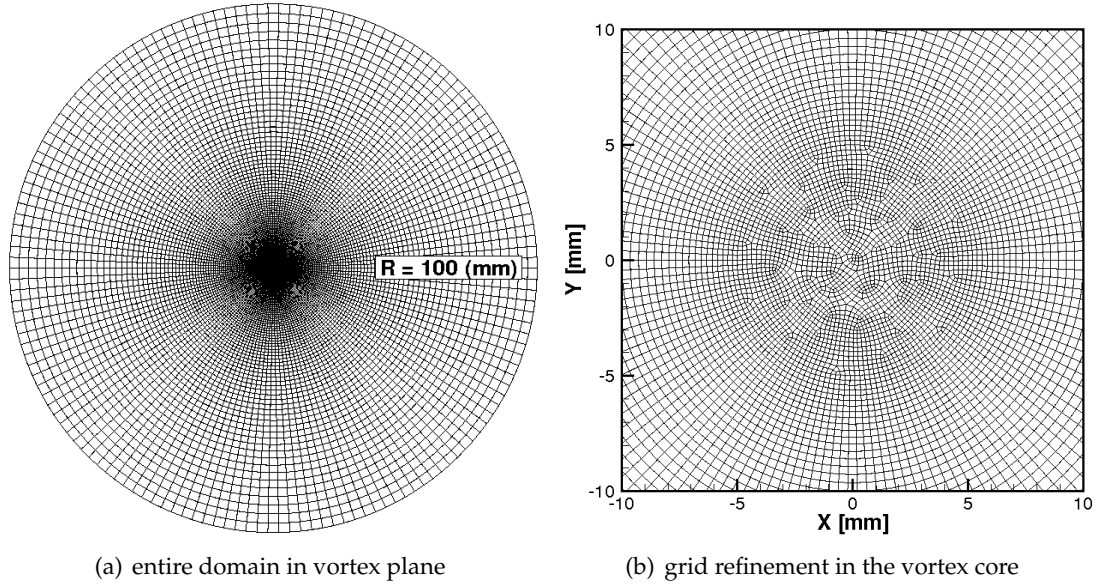


Figure 3.7: Unstructured grid for the Rankine vortex simulations (coarse grid is shown.)

### 3.4.2 Numerical Results

Motion of a single air bubble in a line vortex is simulated using Discrete Bubble Model (DBM). This test case shows the ability of the method in accurate prediction of bubble motion in a relatively complex flow on an unstructured grid. The flow configuration is the same as medium scale vortex used by Hsiao et al. (2003) and listed in the table 3.2. Bubble diameter and density are  $d = 100(\mu\text{m})$  and  $\rho_b = 1(\text{kg}/\text{m}^3)$ , respectively and it is initially located at  $r = 9(\text{mm})$  from the vortex center.

A cylindrical domain is chosen for the computation of vortex. In the cylindrical domain (shown later), flow will receive minimum disturbances from the boundary, compared to a square domain. Unstructured grid is shown in figure 3.7. The grid is generated in three different resolutions for the error calculations and convergence study. Different grid sizes are shown in table 3.3. Boundary conditions are wall on the

Table 3.3: Grid sizes for Rankine vortex simulations

Grid Size	$N_{xy} \times N_z$
small	$118^2 \times 3$
medium	$236^2 \times 4$
large	$472^2 \times 8$

peripheral boundary and periodical on the xy-plane.

Figure 3.8 shows the numerical results for the vortical flow. The numerical simulation results are compared to the Rankine vortex model to calculate the error associated with the single phase flow itself. Figure 3.9 shows  $L2$  norm for error of the horizontal velocity component. The error is simply defined as  $u_{error} = abs(u_{comp.} - u_{model})/u_{max}$ , where  $u_{comp.}$  and  $u_{model}$  are velocity of a particular location from computation and Rankine model (equation 3.3), respectively, and  $u_{max}$  is maximum velocity in the domain.

### 3.4.3 Non-Cavitating Bubble

Trajectory of a single bubble with  $100(\mu\text{m})$  diameter and density of  $1(\text{kg}/\text{m}^3)$  in Rankine vortex is studied here. Bubble is initially located close to the vortex edge at  $r_0/a_c = 0.95$ . The initial velocity is set to the local flow velocity, which is almost the maximum velocity in the domain. Different force models include drag, lift, added mass, pressure, and buoyancy force. It starts moving in a spiral trajectory towards the vortex center, mainly under influence of drag, added mass, and pressure force. Bubble trajectory is shown in the figure 3.10. The figure shows the trajectory from different grid resolutions and also from direct integration of equation of motion using Rankine flow model and same forces. Over most of the trajectory, all three grid resolutions show very close agreement with the direct integration result. But near the vortex center the coarse grid is less accurate, due to insufficient resolution (shown in figure 3.10(b)).

In order to further analyze the trajectory error,  $L2$  error is monitored in figure 3.11. Error is defined as  $r_{err} = abs(r_{comp} - r_{direct})/a_c$ , where  $r_{comp}$ , and  $r_{direct}$  are bubble distance to the vortex center from the computation and direct integration, and  $a_c$  is the vortex core radius. The error is integrated in time to calculate  $L2$  norm.

Another analysis has been done on the accuracy of force calculation. Figure 3.12 shows the error convergence, associated with different forces and the total force acting

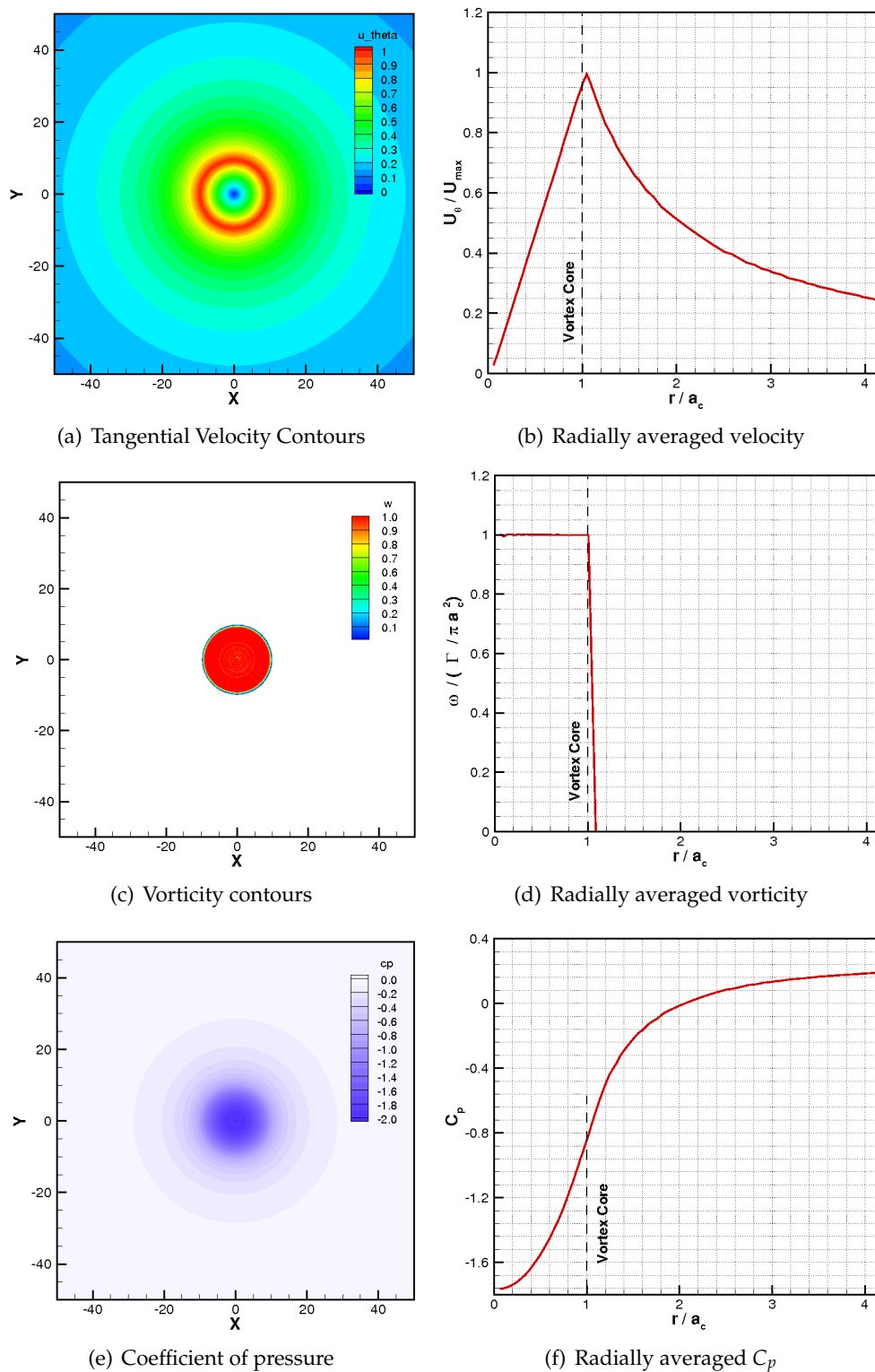


Figure 3.8: Rankine vortex

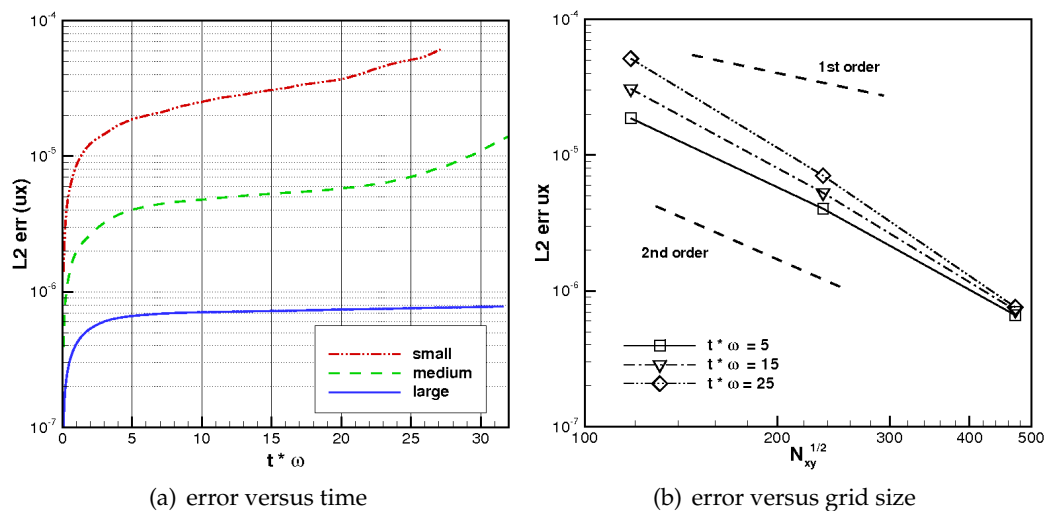


Figure 3.9: Time evolution of L2 error of the horizontal velocity component in Rankine vortex on different grid sizes

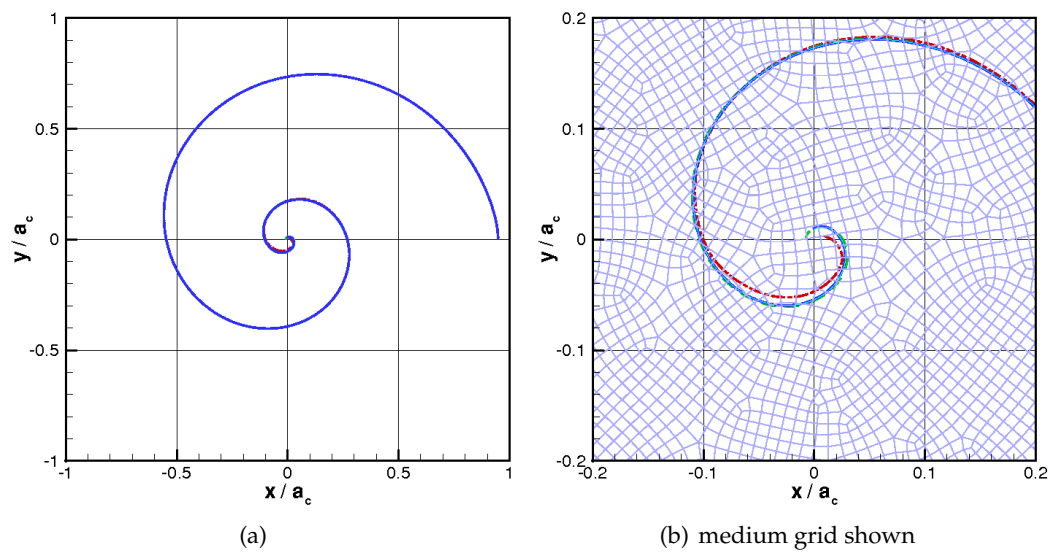


Figure 3.10: Trajectory of single bubble using small (dash-dotted red line), medium (dashed green line), and large (solid blue line), in comparison to the results from direct integration of equations of motion in Rankine vortex model (solid cyan line).

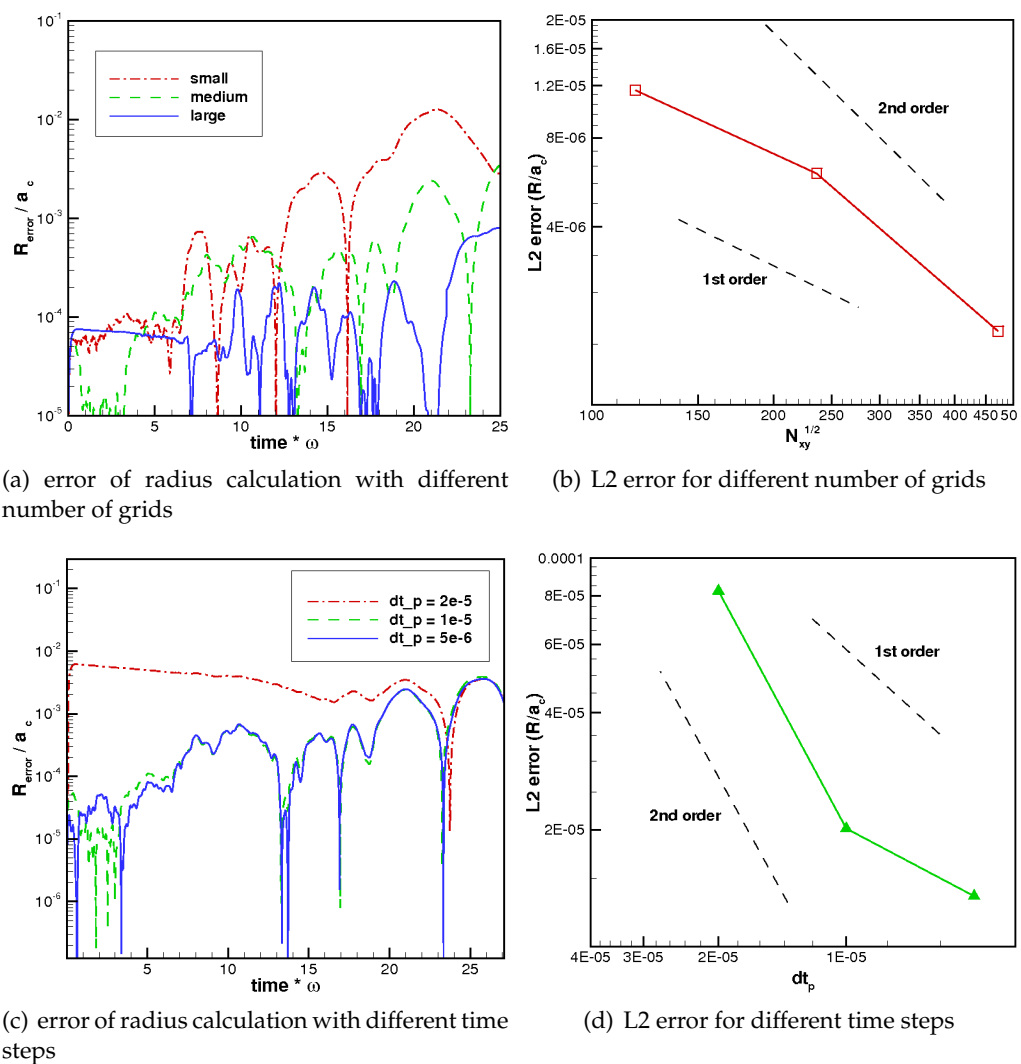


Figure 3.11: Trajectory error for a single bubble in Rankine vortex. Grid sizes found in table 3.3.

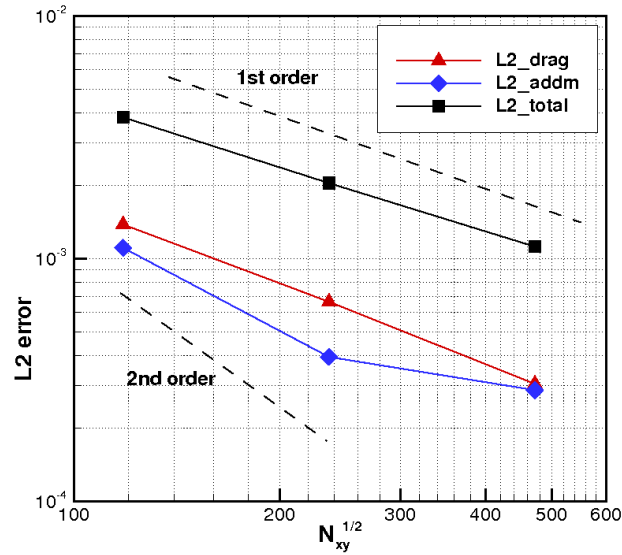


Figure 3.12: Convergence of the force calculation error

on the bubble. The force error is defined as  $F_{err} = abs(F_{comp} - F_{Rankinemodel})$ , where  $F_{comp}$  and  $F_{Rankinemodel}$  are the forces calculated in the computational frame and force calculated from the Rankine model at the same location of bubble. The convergence rate for grid refinement is close to first order of accuracy.

### 3.4.4 Cavitating Bubble

In this test case, we compare trajectories of a single bubble in Rankine vortex, with and without cavitation effect. When the bubble travels to the vortex center, it starts growing due to the decreasing pressure towards the vortex center. Bubble growth changes the effect of different forces in response and the bubble trajectory changes.

Figure 3.13 shows trajectory of a ( $23 \mu\text{m}$ ) bubble with and without cavitation. The bubble moves towards the center very slowly, since the flow acceleration is small at the initial radius ( $r_0 = 2.4a_c$ ). But once it faces a slightly lower pressure region at  $r = 2a_c$ , it starts growing. When the bubble grows the added mass effect and pressure force effect grow and it even accelerates faster towards the center. Once the bubble enters the core, growth continues unrealistically (since there is no feedback effect on the flow in this

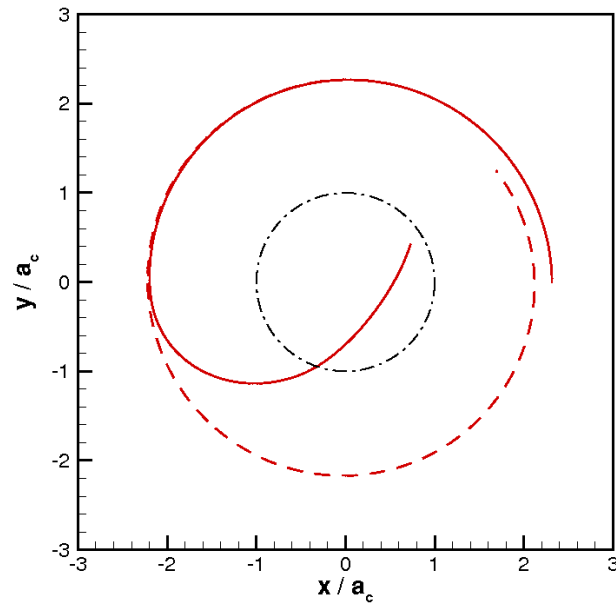


Figure 3.13: Trajectory of cavitating (solid line) versus non-cavitating (dashed line) bubbles in Rankine vortex

simulation to stop the growth) until gravity becomes important and it starts rising.

## Chapter 4 – Bubble Interactions with Vortical Flows

### 4.1 Taylor-Green vortex

Taylor-Green vortex is a two dimensional decaying vortex which has exact solution of Navier-Stokes equations for a single phase, incompressible flow. It is frequently reported as a test case for validation of numerical schemes for single phase flows. The flow velocity components can be derived as:

$$U_x = -\omega_0 \frac{k_y}{k^2} \exp(\nu k^2 t) \cos(k_x x) \sin(k_y y), \quad (4.1)$$

$$U_y = -\omega_0 \frac{k_x}{k^2} \exp(\nu k^2 t) \sin(k_x x) \cos(k_y y), \quad (4.2)$$

where  $\omega_0$  is the initial vorticity,  $k_x$  and  $k_y$  are wave number in  $x$  and  $y$  direction,  $k^2 = k_x^2 + k_y^2$ , and  $\nu$  is the kinematic viscosity.

In a vortical flow, bubbles start migrating to the vortex center, essentially due to added mass and pressure gradient effects. Ferrante and Elghobashi (2007) (referred to as FE07 henceforth) have reported and analyzed effect of micro bubbles on the structure of this vortical flow. Bubbles start migrating in spiral routes towards the vortex centers (high enstrophy regions), principally under influence of the effects from pressure gradient and added mass (in this flow  $D\mathbf{u}/Dt$ ). Bubble concentration in the high enstrophy regions starts growing consequently. This motion modifies the flow field, accordingly. FE07 showed that, micro bubbles with small initial volume fraction ( $\sim 0.01$ ) can remarkably modify the vortex.

In this work, *Case A* from FE07, is simulated with one-way (only momentum from bubbles to liquid), and volumetric coupling (both momentum and volumetric displacement effect from bubble and liquid). Figure 4.1 shows the time variation of bubble concentration at the vortex center in comparison to the results of FE07. Both results from one-way coupling and volumetric coupling are close to those from FE07. The difference may come from different sources due to difference in numerical schemes. One of the possible sources for the difference in concentration, is interpolation method.

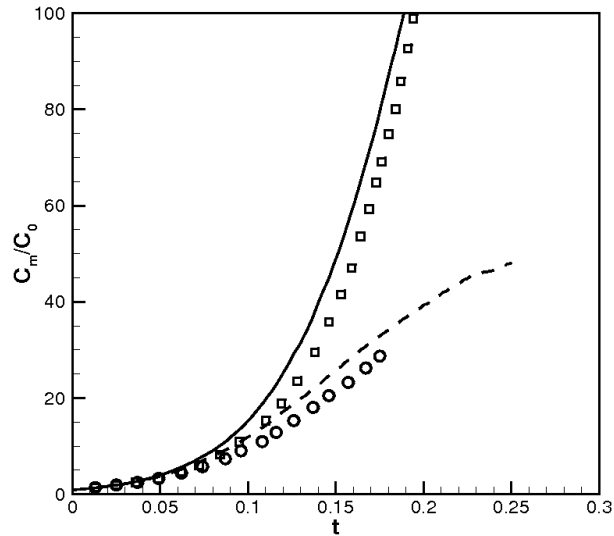
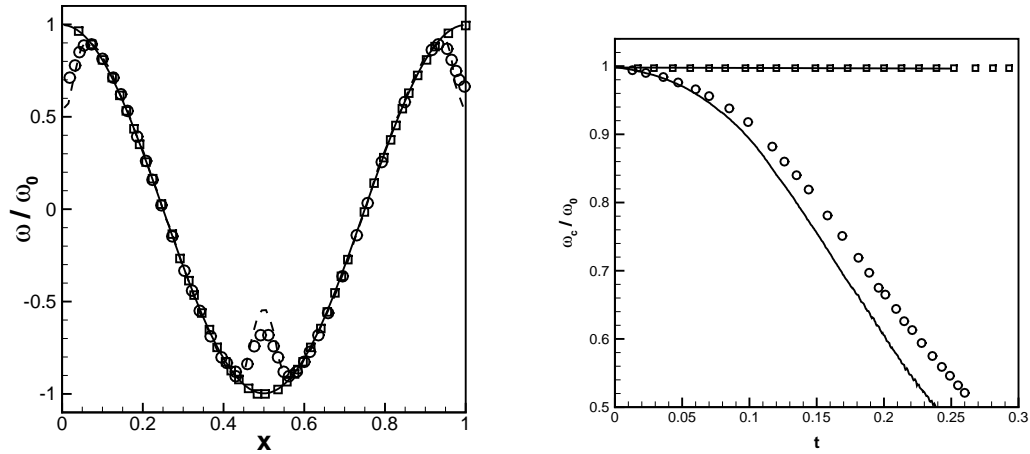


Figure 4.1: Bubble concentration (normalized by maximum initial value) at the vortex center from one-way coupling (solid line), and volumetric coupling (dashed line), in comparison to one-way (squares) and two-way (circles) coupling simulation from FE07 (Ferrante and Elghobashi, 2007).

In this work, Gaussian mollification is used to calculate bubble concentration in each control volume. This technique uses an integration volume larger than a single CV, whereas FE07 loop over particles in a single control volume (Ferrante and Elghobashi, 2005, 2007). Another possible source of inconsistency in results is the time integration method for bubble equation of motion. The way bubbles are handled on the domain periodic boundaries is also different. In this simulation, when bubbles exit from one side, they enter the domain from opposite side, whereas FE07 randomly inject a bubble in the domain for each bubble departure (Ferrante and Elghobashi, 2005).

Vorticity is another quantity which is looked at for comparison to FE07. Figure 4.2 shows the modified flow vorticity in axial direction and in time. One way coupling result, perfectly matches, which shows the consistency in liquid phase calculations.

Material derivative of fluid velocity is believed to be the substantial contributor to the bubble motion towards the vortex centers. The bubble accumulation at vortex centers is a function of the material derivative of fluid velocity. Because of the source term in the momentum equation, the flow acceleration will be different in bubble-laden case.

(a) Axial distribution of vorticity at  $t = 0.2$ 

(b) Time variation of vorticity at the vortex center

Figure 4.2: Flow vorticity (normalized by maximum initial value) from one-way coupling (solid line), and volumetric coupling (dashed line), in comparison to one-way (squares) and two-way (circles) coupling simulation from FE07 (Ferrante and Elghobashi, 2007).

Figure 4.3(a) shows the difference in flow acceleration from one-way coupling model and volumetric coupling.

The source term is essentially the substantial derivative of the fluid concentration. Basically, if the fluid content increases locally, the fluid acceleration will increase. The solid lines in the figure 4.3, show the acceleration and the material derivative of the bubble concentration. It is obvious from the figures that acceleration has changed in the region where  $DC/Dt$  is non-zero. Near the vortex center ( $x \approx 0.5$ ) fluid is accelerating outward, since the bubbles are moving inward.

Pressure is another quantity which is being investigated. Figure 4.4 shows the effect of bubble accumulation on the fluid phase pressure, using volumetric coupling. Pressure in the flow field also changes mainly due to volumetric displacement effect on the flow acceleration.

The effect of bubble motion on the flow pressure is especially crucial in a cavitating case. In this case the pressure has substantially decreased ( $\sim 15\%$ ) near the vortex center. This amount of change in pressure will change the cavitation phenomena.

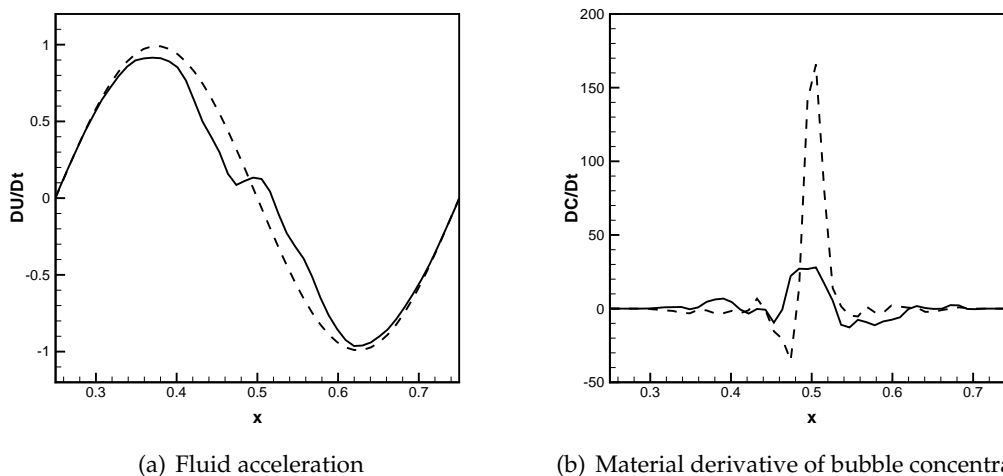


Figure 4.3: Correlation between changes in fluid phase acceleration and material derivative of the bubble concentration at  $t = 0.2$ ; using one-way (dashed lines) and volumetric coupling (solid lines).

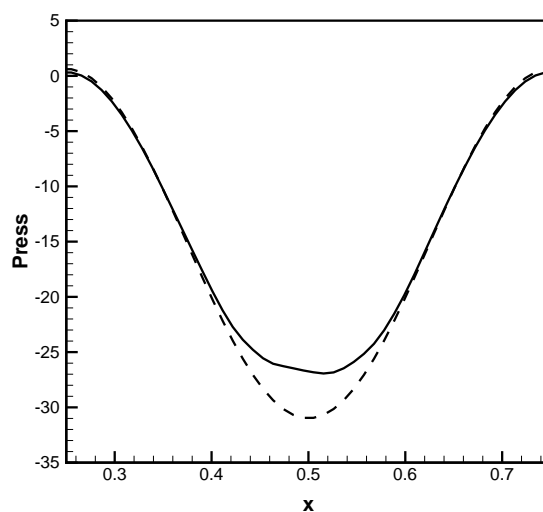


Figure 4.4: Difference in flow pressure, using one-way (dashed line) coupling and volumetric coupling (solid line), at time  $t = 0.5$ .

One of the main intentions of this study is to investigate the possible interactions between the cavitation and bubble accumulation/dispersion, through variation in pressure. It is observed from these cases that, volumetric displacement effect of bubbles, is a major source of these changes, which could only be captured through volumetric coupling model.

## 4.2 Rankine Vortex

### 4.2.1 Numerical Simulations of Bubble-Laden Rankine Vortex

A parametric study on Rankine vortex is presented in this section. Bubble motion in Rankine vortex is explained by showing results of one-way coupling simulation. The results are based on three different parameters,  $St$ ,  $g^*$ , and  $C_0$ , which were defined earlier.

Before starting to present the results of bubble-laden flow, the flow characteristics and simulation methodology are explained. Figure 4.5 shows pressure, vorticity, and flow acceleration in this flow. All parameters are non-dimensionalized as  $\hat{p} = (p - p_\infty) / (\rho a_c \omega_0^2)$ ,  $\hat{\omega} = \omega / \omega_0$ , and  $\hat{D}\mathbf{u}/Dt = (D\mathbf{u}/Dt) / (a_c \omega_0^2)$ , where  $\hat{p}$ ,  $p$ , and  $p_\infty$  are non-dimensional, physical, and reference pressure,  $\hat{\omega}$ ,  $\omega$ , and  $\omega_0$  are non-dimensional, physical, and initial vorticity,  $a_c$  is the vortex core size, and  $D\mathbf{u}/Dt$  is the flow acceleration. Pressure contours are almost circular and the minimum is at the center (figures 4.5(a) and 4.5(b)). Vorticity magnitude is equal to zero outside the core ( $r > 1$ ) and one inside the core. The ideal vorticity curve should change sharply on the core edge, whereas in this simulation there is a small deviation and some spikes can be observed on the edge (figures 4.5(c) and 4.5(d)). Acceleration vectors are always inward, pointing to the center and the maximum magnitude occurs on the edge (figures 4.5(e) and 4.5(e)).

Domain size is 9 times core radius, in the plane normal to the vortex (xy plane). Number of grid points in both x and y direction is 128 and in z direction is 3. Grids are uniformly distributed in each directions. This grid distribution corresponds to at least 27 grid points inside the core. Grid dependency studies showed that this number of grids is enough to resolve the flow in the core (not shown). Boundary conditions are slip-wall in x and y and periodic in z directions.

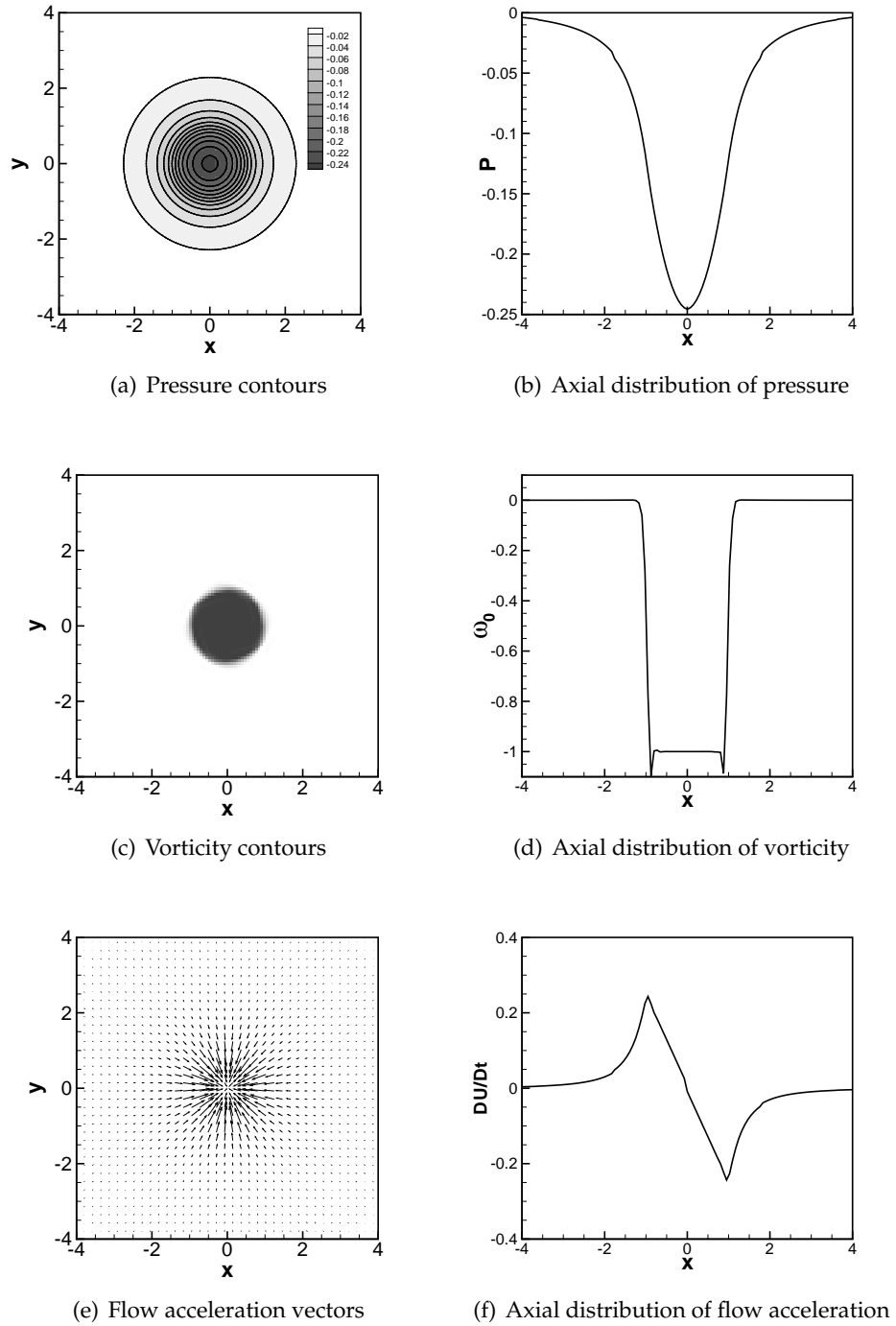


Figure 4.5: Rankine vortex

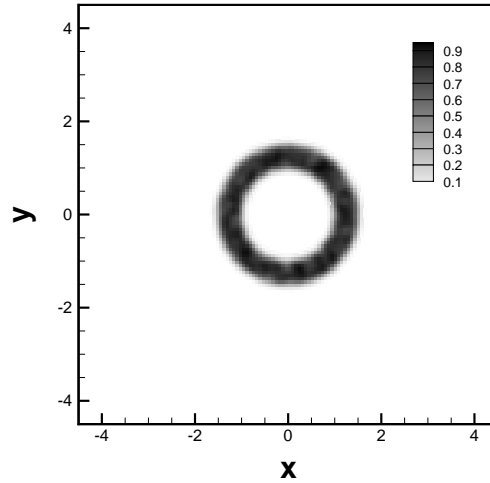


Figure 4.6: Initial distribution of bubbles around the vortex core

Table 4.1: Parameters in Rankine vortex flows

case	$St$	$C_0$	$g^*$	$\omega_0[\text{s}^{-1}]$	$Re_{C_0}$	$d_b[\text{m}]$	$\tau_b [\text{s}]$	$n_b$
<i>A</i>	0.25	0.015	$10^{-4}$	1566	1,957,500	76	$1.60 \times 10^{-4}$	45,000
<i>B</i>	0.5	0.015	$10^{-4}$	2215	2,768,750	90	$2.26 \times 10^{-4}$	27,600
<i>C</i>	1	0.015	$10^{-4}$	3132	3,915,000	107	$3.19 \times 10^{-4}$	16,000
<i>D</i>	1	$1.0 \times 10^{-3}$	$10^{-4}$	3132		107		1,100
<i>E</i>	1	$4.0 \times 10^{-3}$	$10^{-4}$	3132		107		4,000
<i>F</i>	1	$1.6 \times 10^{-2}$	$10^{-4}$	3132		107		16,000
<i>G</i>	0.1	$1.0 \times 10^{-3}$	$10^{-3}$	313		34		72,700
<i>H</i>	0.1	$1.0 \times 10^{-3}$	$10^{-2}$	99		60		11,000
<i>I</i>	0.1	$1.0 \times 10^{-3}$	$10^{-1}$	31		107		1,100

Bubbles are distributed in an annular region around the vortex core. Width of annulus is half of the core size. Figure 4.6 shows the initial distribution of the bubbles around the vortex core (Bubble concentration is normalized by initial concentration).

Table 4.1 shows the parameters related to each setting.

In all these simulations, vortex core size is kept constant and equal to 0.01 [m] and other parameters have been set accordingly to obtain desired Stokes number and grav-

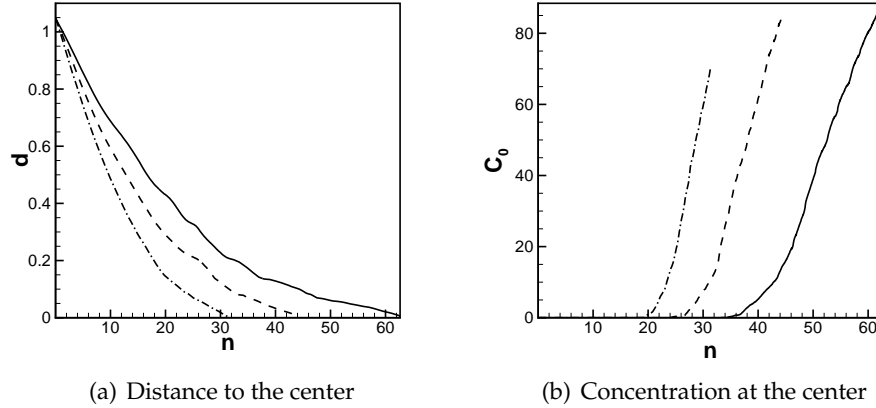


Figure 4.7: Comparing bubble accumulation with different Stokes number at the vortex center for  $St = 0.25$  (solid line),  $St = 0.5$  (dashed line), and  $St = 1.0$  (dash-dotted line).  $n$  is number of vortex revolution,  $d$  is distance to the center normalized by  $a_c$ , and  $C_0$  is the concentration at the center normalize by maximum initial concentration.

ity.

#### 4.2.2 Effect of $St$ and $g^*$ on the bubble accumulation with one-way coupling

In this section the effect of Stokes number and gravity on the bubble accumulation is described. One-way coupling simulations are presented to show the difference between time evolution of concentration at the vortex center and also bubble trajectories.

Figure 4.7 shows the effect of Stokes number on the bubble trajectories and concentration at the center. Different bubbles, which were located initially at the same location, were marked to show how they move differently towards the center. As we expect from theory, bubbles with larger Stokes number move faster to the center, mainly under influence of added mass and pressure gradient effects (not shown in this work). Since the bubble response time  $\tau_b$  and consequently bubble diameter  $d_b$  are increased, the bubbles accelerate faster to the center under reduced drag force and increased net inward acceleration. The rate of change of concentration increases with Stokes number as an outcome of the increased inward acceleration of bubbles, which is shown in figure

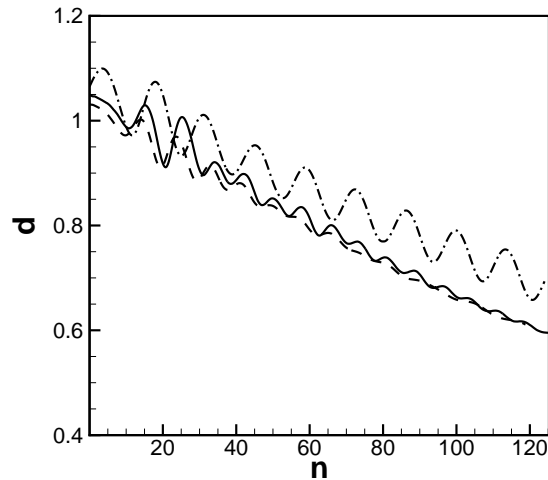


Figure 4.8: Bubble distance to the center for case G (solid line), case H (dashed line), and case I (dash-dotted line).

4.7(b).

In order to study gravitational effect on the bubble motion, non-dimensional gravity  $g^*$  is increased by reducing vorticity and increasing bubble diameter. Gravity is applied in negative  $y$  direction, which generates a body force in the opposite direction on the bubbles. This adds a constant force (if the bubble size does not change) on the bubble, which means oscillating force in radial direction towards the vortex center. The new oscillatory component changes the bubble trajectory (also shown by Sridhar and Katz (1999) in bubble-laden vortex ring).

Figure 4.8 shows how the bubble distance from the center changes. As the gravity effect increases, the bubble undergoes stronger oscillations in trajectory. In case of larger gravity, the bubble may even escape from the vortex core (see Sridhar and Katz (1999)).

### 4.2.3 Coupling Effect on Bubble Concentration

Figure 4.9(a) shows the evolution of bubble concentration at the vortex center for case C. It shows that bubble concentration is different with different coupling models. Two-

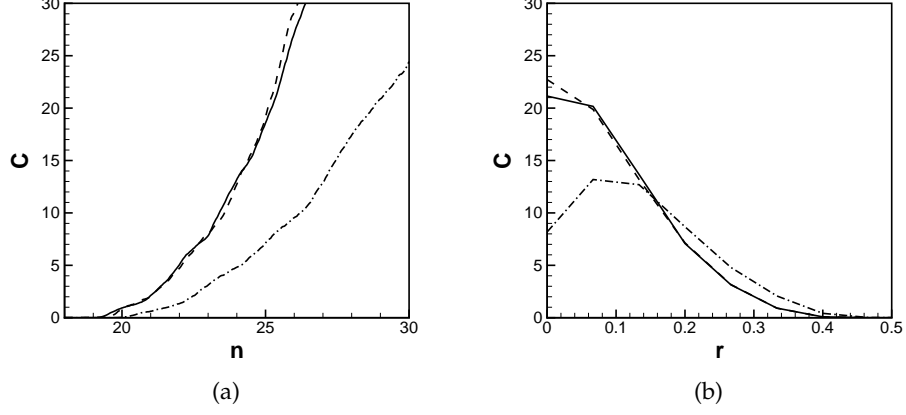


Figure 4.9: Time evolution of the bubble concentration at the vortex center (a) and radial distribution of concentration at time  $n = 25$  for case C (b); with one-way (solid line), two-way (dashed line), and volumetric (dash-dotted line) coupling models.

way coupling slightly increases the bubble accumulation rate, which can be neglected especially before time  $n = 24$ . Volumetric coupling on the other hand, has significantly decreased the accumulation rate at the vortex center. Figure 4.9(b) shows the radial distribution of the bubble concentration after 25 revolution of vortex. This shows almost 8% increase in concentration near the center with two-way coupling but 57% decrease using volumetric coupling. In other words, the results from these two coupling methods are almost 65% different at this certain time and location. Away from the vortex center, one-way and two-way coupling show the same pattern of bubble distribution but volumetric coupling effects are completely different.

A simple analysis on the flow continuity equation may roughly explain how the concentration is changed in volumetric coupling case. Consider equation 2.1 in cylindrical coordinates, defined at the center of vortex:

$$\frac{\partial}{\partial t} (\rho_f \Theta_f) + \frac{1}{r} \frac{\partial}{\partial r} (r \rho_f \Theta_f u_r) + \underbrace{\frac{1}{r} \frac{\partial u_\theta}{\partial \theta}}_{\approx 0} + \underbrace{\frac{\partial u_z}{\partial z}}_{\approx 0} = 0$$

$$\frac{\partial \Theta_f}{\partial t} = -\frac{1}{r} \frac{\partial}{\partial r} (r \Theta_f u_r) \quad (4.3)$$

where  $u_r$ ,  $u_\theta$ , and  $u_z$  are velocity components of liquid phase in cylindrical coordinate, and  $r$  is distance from the origin. Assuming uniform distribution of velocity in azimuthal and vertical directions, the remaining term is radial.

According to the model for the single phase Rankine vortex (equation 3.3), the radial velocity component is zero. Hence, the rate of change of fluid content  $\Theta_\ell$  will be zero. But in the bubbly flow, the concentration will change due to bubble motion (or expansion/contraction/etc.), therefore the right hand side of equation 4.3 can not be zero. One may conclude that in this flow there is a radial component of flow velocity generated by bubble motion.

Figure 4.10 shows the radial velocity component generated by bubble motion in case C at two different time steps. The radial component of velocity from two-way coupling is nearly identical to one-way coupling (zero). Whereas the volumetric coupling has shown significantly different pattern. Generation of new velocity component very well correlates with the rate of change of bubble concentration. Figures 4.10(c) and 4.10(d) show  $D\Theta_b/Dt$  at the same time steps.

Even though the magnitude of the radial velocity component  $u_r$  is very small compared to the maximum velocity magnitude in domain ( $\omega \times a_c$ ), it makes a relatively significant change in the flow acceleration (pressure gradient, vorticity, etc.). The alteration in flow velocity and acceleration is essentially due to the incompressibility of the liquid phase.

Flow acceleration may roughly explain the difference between these results. Flow acceleration ( $D\mathbf{u}/Dt$ ) has the most important effect on the migration of bubbles to the center of vortex (Ferrante and Elghobashi, 2007; Sridhar and Katz, 1999), so it is being studied using these three different coupling methods. Figure 4.11 shows the flow acceleration around the vortex edge ( $0 < r < 2$ ) along with the difference between it and one-way coupling results, at two different time steps. The acceleration is normalized by  $a_c\omega_0^2$ . Radial acceleration has decreased with volumetric coupling and this is not significant with two-way coupling. The radial difference curves show that the radial acceleration may decrease up to 14% of the maximum acceleration which corresponds to 25% of the local acceleration. It is observed that the alteration is much larger at succeeding time steps when the bubble acceleration at the center has increased. Obviously, this variation of  $D\mathbf{u}/Dt$  will change the bubble migration to the center.

The flow acceleration vectors, overlaid by rate of change of bubble concentration

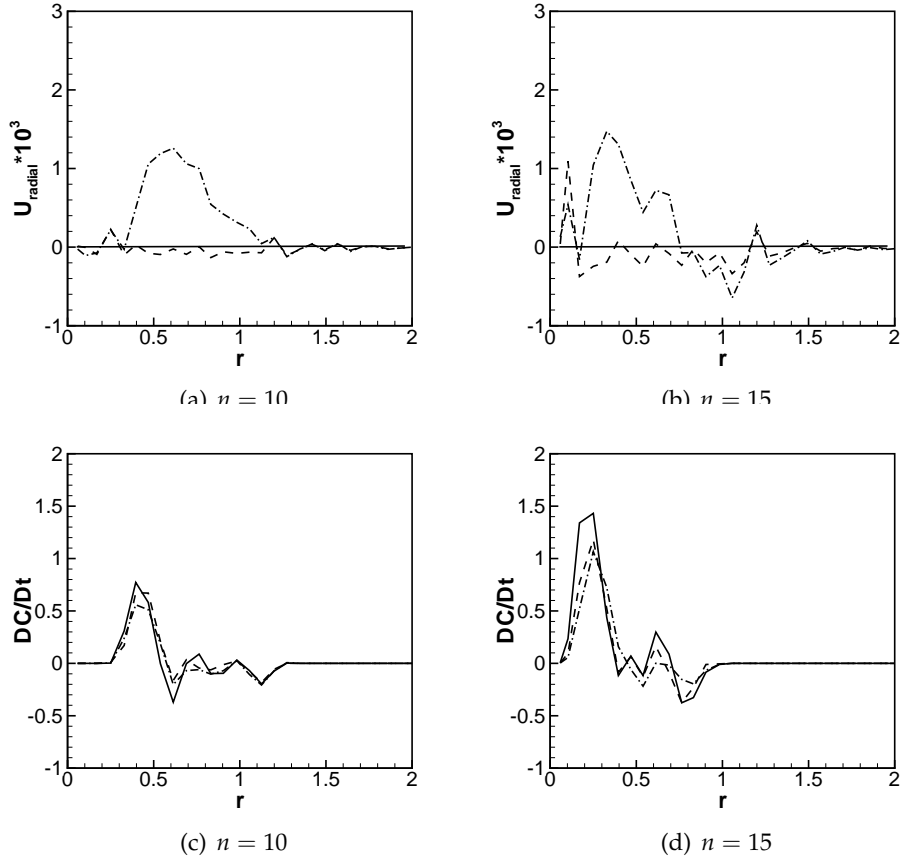


Figure 4.10: Radial velocity component in the Rankine vortex generated by phase coupling effect (a) and (b), and rate of change of bubble concentration in time  $D\Theta_b/Dt$  (normalized by initial concentration  $\Theta_{b,0}$  and bubble response time  $\tau_b$ ); showing one-way (solid line), two-way (dashed line), and volumetric (dash-dotted line) couplings.

are shown in figure 4.12 to give a better insight on the correlation between these parameters. The acceleration vectors are completely deformed in the regions where the  $D\Theta_b/Dt$  is not zero.

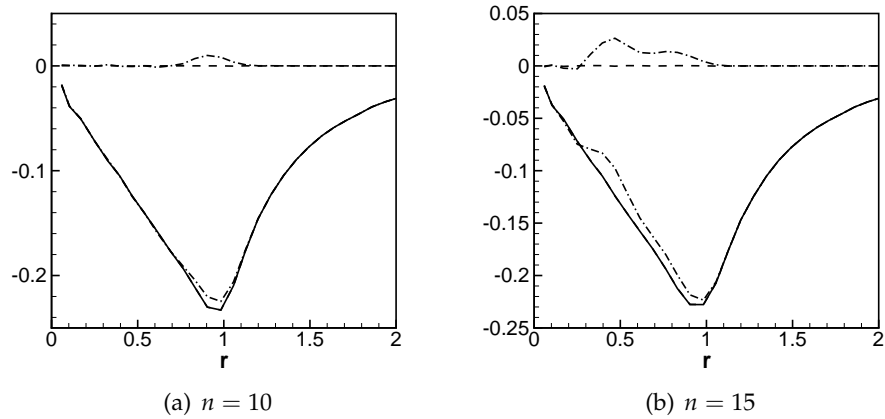


Figure 4.11: Flow radial acceleration (normalized by  $a_c \omega_0^2$ ) and its variation with two-way (dashed line) and volumetric (dash-dotted line) coupling.

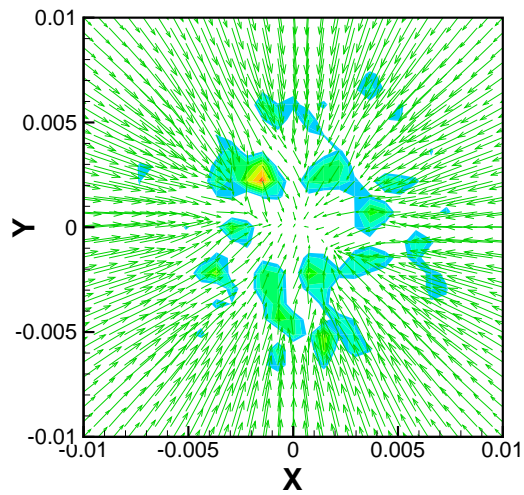


Figure 4.12: Correlation between  $D\Theta_b/Dt$  (contours) and  $D\mathbf{u}/Dt$  vectors in case c at  $n = 15$ , using volumetric coupling.

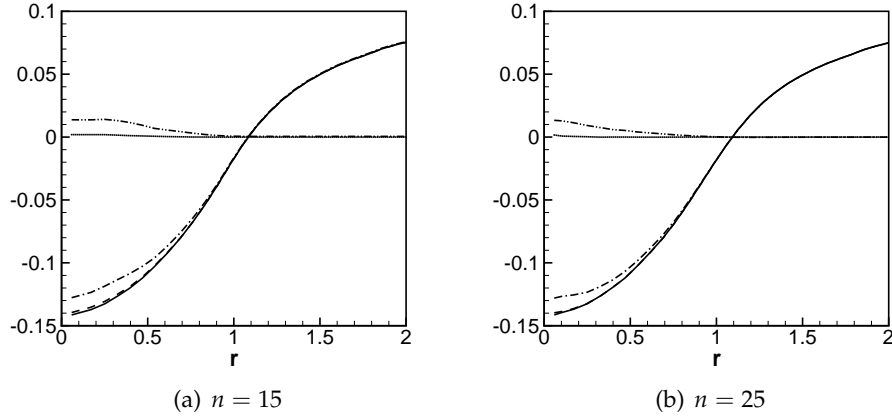


Figure 4.13: Radial pressure distribution with one-way (solid line), two-way (dashed line), and volumetric (dash-dotted line) coupling and the differences with one-way coupling (the curves in the middle). Pressure is normalized as  $\hat{p} = (p - p_\infty) / (a_c \omega_0^2)$ .

#### 4.2.4 Coupling Effect on Pressure

The correlation between bubble motion and pressure variation in bubbly Rankine vortex is being presented in this section. It was shown in the previous section that the flow acceleration is being modified under the influence of bubble accumulation and spatial and temporal variation of bubble/liquid concentration. Changes in acceleration are balanced mainly by pressure gradient on the right hand side of the momentum equation.

This notion is followed to show how the variation in pressure is captured by different coupling models. Figure 4.13 shows radial pressure distribution in the vortex at two different time steps. According to the model the minimum pressure occurs at the vortex center and the maximum is far from the core edge. The volumetric coupling results show slight difference (5-6%) in pressure especially within the core, whereas two-way coupling is almost identical to one-way (Rankine model).

The variation in pressure gradient is more remarkable. Figure 4.14 shows the pressure gradient. At these two time steps, pressure gradient has decreased up to 27% at  $n = 15$  and 50% at  $n = 25$ . This amount of change is only captured by volumetric coupling whereas two-way coupling does not show significant effect.

Luo et al. (2007) have shown the correlation between pressure and particle disper-

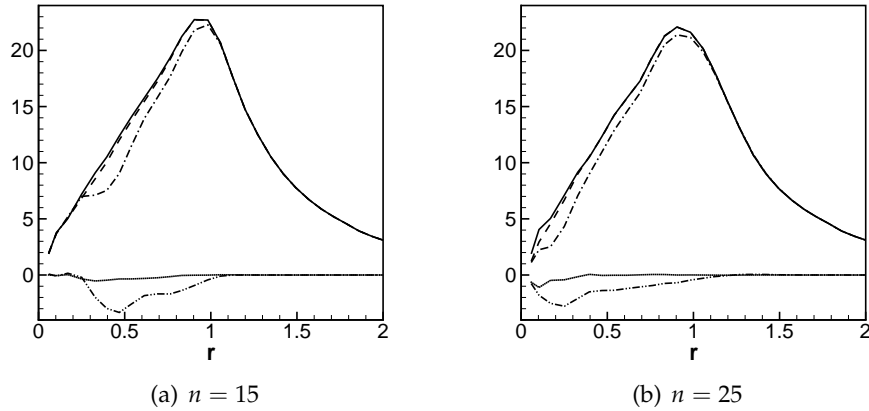


Figure 4.14: Radial distribution of pressure gradient

sion in flow. They have concluded that in particle-laden flow, particle local concentration is well correlated with Laplacian of pressure  $\nabla^2 p$ . The heavy particles in their study accumulate in regions of negative pressure Laplacian  $\nabla^2 p < 0$ . The fraction of bubble number is defined similarly:  $\alpha(\nabla^2 p)$  is the number of bubbles located at a certain  $\nabla^2 p$ , divided by total number of bubbles. In order to calculate  $\alpha$ , the range of variation of  $\nabla^2 p$  (minimum to maximum at each time step) is uniformly segmented.

Figure 4.15 shows the time evolution of  $\alpha$  for each of three coupling methods. The difference between volumetric coupling and two others is even remarkable from the early stages (i.e. figure 4.15(a)). Bubbles are mostly located at the negative  $\nabla^2 p$  which is due to the special form of initial arrangement. Bubbles are distributed in the outer core region, where the Laplacian of pressure is negative according to the Rankine vortex model. They start moving towards the center of vortex, where  $\nabla^2 p > 0$ . This is different from the heavy particle case Luo et al. (2007), where the particles tend to move to the low vorticity regions, which are correlated to  $\nabla^2 p < 0$ . The surprising feature of these figures is the distribution of  $\alpha$  at different time steps with volumetric coupling. Volumetric coupling shows almost invariant distribution of  $\alpha$  in time.

#### 4.2.5 Coupling Effect on flow Vorticity

The next important effect of the bubbles is on flow vorticity. Ferrante and Elghobashi (2007) have shown and analyzed the effect of microbubbles on vorticity of Taylor-Green

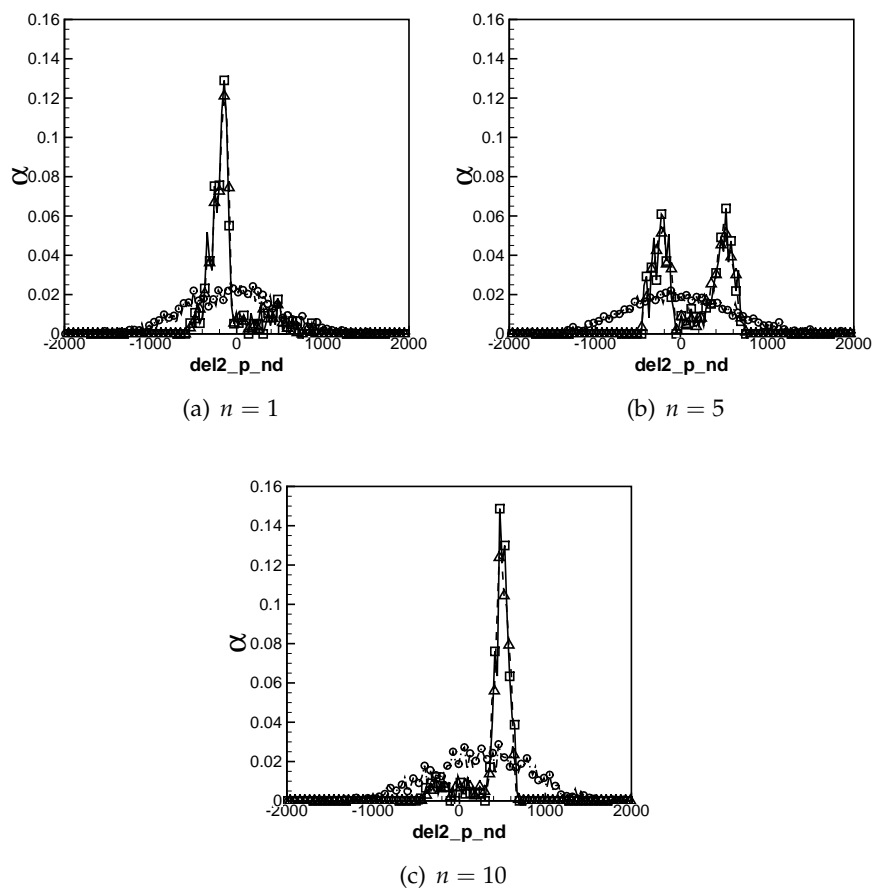


Figure 4.15:  $\alpha$ , using one-way (square), two-way (delta), and volumetric (circle) coupling.

vortex. Their results show that there is a substantial reduction in vorticity magnitude near the vortex center. Their analysis shows that the local non-zero velocity divergence in the flow field, which is generated by bubble motion and correlated with  $D\Theta_b/Dt$ , is the main source of reduction in vorticity. Wherever in the flow field  $\nabla \cdot \mathbf{u}$  is negative, the vorticity increases and vice versa.

Figure 4.16 shows the vorticity at the center of Rankine vortex for case C. The vorticity goes down with volumetric coupling and two-way coupling. There is nearly 12% reduction at  $n = 25$  and then a huge reduction up to more than 30% at  $n = 30$ . The reduction is also being partially captured by two-way coupling through the reaction force.

Figure 4.17 shows the radial distribution of the difference between vorticity of one-way coupling to other coupling techniques, along with the generated velocity divergence  $\nabla \cdot \mathbf{u}$ , from bubble motion. It shows the correlation between reduction in vorticity and generation of  $\nabla \cdot \mathbf{u}$ .

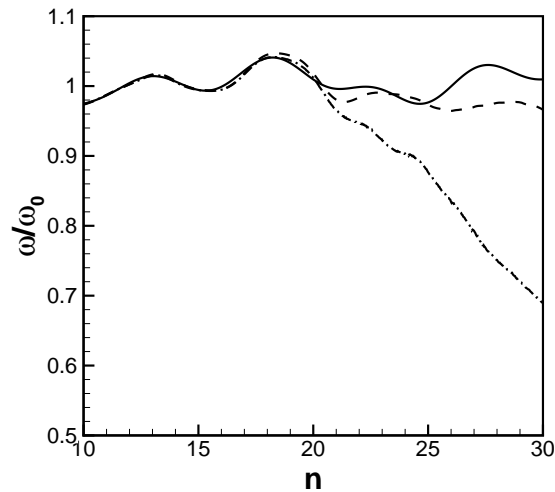


Figure 4.16: Time evolution of vorticity at the vortex center for case C, using one-way (solid line), two-way (dashed line), and volumetric (dash-dotted line) coupling.

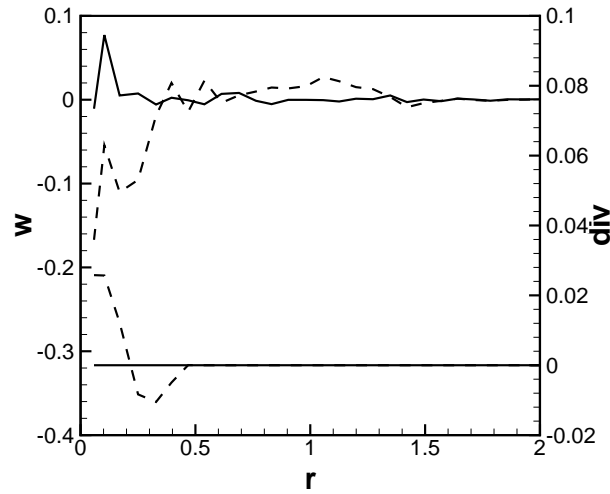


Figure 4.17: Radial distribution of the vorticity difference (upper curves) for two-way coupling (solid line), and volumetric coupling (dashed line) with one-way coupling, along with the velocity divergence  $\nabla \cdot \mathbf{u}$ , at time  $n = 25$ .  $\nabla \cdot \mathbf{u}$  is normalized by  $\omega_0$ .

### 4.3 Summary and Conclusions

Effect of bubble motion on the two vortex flows, including Taylor-Green vortex and Rankine vortex was presented in this work. It was shown that, this effect can mainly be expressed by accounting for volumetric displacement effect of the bubbles on the which was termed as volumetric coupling in this work.

For the Rankine vortex, the investigation started from the bubble concentration at the vortex center. The difference between the results from three different coupling techniques were analyzed by employing the Rankine model to the conservation of mass equation. Generated radial component of the fluid velocity is responsible for the further variations in flow acceleration, pressure gradient, and vorticity. Although the radial component does not have a large magnitude, it generates significant acceleration, in opposite direction of the flow acceleration from model, and reduces the net acceleration to the center. Similar effect is also observed on the pressure gradient. The reduction in pressure gradient changes the bubble migration pattern to the center and rate of change of bubble concentration at the center decreases.

Laplacian of pressure  $\nabla^2 p$  was correlated with the bubble accumulation. The results show that bubbles tend to move to the positive  $\nabla^2 p$  regions where the pressure gradient is minimum. The surprising result from volumetric coupling shows that the bubble number  $\alpha(\nabla^2 p)$  is invariant in time. This means that the bubble motion changes  $\nabla^2 p$  such that there is always a uniform distribution of  $\alpha$  in the flow.

## Chapter 5 – Cavitation Inception in a Turbulent Flow Over an Open Cavity

### 5.1 Introduction

Predictive capability of the bubble cavitation model in a complex flow configuration will be shown in this chapter by studying turbulent flow over an open cavity. Incompressible turbulent flow over cavity has been studied in various geometries and flow configurations (for example Pereira and Sousa (1995); Lin and Rockwell (2001); Chang et al. (2006)). Several flow features of this flow have been reported, such as instability on the shear layer, flow separation from the leading and trailing edges, and flow impingement on the corners. Accurate prediction of flow instabilities in this geometry is an important task in a numerical study.

Cavitation phenomenon has not been studied in this geometry until recently by Liu and Katz (2008). They experimentally studied a highly turbulent flow over a cavity in a variety of Reynolds numbers and cavitation indices  $\sigma$ . Their observations show that cavitation occurs on the cavity trailing edge and shear layer for low  $\sigma$  values. Availability of experimental data from Liu and Katz (2006, 2008), being referred to as LK2008 henceforth, on both velocity and pressure is the uniqueness of this experimental work. Available experimental data on pressure makes it suitable for the cavitation inception studies. Figure 5.1 shows the schematic of the test section from the experiments.

Numerical simulation of cavitation inception in this geometry, using LES technique, is presented in this chapter. Better predictive capabilities of LES, in comparison to other models such as RANS and DES, in modeling turbulent fluctuations helps to more accurately capture cavitation inception. Two different models are used in this study for cavitation inception: (i) a scalar transport model based on the source and sink terms for water vapor (Senocak and Shyy, 2002a), and (ii) cavitation bubble transport model. Scalar transport model captures the vapor generation and destruction due to pressure variation, whereas the cavitation bubble model captures the subgrid dynamics of cavitation. The results are compared against available experimental data.

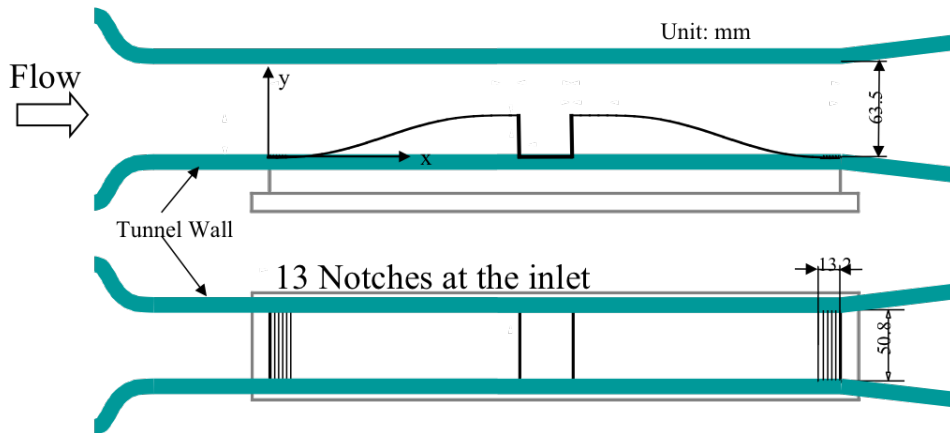


Figure 5.1: Schematic top and side views of the test case for flow over cavity, from the experiments by Liu and Katz (2006, 2008).

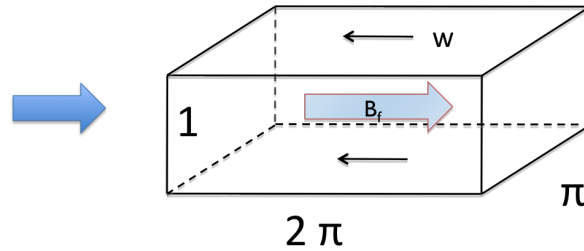


Figure 5.2: Flow in a periodic channel

## 5.2 Turbulent Channel Flow

First a periodic turbulent channel case is being simulated to verify the accuracy of the LES solver. Gullbrand (2000) simulated periodic channel using direct numerical simulation with  $Re_\tau = 395$ . In this section the same case is simulated and being presented as a verification test on the single phase flow using LES. Flow is periodic in stream wise and span wise directions and wall-bounded in vertical direction. Figure 5.2 shows the schematic case setup. Computational setup is being shown in the table 5.1. The smallest grid in the wall normal direction is 0.81 wall units.

In order to maintain turbulence level, a body force based on the constant mass flow

Table 5.1: Computational domain and grid size (+ denotes wall units) for the periodic channel (verification case).

Channel size		$2\pi \times 1 \times \pi$	
Grid resolution		$64 \times 49 \times 48$	
$\Delta x_{min}$ ,	$\Delta x_{min}^+$	$98.17 \times 10^{-3}$ ,	38.8
$\Delta y_{min}$ ,	$\Delta y_{min}^+$	$2.05 \times 10^{-3}$ ,	0.81
$\Delta z_{min}$ ,	$\Delta z_{min}^+$	$65.45 \times 10^{-3}$ ,	25.8

rate in the channel is applied on the flow in stream wise direction.

Figure 5.3 shows the mean stream wise velocity component and *rms* of all three velocity components. The results match well with the same reported values by Gullbrand

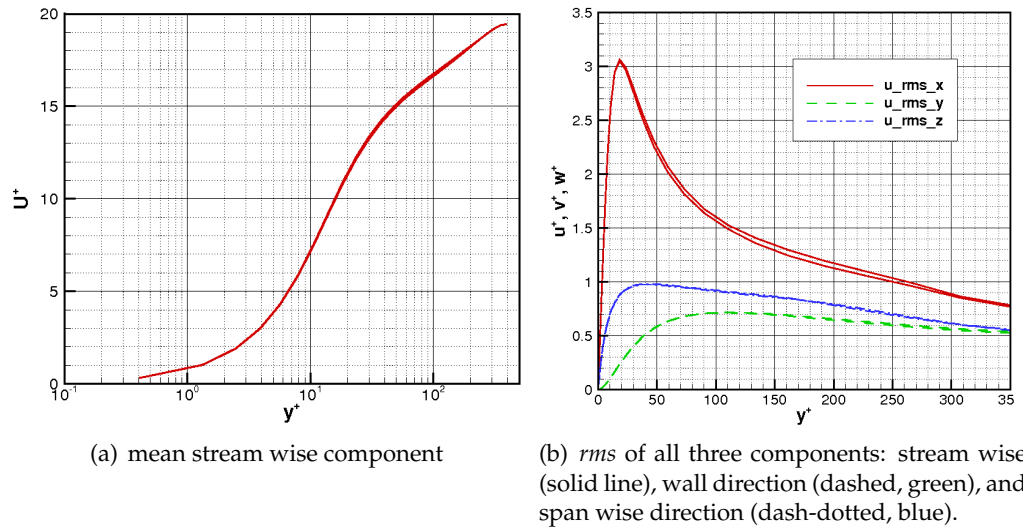


Figure 5.3: Velocity in a periodic channel flow with  $Re_\tau = 395$ .

(2000).

### 5.3 Numerical Setup for Flow Over Cavity

The numerical setup consists of a straight ducted channel with a nearly square cavity in the central region as shown in figure 5.4. To keep the computational size small, only up to the half duct height is simulated. Emphasis is placed on the shear layer and

the leading and trailing edges of the cavity, with refined grids in these regions. The computational domain includes the cavity and the duct flow which starts at  $-12.4$  mm before the cavity leading edge and ends at  $32$  mm after the trailing edge.

Flow properties are shown in table 5.2. Upstream flow coming to the cavity section is highly turbulent. The average velocity is  $\overline{U_\infty} = 5.175$  m/s, which corresponds to Reynolds number of 170,000. Friction velocity,  $u_\tau = (vdu/dy)^{1/2} \approx 0.596$  m/s, is approximated from experimental results for mean stream-wise velocity distribution near the inlet.

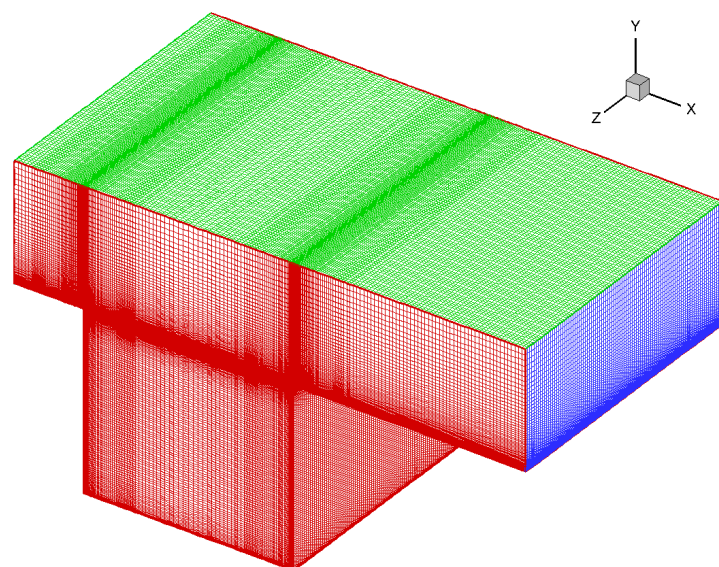
Table 5.2: Properties for flow over cavity (+ denotes wall units,  $y^+ = yu_\tau/\nu$ ).

Average inflow velocity	$\overline{U_\infty} = 5.175$ m/s
Kinematic viscosity	$1.121 \times 10^{-6}$ m <sup>2</sup> /s
Reynolds number	$Re_L = 170,000$
Vapor pressure	$P_v = 2.337$ kPa

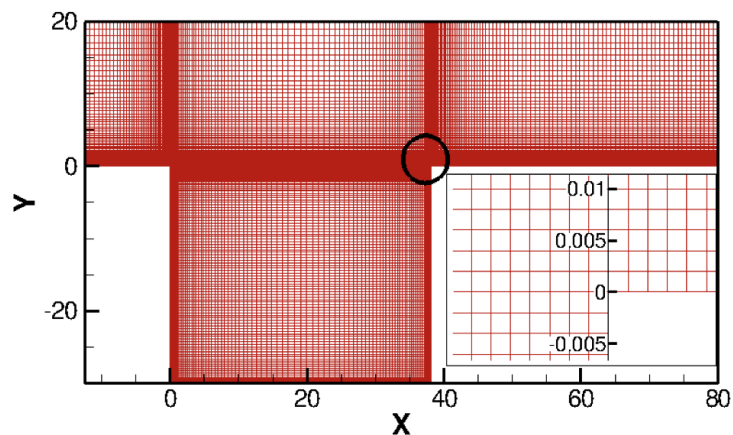
Table 5.3: Cavity geometry and computational grid (+ denotes wall units,  $y^+ = yu_\tau/\nu$ ).

<b>dimensions</b>	Cavity size	$38.1 \times 30 \times 50.8$ mm <sup>3</sup>
	Channel size	$92.4 \times 20 \times 50.8$ mm <sup>3</sup>
	Cavity length $L$	38.1 mm
<b>base grid</b>	$\Delta x_{min} = \Delta y_{min}$	1.9 $\mu$ m
	$\Delta x_{min}^+ = \Delta y_{min}^+$	1.1
	$\Delta z$ & $\Delta z^+$	500 $\mu$ m, 208
	Total grid points	5 million
	Simulation time step	$\Delta t_{solver} = 10^{-7}$ s
<b>coarse grid</b>	$\Delta x_{min} = \Delta y_{min}$	3.8 $\mu$ m
	$\Delta x_{min}^+ = \Delta y_{min}^+$	2.2
	$\Delta z$ & $\Delta z^+$	1000 $\mu$ m, 416
	Total grid points	600,000
	Simulation time step	$\Delta t_{solver} = 2 \times 10^{-7}$ s
<b>fine grid</b>	$\Delta x_{min}$	10 $\mu$ m
	$\Delta x_{min}^+$	5.8
	$\Delta x_{min}$	2 $\mu$ m
	$\Delta x_{min}^+$	1.15
	$\Delta z_{min}$ & $\Delta z_{min}^+$	200 $\mu$ m, 83.2
	Total grid points	7.5 million
	Simulation time step	$\Delta t_{solver} = 10^{-7}$ s

Fine grid is mainly refined in spanwise direction.



(a) 3D View



(b) Symmetry Plane

Figure 5.4: Computational domain and grid: (a) three-dimensional domain with Cartesian grid, (b) refined grids (dimensions shown are in mm) are used in the shear layer and near the cavity leading and trailing edges. A zoomed-in view of the grid near the trailing edge is shown in wall co-ordinates.

Table 5.3 gives the details of the computational domain size and the grid resolutions. The grid elements are mainly Cartesian hexahedra with refined regions in the leading edge and near wall regions. The wall-layers in the leading and trailing edges are resolved. The base computational grid consists of 5 million elements. This flow is also simulated over a coarser and a finer grid in order to show the grid independency of the results. The coarse grid is simply twice coarser in all three directions and grid distribution is quite similar to the base grid. The fine grid, however, is mainly refined in the spanwise direction to show the effect of under resolved structures in this direction. It is more than twice finer in the mid-section ( $-12\text{mm} < z < +12\text{mm}$ ) in this direction and is coarsened near the walls. The grid coarsening is, however slower in the flow direction and on the shear layer, which is believed to help capture more instability and vortical structures on the layer. The simulation on the fine grid is still in progress and results are not presented in this document.

### 5.3.1 Boundary Conditions

In the present simulation, the wall layers are resolved, and no-slip conditions are applied at all walls. A convective outflow boundary condition is applied at the outlet. In the experimental setup, the upstream region of the duct consists of a convergent section near the bottom wall and the flow is tripped using thirteen notches to create turbulence (Liu and Katz, 2008). The divergent section is not simulated in the present study. Instead, it is assumed that the flow is fully developed and the experimentally measured mean velocity field in the symmetry plane is used to specify the inlet conditions.

To create proper turbulence structures, a separate periodic flow in a duct is simulated at the desired mass-flow rate and Reynolds number using a body-force technique (Pierce and Moin, 1998). Resolved LES of a periodic duct flow on  $180 \times 256 \times 144$  grid points with the resolution of  $\Delta x^+ = 64$ ,  $\Delta z^+ = 42$ , and  $\Delta y_{min}^+ = 0.835$ ,  $\Delta y_{max}^+ = 85$  (where the superscript '+' denotes wall variables) is performed. Figure 5.5 shows the comparison of the vertical variations of mean and *rms* axial velocity field in the symmetry plane with the experimentally measured inlet flow. A reasonable agreement is obtained for the *rms* fluctuations; however, the mean flow shows much higher shear in the experiment than those obtained from the simulations.

The vertical velocity component in the experiment is also significant at the inlet.

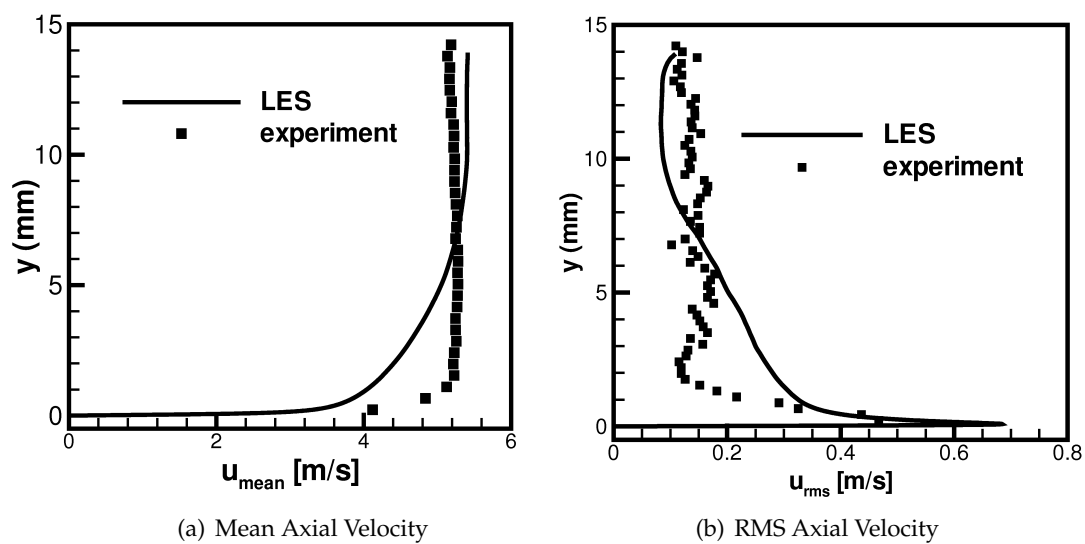


Figure 5.5: Comparison of vertical variations of mean and *rms* axial velocity fields in the inflow section (obtained from a stand-alone LES computation of a periodic duct flow) with the experimental data (Liu and Katz, 2008). For inlet conditions, the mean velocity from the experiment and fluctuating velocity field from the periodic duct flow are used.

Downward velocity is generated at the test section inlet, as the effect of convergent ramp in the upstream. In order to better match the inflow velocity boundary condition with the experiment, mean velocity field from the experiments and the instantaneous velocity fluctuations from the periodic duct flow are used:

$$u_i^{\text{inflow}} = (u_i^{\text{periodic duct}} - \overline{u_i^{\text{periodic duct}}}) + \overline{u_i^{\text{experiment}}}, \quad (5.1)$$

where  $\overline{(\ )}$  in the above expression denotes time-averaged quantity. The superscript ‘periodic duct’ stands for flow field from the highly resolved periodic duct flow. This inflow data over several flow through times is generated *a priori* and read at each time step to specify the velocity components at the inlet.

This technique ensures that the fluctuating velocity field at the inlet section is divergence-free. The effectiveness of the inflow velocity fluctuations in predicting the flow statistics downstream will be shown later. In order to obtain good predictions from the LES computation, an accurate estimation of the inflow conditions is necessary. With this approach, the inflow conditions are better represented in the computations. The predictive capability of LES can now be tested by comparing the flow features and turbulence statistics with the experimental data.

## 5.4 Flow Velocity Statistics

Flow field statistics are collected over 7.5 flow through time (FTT). FTT is calculated as  $FTT = L/U_{\text{freestream}} = 7.36$  ms, where  $L$  is the cavity length and  $U_{\text{freestream}}$  is the free stream convective velocity. Figure 5.6 shows the convergence of flow mean velocity components over the simulation period (7.5 FTT). It shows a relatively stationary state of statistics, especially in the regions of interest, which are the leading edge, shear layer, and trailing edge. Mean stream-wise velocity component  $\overline{u}$  shows better convergence behavior, compare to the vertical component, especially on the shear layer (see figures 5.6(c) and 5.6(d)). Velocity statistics is weakly converged inside the cavity, which is not of the interests in this study. Large vortical structure inside the cavity slowly interacts with the shear layer instabilities and vortex shedding from the leading and trailing edges. It means that a much longer simulation may be needed to resolve all the time scales associated with the flow inside the cavity.

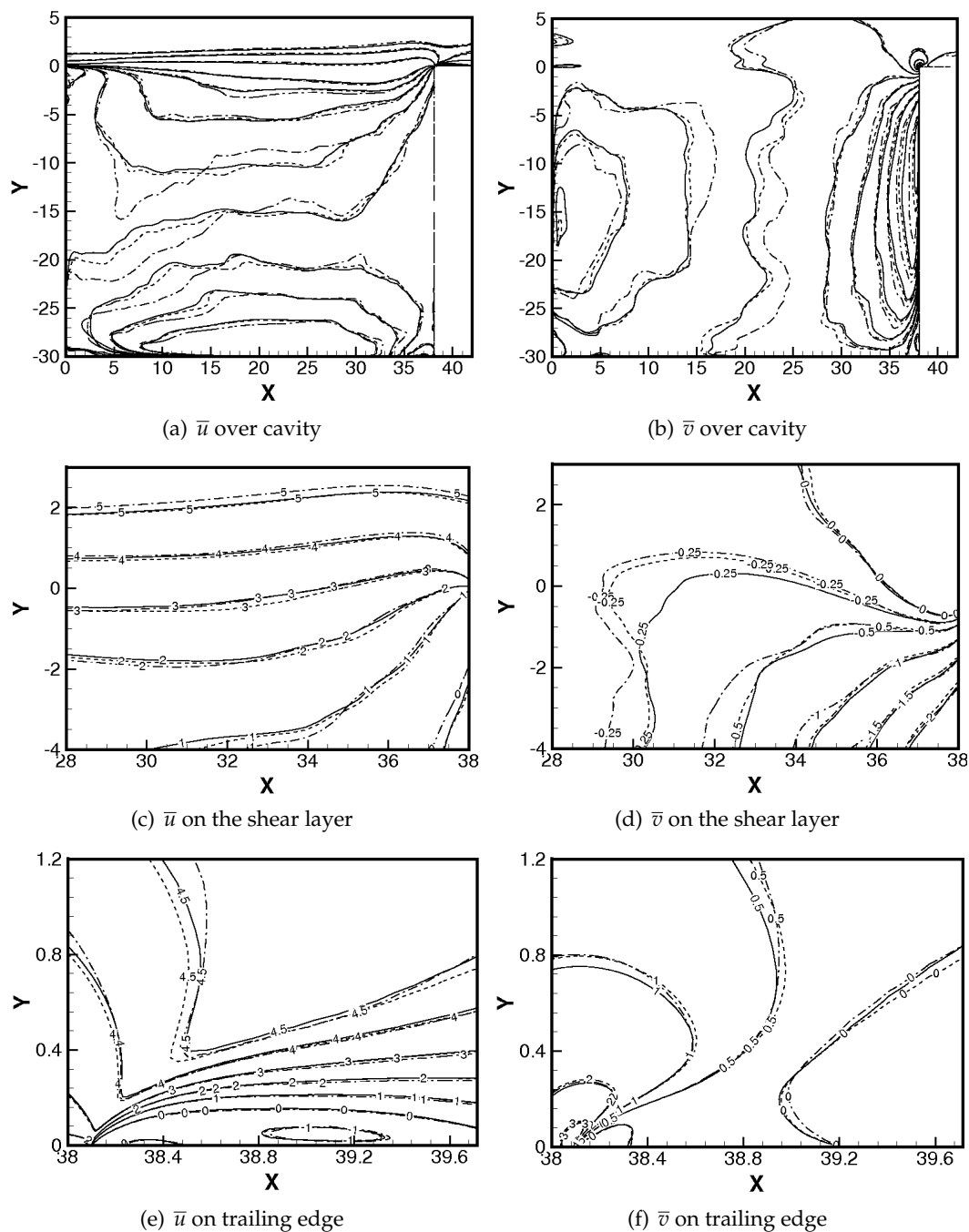


Figure 5.6: Convergence of mean velocity, showing contour lines of time-averaged velocity components at different time snaps corresponding to 3.9 (dashed-dotted), 5.9 (dashed), and 7.5 (solid) flow-through-times, calculated based on the cavity length and free stream velocity.

Flow statistics obtained from the simulation, including mean and *rms* values of the flow field, are first compared to those reported in LK2008. Detailed comparisons of flow statistics between LES and experimental data are presented. Comparisons are performed at three different sections, including leading edge, shear layer, and trailing edge.

### 5.4.1 Leading Edge

Effect of imposed inflow fluctuations at the inlet boundary, on improving the velocity statistics is shown in this section. Also, in order to show the level of grid dependency of the simulation, the results are compared to another simulation on a twice coarser computational grid.

Figure 5.7 shows comparison of the vertical variations in the mean and *rms* axial velocity field near the leading edge with the data of LK2008. LES predictions with and without inlet velocity fluctuations are shown at three different locations. The mean flowfield is reasonably well predicted by both computations. It is slightly better predicted when only the experimental mean flow was used (without any fluctuations). However, the *rms* velocity fields are much better represented by LES with inlet flow fluctuations. Specifically, the *rms* fluctuations disappear away from the wall in the absence of imposed inflow fluctuations.

The experimental data as well as LES with inflow fluctuations show substantial turbulence further away from the wall. The distribution of the *rms* velocity fields are also better predicted by the LES with inflow fluctuations. It was observed that with no fluctuations at the inlet, flow structures above the shear layer generally predicted very low levels of turbulence. Accurate characterization of the inlet flow fluctuations are thus found to be important. An LES simulation inclusive of the upstream divergent section at the bottom wall of the duct may provide even better inflow conditions.

Figure 5.8 shows the effect of grid refinement of the velocity statistics. There is a small improvement in the mean velocity distribution from LES with the finer grid. It seems to be more effective as we approach the leading edge. RMS values, however, show more substantial dependence on the grid resolution. Better agreement achieved with the finer grid, especially away from the boundary layer edge.

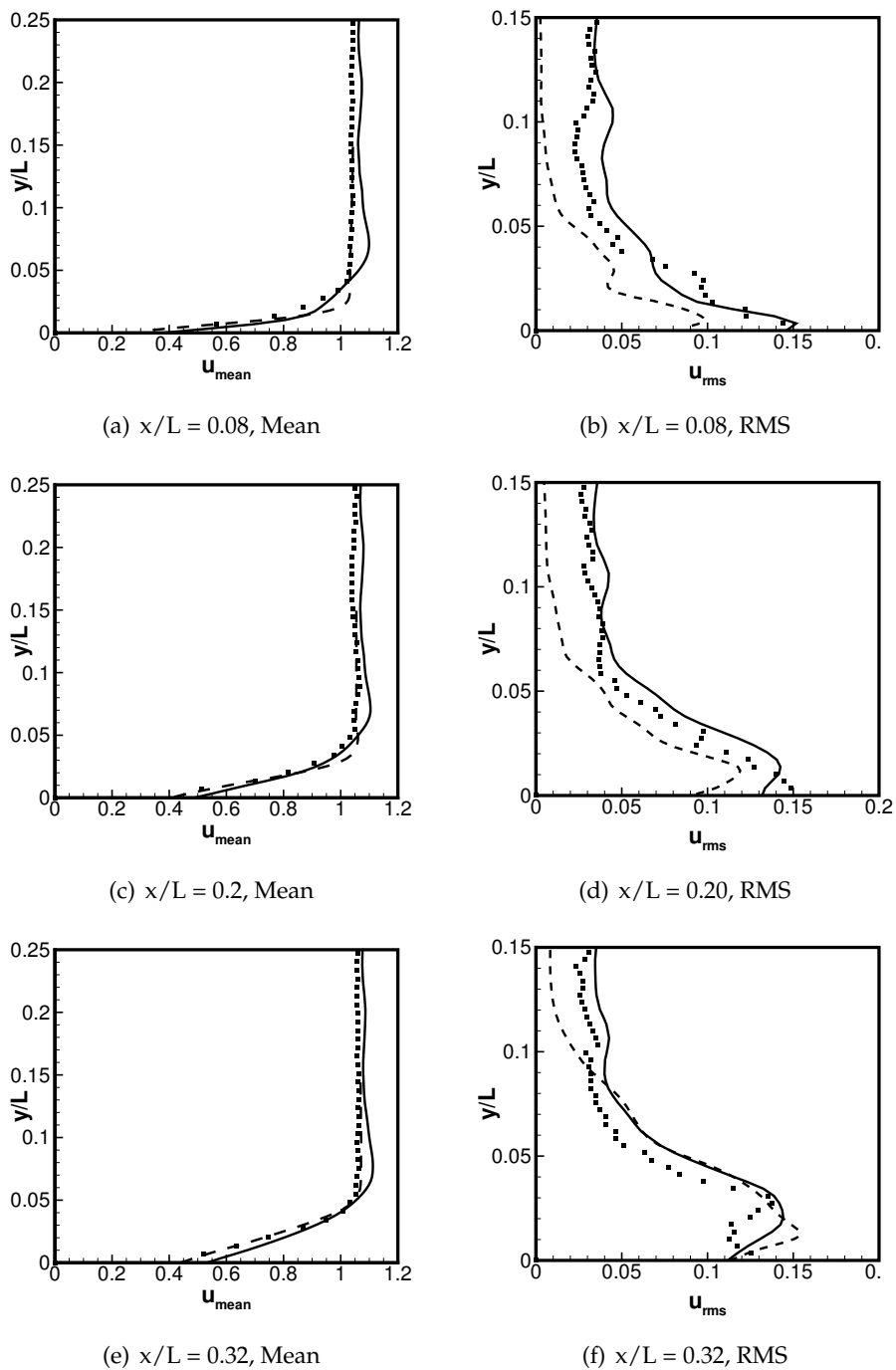


Figure 5.7: Comparison of vertical variations of mean and *rms* of stream-wise velocity component near the leading edge with (solid lines) and without (dashed lines) inflow fluctuations with the experiment data of LK2008 (symbols).

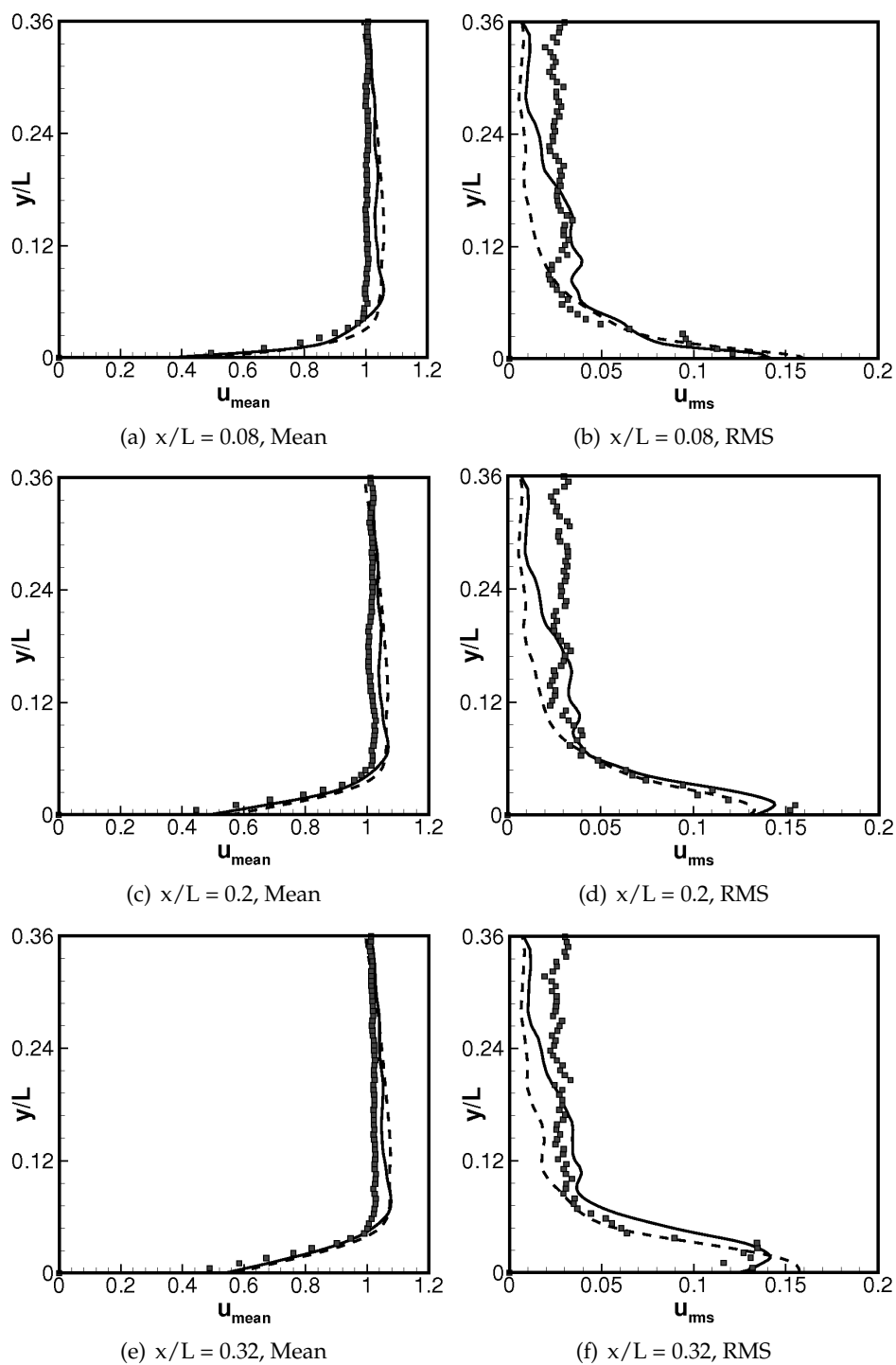


Figure 5.8: Effect of grid refinement on the mean and *rms* of stream-wise flow velocity component. Shown in the figures are the results from the base (solid line), coarse (dashed line) computational grid, and experimental results (symbols).

### 5.4.2 Shear Layer

Cavitation has been observed in the shear layer region of this geometry, in the work of LK2008. They have reported unsteady cavitation occurring frequently on the shear layer, which is believed to happen due to large pressure fluctuations. This section shows the accuracy of prediction of velocity mean and rms, on the shear layer.

Figure 5.9 shows the comparison between velocity statistics from LES and experimental results from LK2008. It shows good agreement of the contour lines of the normalized mean velocity ( $\bar{U}/U_\infty$  and  $\bar{V}/U_\infty$ ) on the shear layer (figures 5.11(a) and 5.11(b)). Deviation from the experimental results are more pronounced inside the cavity and away from the shear layer. This is possibly because the statistics collection time is not long enough in this simulation to resolve the very large time scale inside the cavity as shown the earlier section. However, large amount of velocity fluctuation is predicted very well on the shear layer (figure 5.11(c) and 5.11(d)). Accurate prediction of fluctuations is important in cavitation modeling. Figure 5.10 also shows the distribution of these quantities in flow normal direction at two different stream-wise sections on the shear layer.

### 5.4.3 Trailing Edge

Contour plots of the normalized mean axial velocity ( $\bar{u}/U_\infty$ ) and vertical velocity ( $\bar{v}/U_\infty$ ) are presented in figure 5.11. Also shown in figure 5.12 are the distribution of axial velocity in the vertical direction near the trailing edge compared to the data of LK2008. The distribution of the mean velocity field is very similar to that shown by LK2008. It is observed from the mean streamtraces that the shear layer impinges the trailing edge slightly below the corner. The LES results predict the behavior of the mean axial velocity reasonably well above the trailing edge. Upstream of the trailing edge (inside the cavity), the experimental data indicates slightly lower axial velocity than those predicted by the LES ( $x/L = 0.8, 0.9$ ). A more refined grid in the axial direction over the entire shear layer may be necessary to capture the high shear in this region.

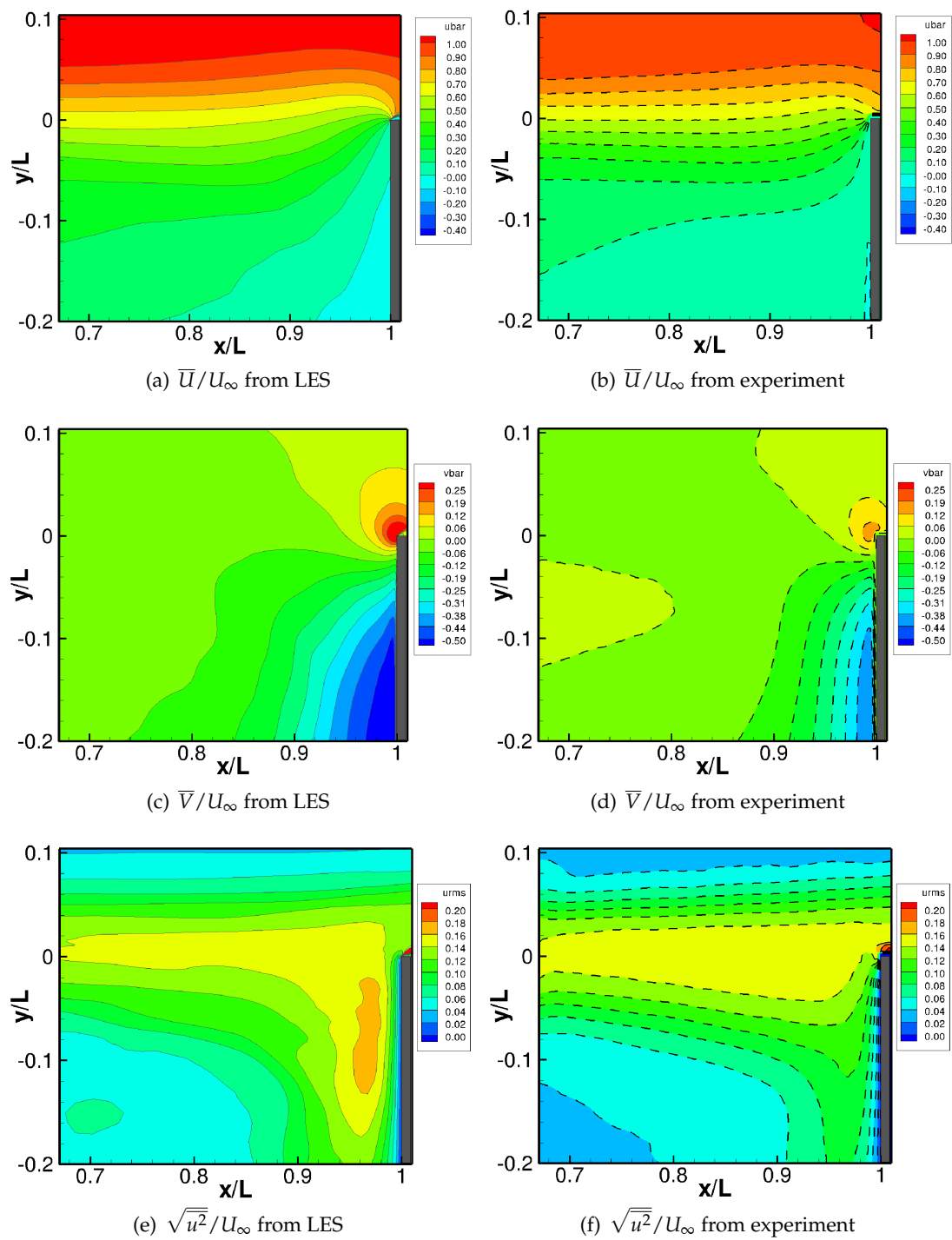


Figure 5.9: Cont'd on the next page.

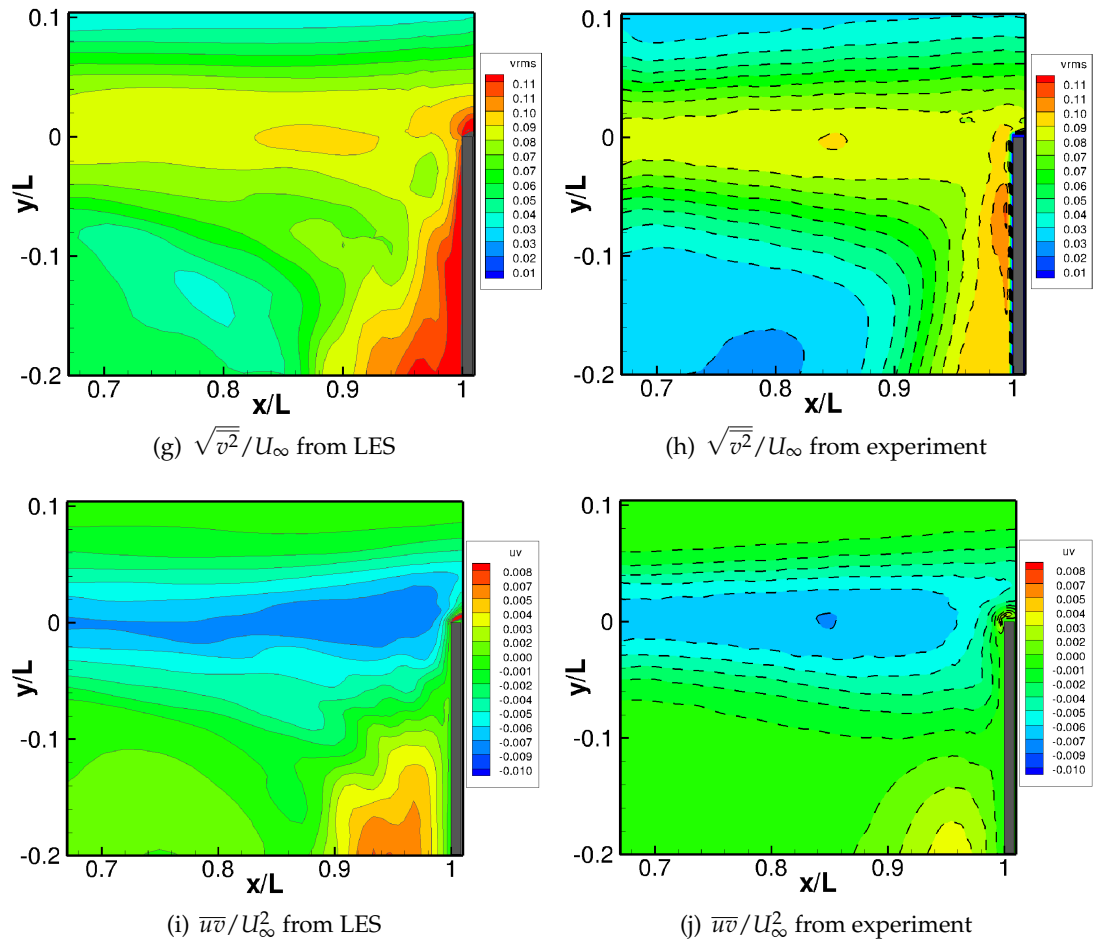


Figure 5.9: Contours of flow velocity statistics on the shear layer, showing mean ( $\overline{U}/U_\infty$  and  $\overline{V}/U_\infty$ ), rms ( $\sqrt{u^2}/U_\infty$  and  $\sqrt{v^2}/U_\infty$ ), and Reynolds Stress ( $\overline{uv}/U_\infty^2$ ) from both LES (color contours), and experimental data (dashed contour lines) from LK2008.

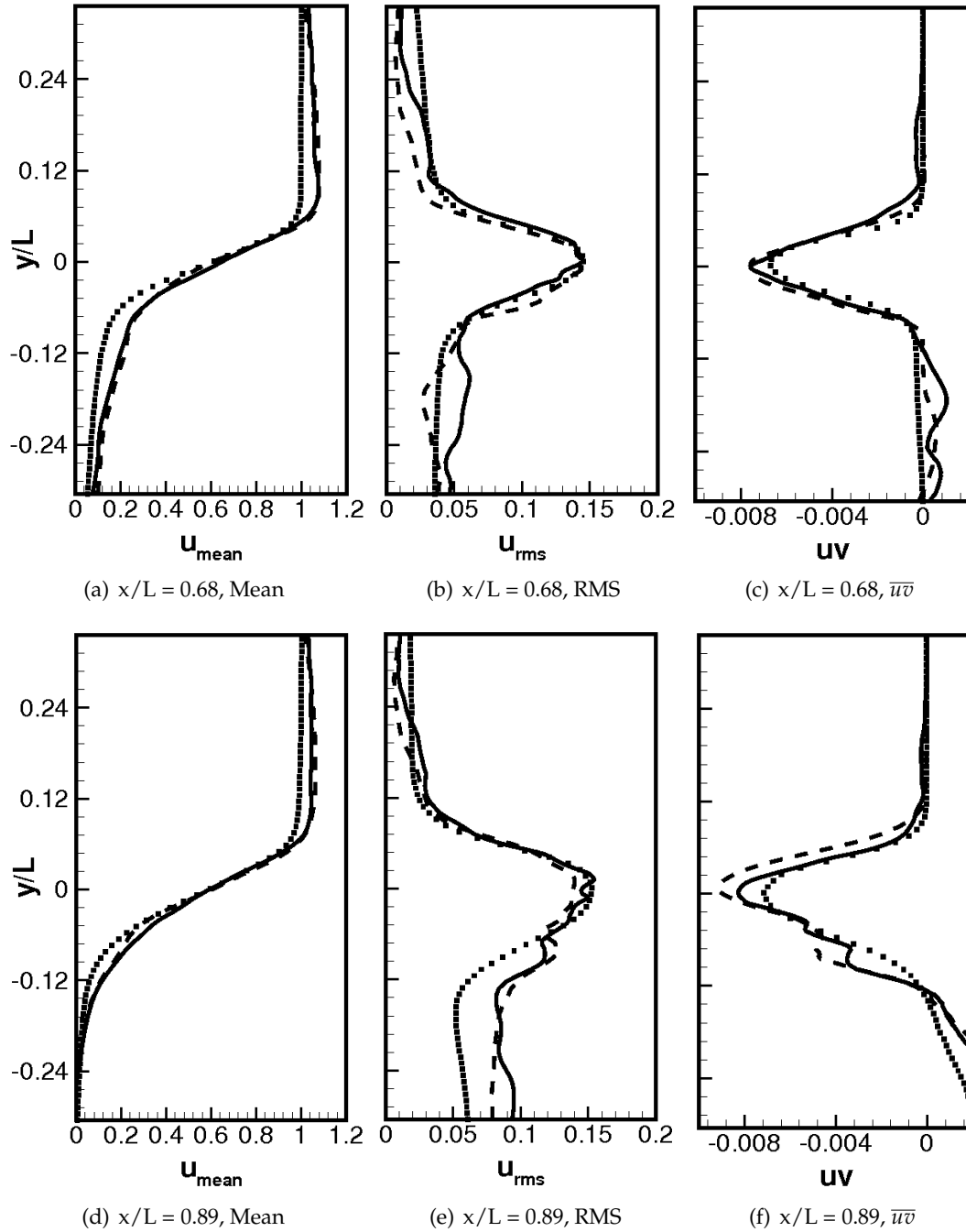


Figure 5.10: Comparison of vertical variations of mean ( $\overline{U}/U_\infty$ ) and rms ( $\sqrt{\overline{u^2}}/U_\infty$ ) of stream-wise velocity component and Reynolds Stress ( $\overline{uv}/U_\infty^2$ ), on the shear layer with (solid lines) and without (dashed lines) inflow fluctuations with the experiment data of LK2008 (symbols).

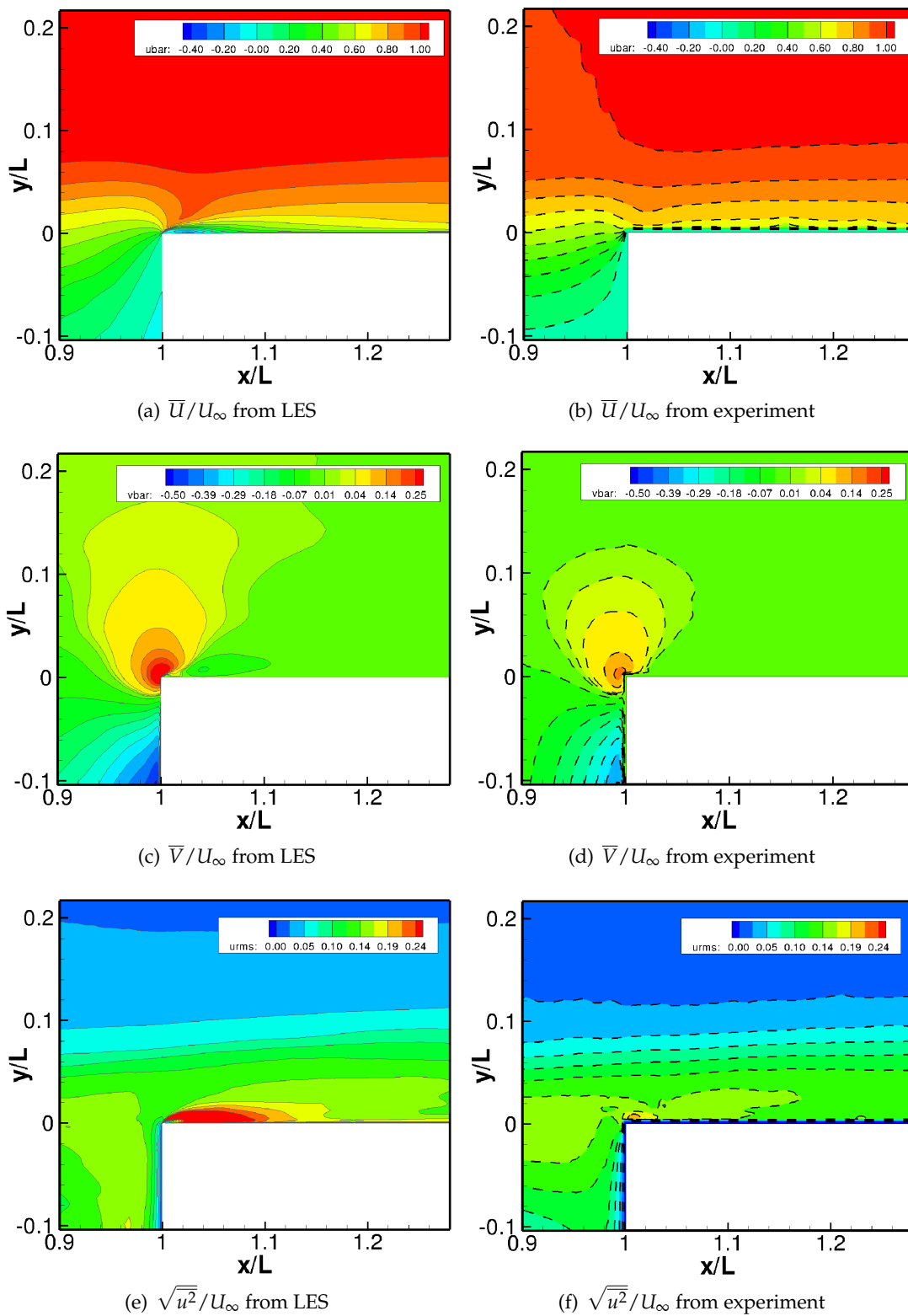


Figure 5.11: Cont'd on the next page.

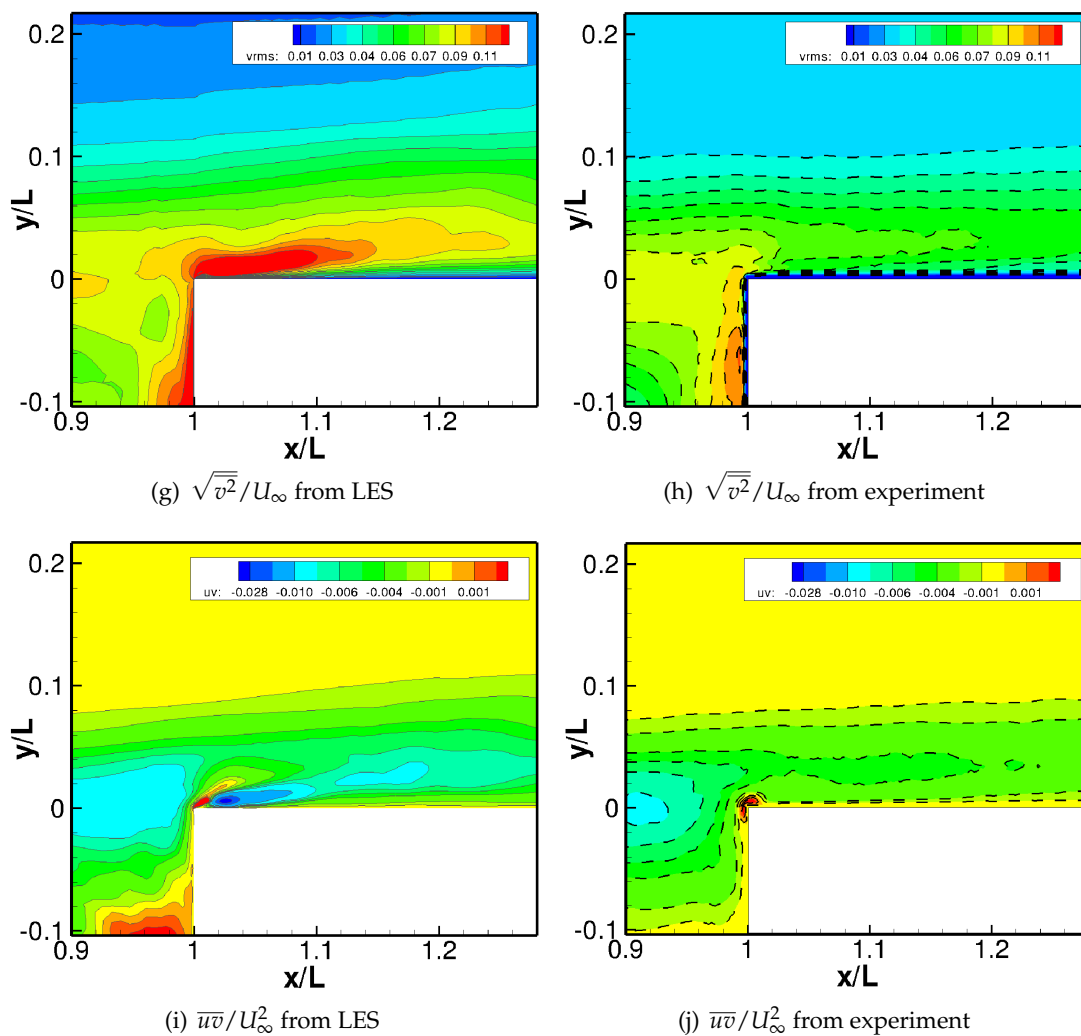


Figure 5.11: Contours of flow velocity statistics on the trailing edge, showing mean ( $\overline{U}/U_\infty$  and  $\overline{V}/U_\infty$ ), rms ( $\sqrt{\overline{u^2}}/U_\infty$  and  $\sqrt{\overline{v^2}}/U_\infty$ ), and Reynolds Stress ( $\overline{uv}/U_\infty^2$ ) from both LES (color contours), and experimental data (dashed contour lines) from LK2008.

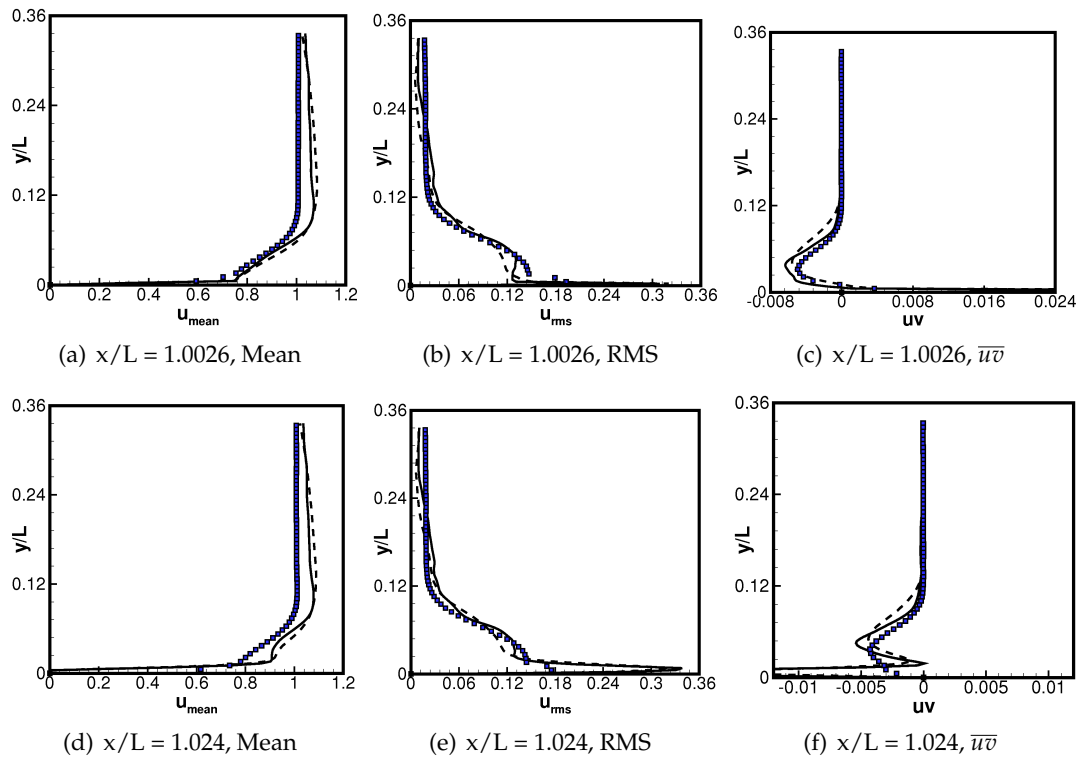


Figure 5.12: Distribution of flow velocity statistics on top of the shear layer with basic grid (solid line), coarse grid (dashed line), and experimental (symbols) results.

## 5.5 Pressure Distribution

Pressure is the most important parameter in the accuracy of both cavitation models used in this study. In the scalar transport model, it is used to determine the source and sink terms, indicating the generation and destruction of liquid vapor. Bubble cavitation model also uses pressure and its gradient for the calculations of bubble motion and size variation. Accordingly, accurate prediction of pressure is crucial in any numerical simulation of cavitation. In this section, statistics and instantaneous behavior of pressure are being investigated and analyzed for the LES of turbulent flow over cavity.

Figure 5.13 shows the distribution of mean and rms of pressure near the trailing edge, in comparison to available experimental data from LK2008. The following two features, which are also observed in the experiments, are accurately predicted: (i) a high-pressure region just upstream of the trailing edge (corner in the present 2D plane) which extends into the cavity, and (ii) a low pressure region above the trailing edge. The high pressure region just upstream of the trailing edge occurs basically due to the impingement of the shear layer onto to the trailing edge, creating a stagnation point slightly below the edge. The flow then has to turn and go around, creating a low pressure region above the trailing edge. The shape of contours of the mean  $C_p$  are similar to those observed in the experiments. The low pressure and high pressure regions are predicted very well in comparison to the experiment. The LES results show close agreement with the experiment especially away from the corner. However, absolute values of LES results near the corner are higher than the corresponding values obtained by LK2008 (figures 5.13(a) and 5.13(b)).

Figure 5.13(c) also shows the *rms* distribution of pressure near the trailing edge from LES results. It shows large amount of pressure fluctuation the the top of the corner, which is even larger than the mean value. This large pressure fluctuation is an essential factor in the cavitation inception at large cavitation indices (i.e.  $\sigma > (p_\infty - p_v)/0.5\rho U_0^2$ ).

In order to further analyze the pressure fluctuations in this geometry, PDF of pressure signals are studied at different locations. The distribution of the mean pressure near the trailing edge is shown in figure 5.14. Also shown are locations of eight probes (p1–p8) at which the pressure signal is further analyzed. The probability distribution functions (PDFs) of the fluctuations in pressure coefficient ( $C'_p$ ) at the eight probes are shown in figure 5.15a-h. The corresponding mean and *rms* values of  $C_p$  are also quoted.

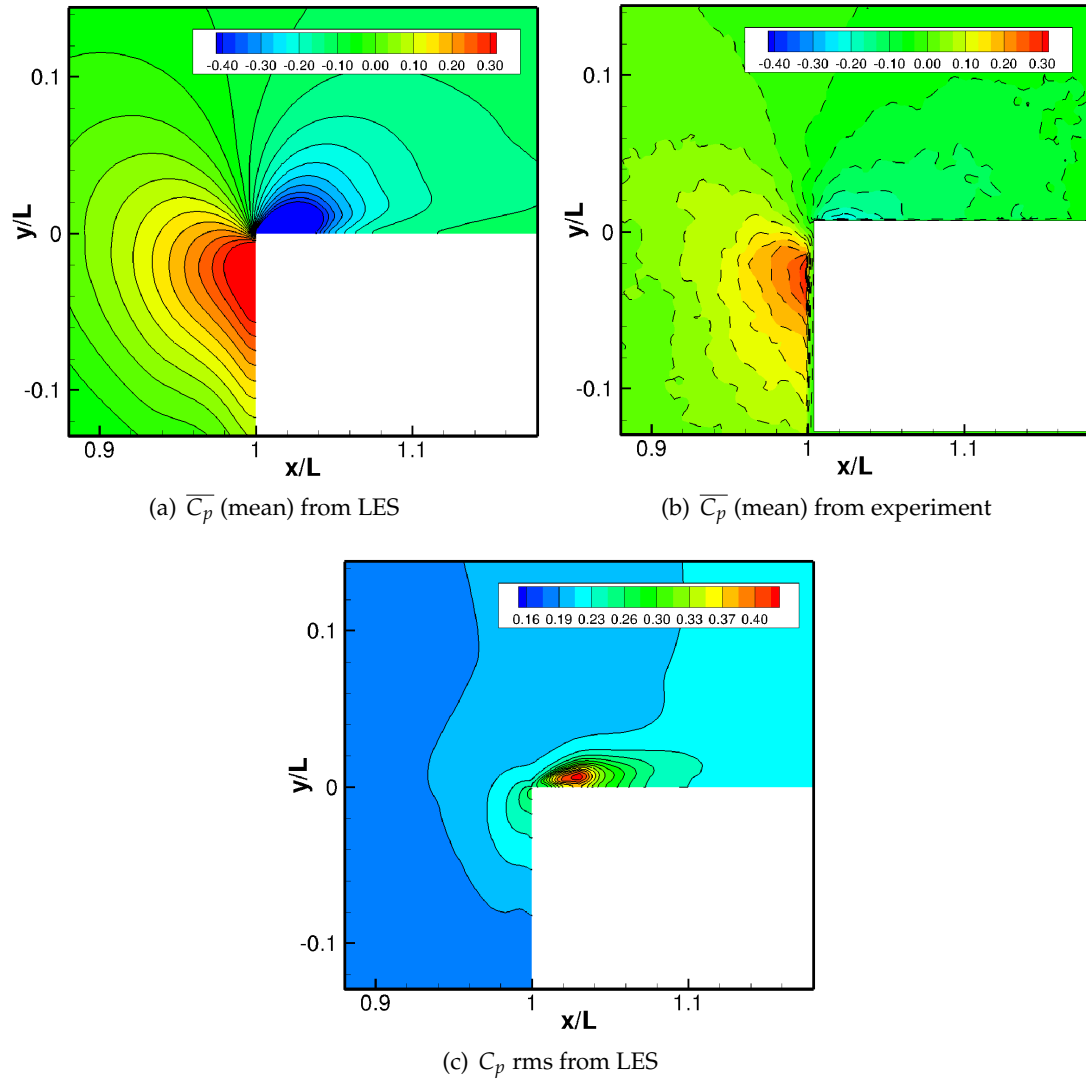


Figure 5.13: Contours of mean ( $\overline{C_p}$ ) and rms ( $\sqrt{C_p'^2}$ ) of pressure coefficient near the trailing edge. Shown is the LES results (color contours) and experimental results (dashed lines) from LK2008.

Probes p1 and p2 are slightly upstream of the trailing edge, probes p3 and p4 are in the shear layer, and probes p5–p8 are downstream of the trailing edge. Based on the mean values of  $C_p$  and PDFs of  $C'_p$ , cavitation is likely to occur inside the shear layer for a cavitation index of  $\sigma_i \leq \sim 0.43$  (for example, for probe p3,  $\bar{C}_p = -0.13$  with a PDF tail of around  $-0.3$ ). LK2008 also observed cavitation inside the shear layer for similar inception index. The mean statistics were collected over 4 flow through times (that is over around 33 ms where one flow through time is taken to be approximately  $L/U_\infty \sim 7.7$  ms. This is rendered sufficient time for the shear-layer statistics.

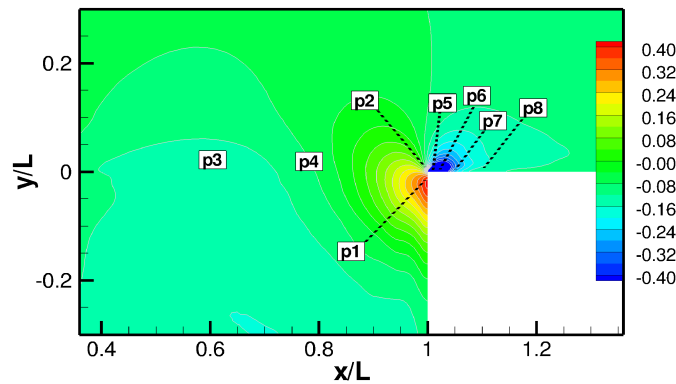


Figure 5.14: Time-averaged contours of pressure coefficient ( $\bar{C}_p$ ) near the trailing edge.

The probes (p5–p8) above the trailing edge (downstream of the corner) show low values of  $\bar{C}_p$  together with a broader spectrum of  $C'_p$ . Inception first occurs inside these regions as also noted by LK2008. It is observed that in the present simulations, the absolute values of mean pressure coefficient ( $|\bar{C}_p|$ ) at some points above the trailing edge (i.e. probes p5–p8) were generally higher and the *rms* values ( $C_{p,rms}$ ) were lower compared to the experimental data. For example, at probe p6,  $\bar{C}_p = -0.63$  and  $C_{p,rms} = 0.3$  providing an inception index of  $\sigma_i = 0.93$ . LK2008 also reported inception index of  $\sigma_i = 0.9$ ; however, generally showed lower mean  $|\bar{C}_p|$  and higher  $C'_p$  above the trailing edge.

In LES, the PDFs of  $C'_p$  showed larger negative tails. If instantaneous values of  $C_p$  are used as criterion for inception, these distributions indicate that inception above the trailing may occur at even higher  $\sigma$  values. In experiments, the pressure signal was deduced based on the material acceleration  $D\mathbf{u}/Dt$  by neglecting the viscous effects (Liu and Katz, 2006). In LES, near the trailing edge, the viscous effects may be small; how-

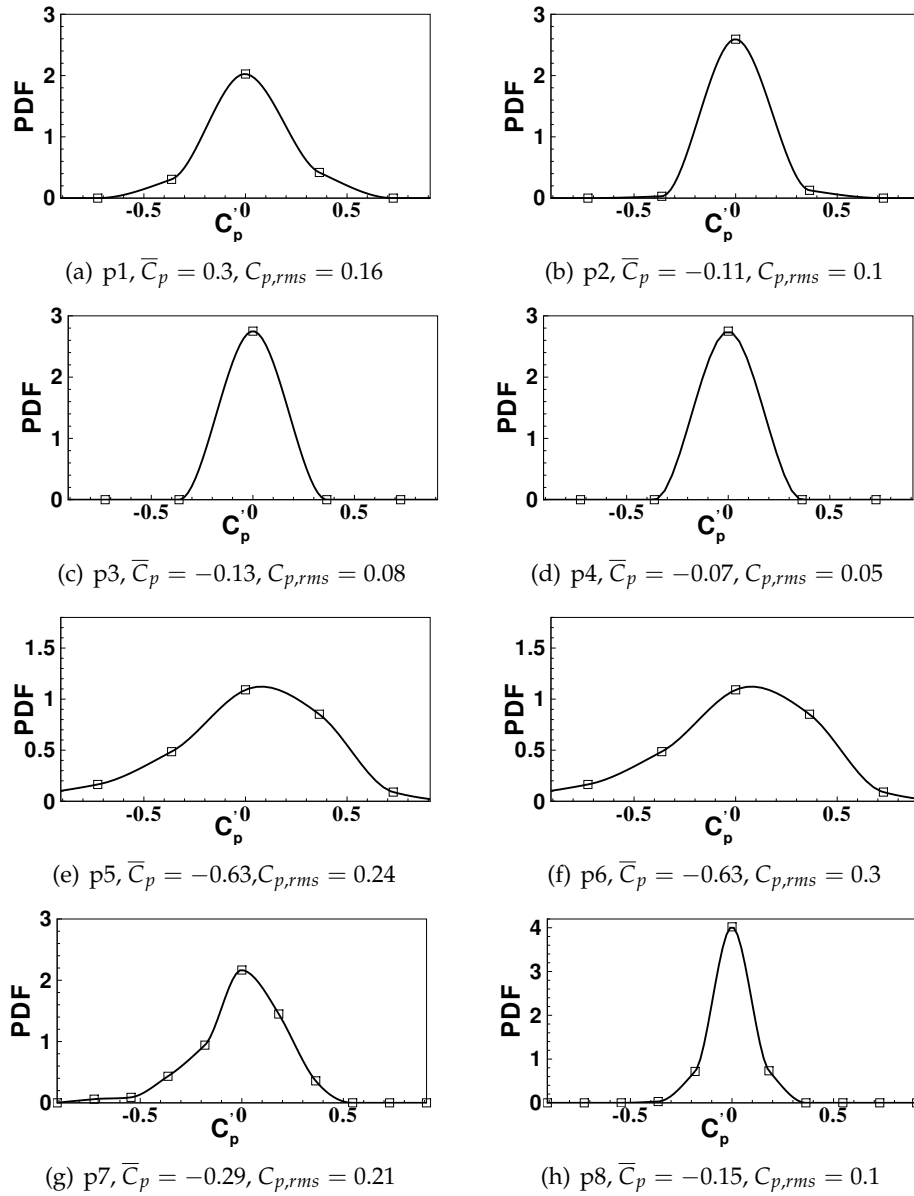


Figure 5.15: Probability distribution functions for  $C'_p$  at the eight probe locations (p1–p8) shown in Figure 5.14.

ever, the subgrid-scale stresses can be large influencing the filtered pressure field as:

$$-\frac{1}{\rho_\ell} \nabla \bar{P} = \frac{D\bar{\mathbf{u}}}{Dt} - \frac{\partial \tau_{ij}^r}{\partial x_j}. \quad (5.2)$$

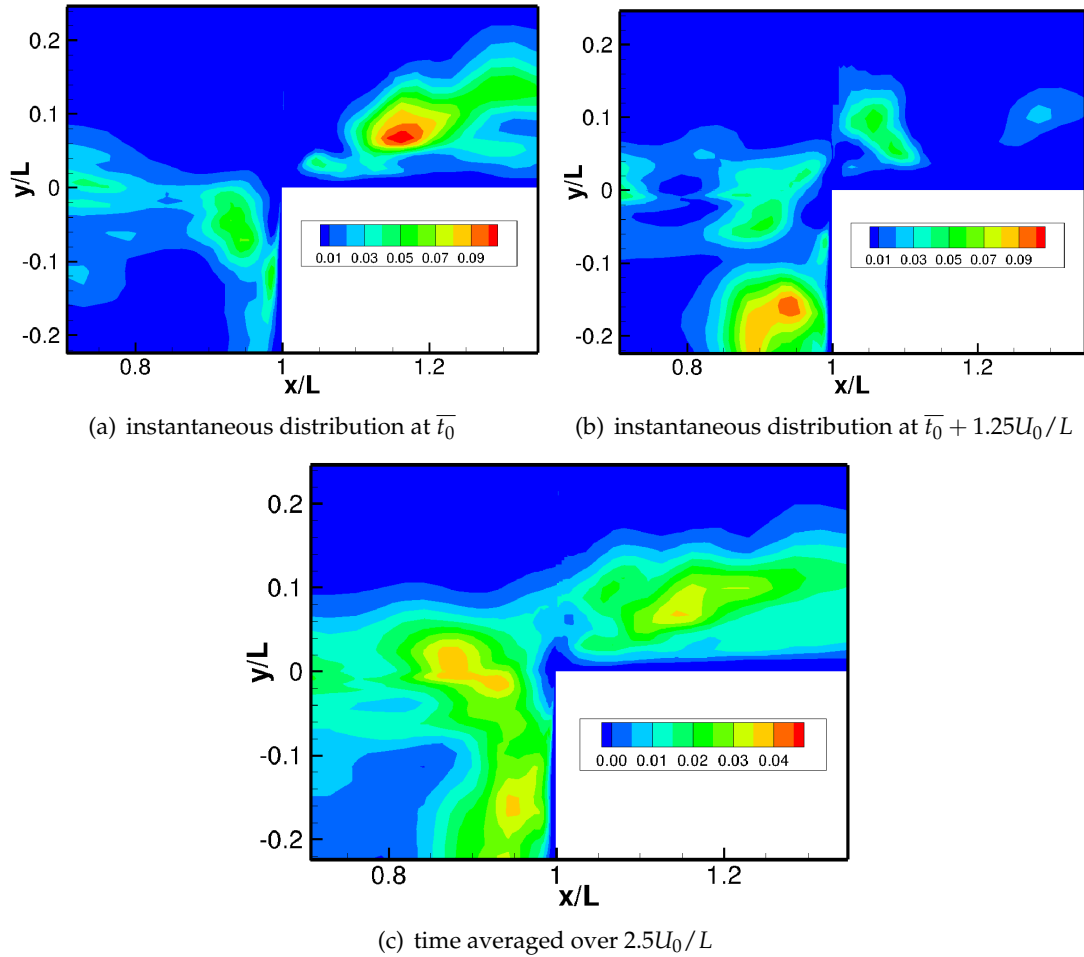


Figure 5.16: Eddy viscosity  $\mu_T$  calculated by subgrid scale model

Figure 5.16 shows the distribution of eddy viscosity on top of the trailing edge and on the shear layer. It shows large values of  $\mu_T$  near the corner. The maximum average values are shown in figure 5.16(c) fairly correspond to the regions where the absolute value of pressure is predicted different from those calculated in the experiment. It is

conjectured that local variations in subgrid-scale stresses and subgrid viscosity obtained from the dynamic model may affect the filtered pressure field resulting in lower pressure values in a small region above the trailing edge. However, away from the trailing edge, the pressure coefficients were well predicted compared to the experiments. The variations in  $C_p$  values above the trailing edge were related to the impacting of shear layer vortices on the trailing edge and is discussed below.

## 5.6 Instantaneous Flow Field

Figure 5.17 shows the instantaneous plots of  $C_p = (\bar{P} - P_\infty)/(0.5\rho U_\infty^2)$  in the symmetry plane ( $z = 0$ ) together with instantaneous streamlines obtained by removing  $0.5U_\infty$  from the axial velocity field. Low pressure regions within the shear layer and corresponding vortical structures are clearly visible. The two snapshots (5.17a,b) correspond to higher and lower pressures just above the trailing edge corner ( $x/L = 1.01$ ,  $y/L = 0.0035$ ,  $z/L = 0$ ). The instantaneous  $C_p$  signal at this location is also shown in figure 5.17d. The vortical structures in the shear layer generated from the leading edge separation travel downstream and interact with the trailing edge causing significant changes in the  $C_p$  values above the trailing edge. Liu and Katz (2008) showed similar vortex structures and argued that there is a strong correlation between the traveling vortices and the trailing edge, causing flow-induced  $C_p$  fluctuations. Similar interactions between the traveling vortices and the trailing edge are observed. Based on the signal shown in figure 5.17d, the  $C_p$  value varies over a wide range of  $-0.01$  to  $-2$ . The  $C_p$  values also showed variations in the spanwise directions suggesting that the impact location of the vortex cores on the trailing edge (and the stagnation point) move in and out of the plane (in spanwise directions). Based on the mean and *rms* values of the pressure coefficient at neighboring points ( $\bar{C}_p \sim -0.639$ ,  $C_{p,rms} \sim 0.29$ ), the inception index is approximately  $\sigma_i \sim 0.93$ .

## 5.7 Cavitation Inception

We consider two different approaches to investigate the nature of cavitation near the trailing edge and inside the shear layers: (i) a discrete bubble model and (ii) a scalar transport model. In the discrete bubble model, it is assumed that water contains abun-

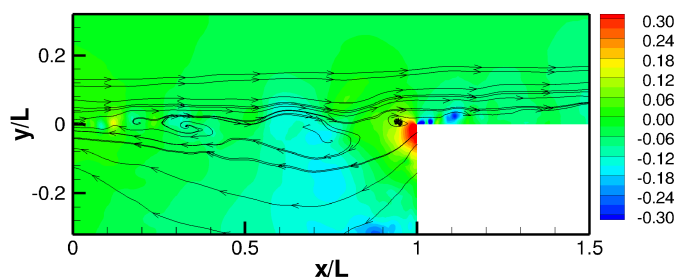
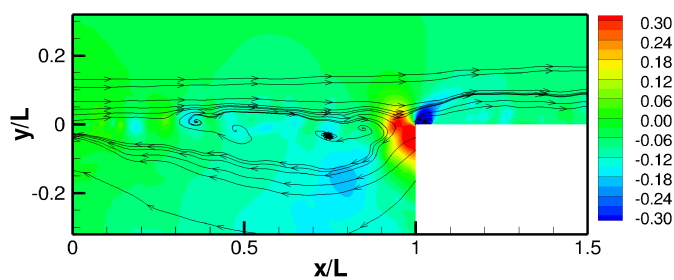
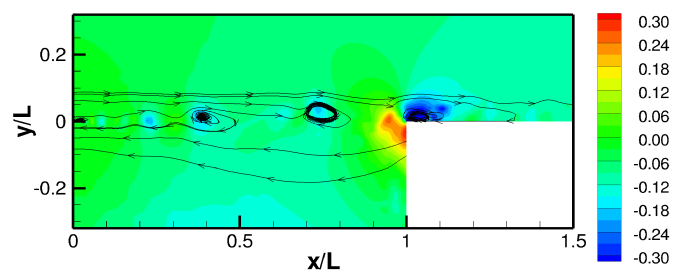
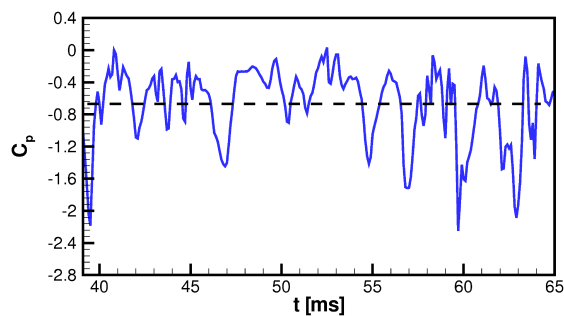
(a)  $t = 53$  ms(b)  $t = 55$  ms(c)  $t = 65$  ms(d)  $C_p(t)$ 

Figure 5.17: Instantaneous pressure contours and stream traces (based on removing  $0.5U_\infty$  from the streamwise velocity):(a)  $t = 53$  ms (high pressure above the trailing edge), (b)  $t = 55$  ms (low pressure above the trailing edge), (c)  $t = 65$  ms, (d)  $C_p(t)$  at a probe above the trailing edge ( $x/L = 1.01$ ,  $y/L = 0.0035$ ,  $z/L = 0$ ).

dant nuclei of dissolved gas which can undergo rapid size variations indicating occurrence of cavitation. In the scalar transport model, actual phase change is simulated by modeling rates of evaporation and condensation based on the local pressure field compared to the vapor pressure. Results obtained from both models are presented below.

### 5.7.1 Scalar Transport Model

In this model, a transport equation for liquid volume fraction is solved:

$$\frac{\partial \Theta_\ell}{\partial t} + \nabla \cdot (\Theta_\ell \vec{u}) = \dot{m}^+ + \dot{m}^-, \quad (5.3)$$

where the source terms  $\dot{m}^-$  and  $\dot{m}^+$  represent the destruction (evaporation) and production (condensation) of the liquid. They are both functions of the local and vapor pressures:

$$\dot{m}^- = \frac{C_{dest} \rho_\ell \min(P_\ell - P_v, 0) \Theta_\ell}{\rho_v (0.5 \rho_L U_\infty^2) t_\infty} \quad (5.4)$$

$$\dot{m}^+ = \frac{C_{prod} \max(P_\ell - P_v, 0) (1 - \Theta_\ell)}{(0.5 \rho_\ell U_\infty^2) t_\infty}, \quad (5.5)$$

where  $C_{dest}$  and  $C_{prod}$  represent the empirical constants and  $t_\infty$  is the characteristic time-scale associated with the flow. In this work,  $C_{dest}$  and  $C_{prod}$  are set to 1.0 and 80, respectively, based on similar values used by Senocak and Shyy (2002a). The time scale is set equal to the flow-through time based on the cavity length ( $L$ ) and the mean flow velocity in the duct ( $U_\infty$ ).

The source and sink terms in the transport equation are proportional to the difference between the local pressure and the vapor pressure as well as the amount of liquid present in a given control volume. Typically, if the local pressure drops below the vapor pressure, the liquid evaporates creating vapor. In the present work, the local pressure field was defined relative to the pressure field above the leading edge of the cavity ( $P_\infty$ ). Similarly to the experiments, the absolute value of  $P_\infty$  was reduced starting with one atmosphere. The vapor pressure was assumed to be  $P_v = 2.337$  kPa.

Early sites of cavitation observed above the trailing edge where the pressure minima occurs. Small amounts of vapor were created in this region with vapor fractions on the

order of 0.01 for a cavitation index of  $\sigma_i = 0.9$  (not shown here). Figure 5.18 shows time

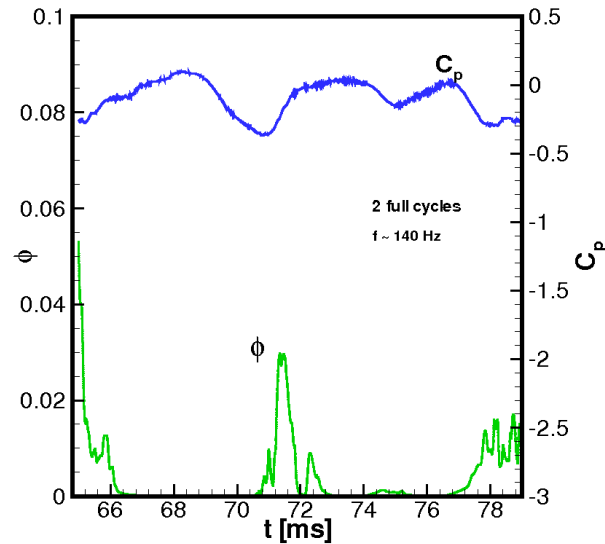


Figure 5.18: Time evolution of vapor fraction and  $C_p$  just above the trailing edge at  $\bar{\mathbf{x}} = (38.0, 0.3, 0.0)$  for  $\sigma_i = 0.9$ .

variation of vapor fraction  $\phi$  and coefficient of pressure  $C_p$  just above the trailing edge for  $\sigma_i = 0.9$ . The inception frequency for this cavitation index is almost 140 Hz.

Further reduction in  $P_\infty$  resulted in increased inception frequency and amount of cavitation above the trailing edge. Temporal evolution of vapor fraction on top of the trailing edge is shown in figure 5.19 for  $\sigma_i = 0.4$ . In the experiments, vigorous cavitation was observed at this level. Periodic occurrence and disappearance of vapor fraction structures above the trailing edge are clearly visible (dark regions show large vapor fraction). A time trace of instantaneous  $\phi$  and  $C_p$  are plotted in figure 5.20. The frequency of the growth and decay of vapor fraction is observed to be around 300 Hz for the present case with  $U_\infty = 5$  m/s. As can be seen from the contour plots and the time traces, periodic occurrence and disappearance of cavitation is predicted similar to that observed in experiments. This indicates that this periodic cavitation phenomenon is associated with the pressure variations above the trailing edge. The pressure variations are mainly caused by the shear-layer eddies impinging on the the cavity trailing edge (see figures 5.17). Since the focus of interest in this study is cavitation inception not the

dynamic effects on the flow, pressure, velocity, and density are not coupled. Coupling these quantities may become important when heavy cavitation occurs (for the case of  $\sigma_i \leq 0.4$ ). However, the features associated with periodic growth and decay of the vapor fraction above the trailing edge are captured.

Cavitation index in the scalar transport studies was decreased even further down to  $\sigma_i = 0.1$ . This study shows cavitation also occurs on the shear layer above the cavity. Figure 5.21 shows time evolution of vapor fraction on the shear layer and inside the cavity. The amount of vapor on the shear layer is mainly generated due to pressure being lower than vapor pressure or  $Cp < \sigma_i = 0.1$ . PDF of pressure fluctuations on the shear layer (Figure 5.15c-d), also indicates that the pressure drops below  $\sigma_i = 0.1$ . This has been observed in the experiments with  $\sigma_i < 0.4$ , as reported by Liu and Katz (2008).

### 5.7.2 Discrete Bubble Model

Cavitation inception studies are also performed by using the discrete bubble model (DBM) with adaptive time-stepping as described in chapter 2. The gas content in the liquid was assumed to be small (initial gas void fraction was assumed to be  $10^{-5}$ ). It is important for the bubble nuclei to pass through the small pressure regions above the cavity ('window of opportunity' to get drawn into low pressure regions and cavitate) (Hsiao et al., 2006). Accordingly, air nuclei were distributed evenly in a small band around the shear layer. The bubbles were initially injected over a small region in stream-wise direction and in a band of 10 mm in the mid section of flow span. In order to keep the number of bubbles constant in the domain, bubbles were continuously injected near the leading edge and removed farther away from the trailing edge. To analyze the sensitivity of the initial bubble size to cavitation inception, detailed PDF analysis (following the works of Cerutti et al. (2000) and Kim et al. (2006)) was performed by collecting data over 1.8 flow through time based on the cavity length and the free-stream velocity.

Figure 5.22 shows the temporal evolution of bubble locations inside the shear layer and above the trailing edge. The size of the scatter symbols is scaled with respect to the size of the bubble. Accordingly, large size bubbles are obtained near the trailing edge. The initial pressure inside the bubble was set based on an equilibrium radius corresponding to the radius of the nuclei and its location in the domain. Using the Rayleigh-

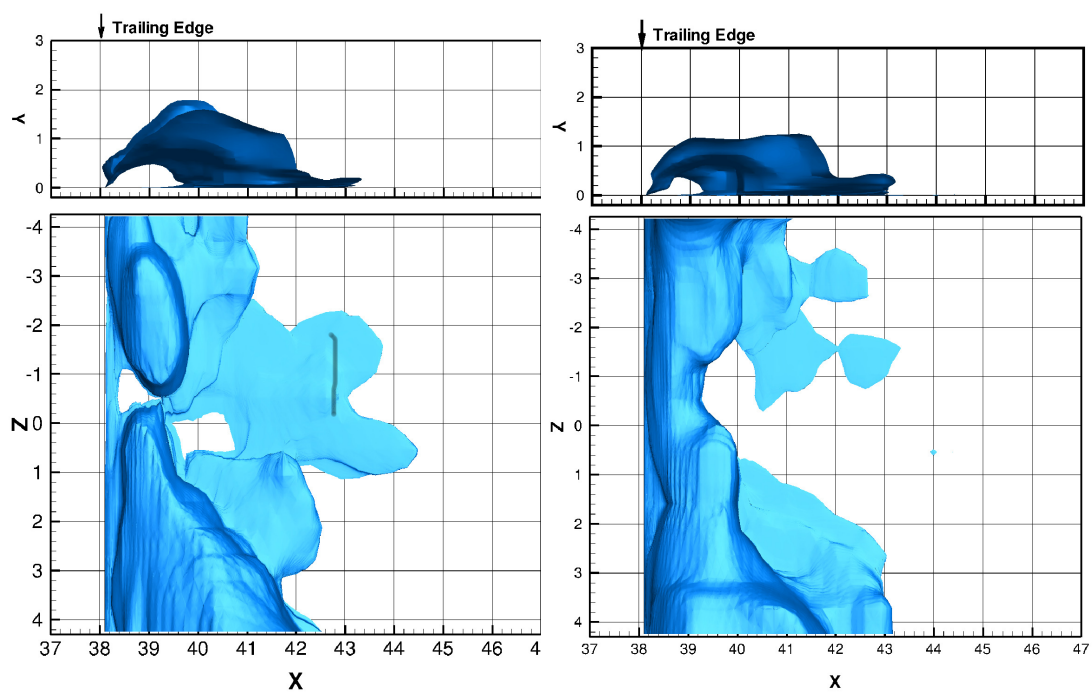
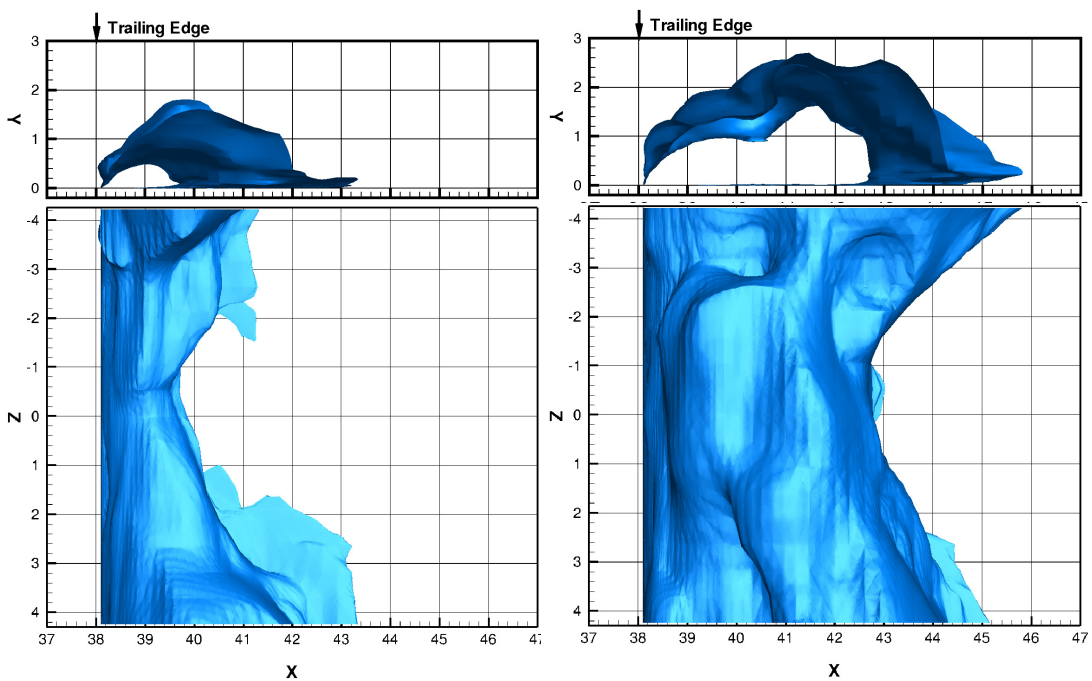
(a)  $t = 52.7$  ms(b)  $t = 53.4$  ms(c)  $t = 53.6$  ms(d)  $t = 54.4$  ms

Figure 5.19: Cont'd on the next page.

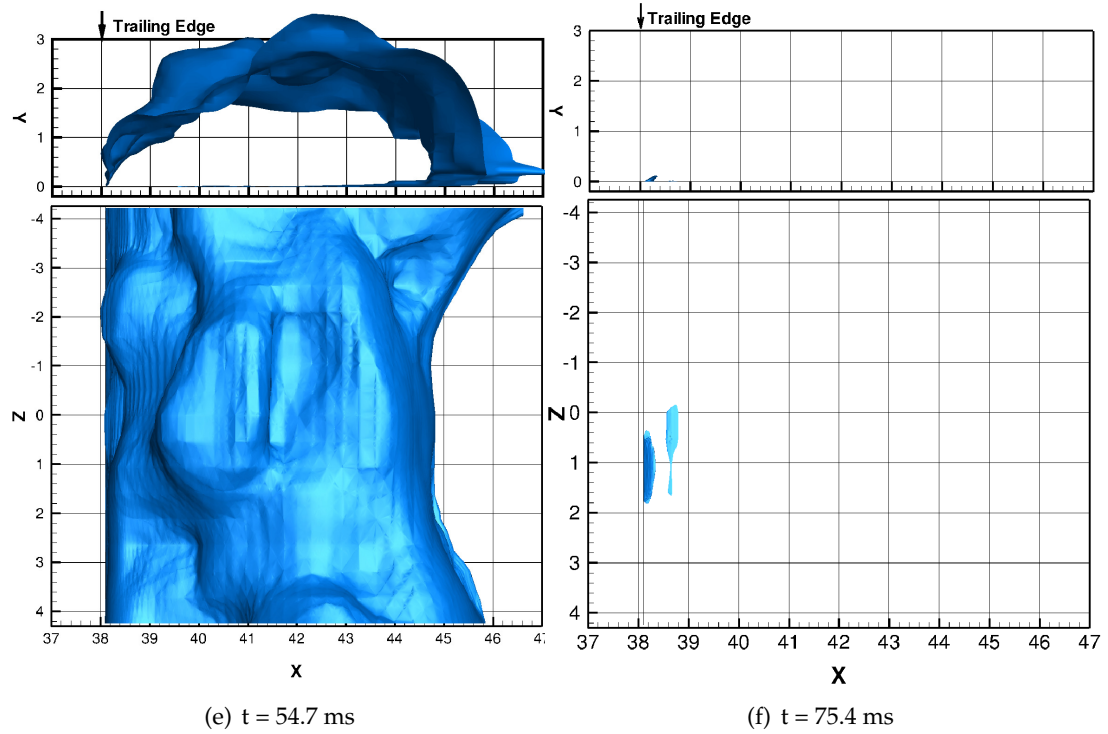


Figure 5.19: Evolution of vapor fraction ( $\phi = 1 - \Theta_\ell = 0.2$ ) above the trailing edge as predicted by the scalar transport model. Periodic growth and decay of the local vapor fraction is correlated with the variations in  $C_p$  just above the trailing edge.

Table 5.4: Case studies to analyze cavitation inception using the Discrete Bubble Model.

Case	Figure Symbol	$d_{\text{initial}}$ ( $\mu\text{m}$ )	$\sigma_i$
C1	square	10	0.4
C2	triangle	50	0.4
C3	circle	100	0.4
C4	diamond	50	0.9
C5	circle (filled)	50	1.4
C6	square (filled)	50	0.1

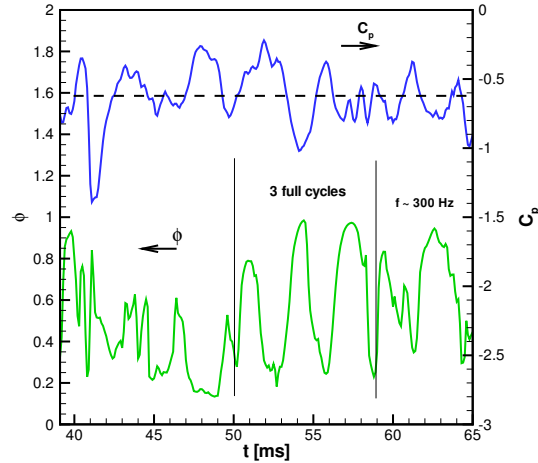


Figure 5.20: Time evolution of vapor fraction and  $C_p$  just above the trailing edge at  $\bar{x} = (38.1, 0.01, 0.0)$  for  $\sigma_i = 0.4$ .

Plesset equations (2.9), at equilibrium conditions, the pressure inside the bubble can be obtained as:  $P_b = \bar{P}_{out} + 2\sigma/R_b$  ( $\sigma$  is the surface tension coefficient). The bubbles are then advected using the adaptive time-stepping described earlier with ‘one-way’ coupling (bubbles do not affect the flow). On an average, approximately 50,000 bubble trajectories are tracked at each instant. In order to gain better understanding of how different parameters such as the initial bubble size and cavitation index  $\sigma_i$  affect the inception and the behavior of bubbles, three different initial bubble sizes (10, 50, and 100  $\mu\text{m}$ ) were considered with a constant cavitation index ( $\sigma_i = 0.4$ ). In addition, four different cavitation indices (0.1, 0.4, 0.9, and 1.4) were examined on a certain initial bubble diameter ( $d_{init} = 50 \mu\text{m}$ ). Table 5.4 shows different diameters and cavitation indices used in the present study.

Figure 5.23 shows instantaneous snapshots (a top view) of bubbles just in the the shear layer and above the trailing edge (only a few bubbles are shown for clarity). The bubble size is scaled according to their diameter; thus bubbles with large radius appear more prominently. The two sets of snapshots correspond to different values of  $P_\infty$  (set based on the cavitation index ( $\sigma_i$ ) of 0.4 and 0.9). For  $\sigma_i = 0.4$  large size bubbles are readily observed near the trailing edge. As shown later, rapid variation in bubble size

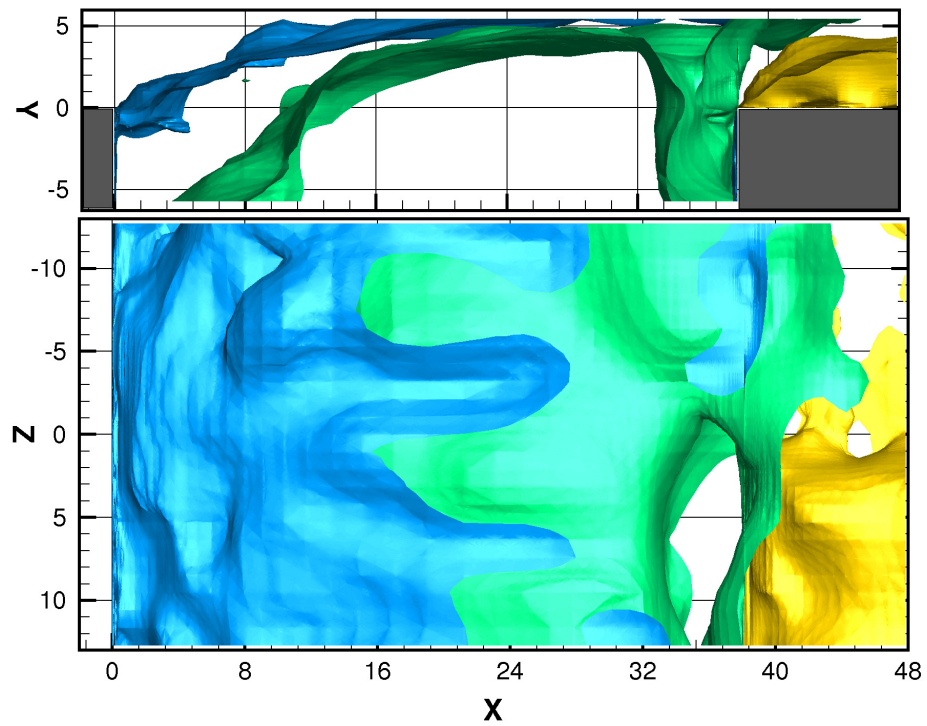
(a)  $t = 66.2$  ms

Figure 5.21: Time evolution of liquid vapor fraction ( $\phi = 1 - \Theta_\ell$ ) on the shear layer with  $\sigma_i = 0.1$  from the scalar transport model. Shown in the figure are iso-surfaces of  $\phi = 0.2$  (cyan),  $0.4$  (light green), and  $0.8$  (yellow).

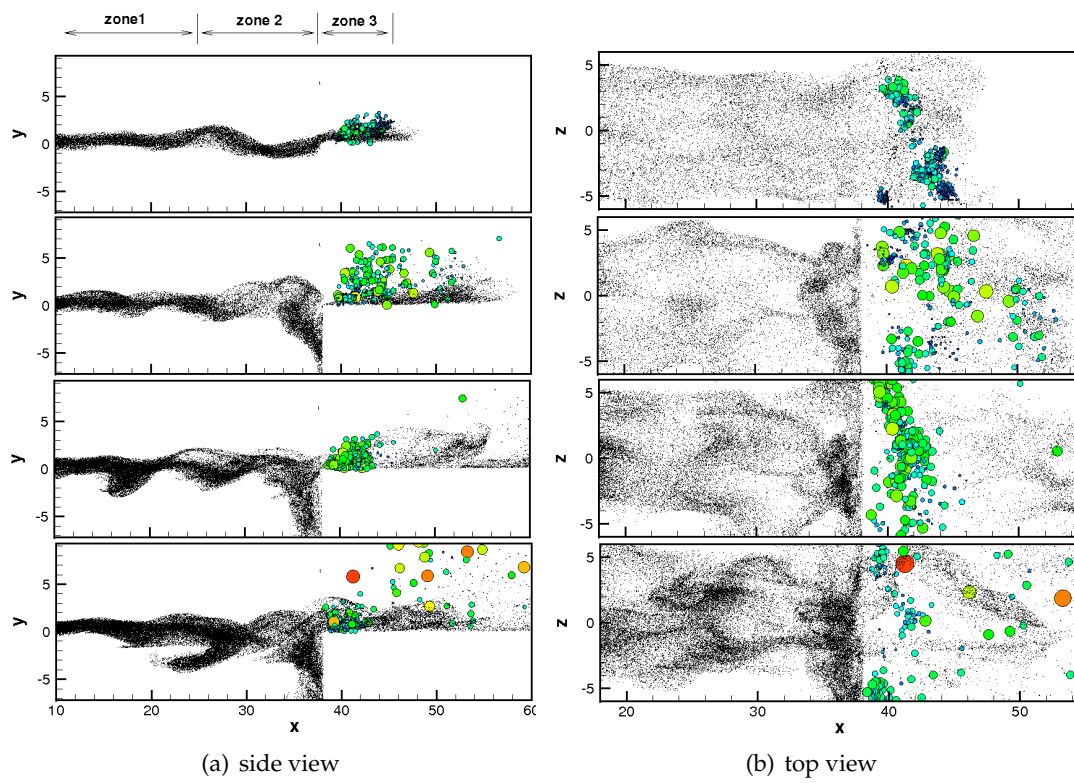


Figure 5.22: Temporal evolution of bubble distribution (initial size  $50 \mu\text{m}$ ) on the shear layer (side view) for  $\sigma_i = 0.4$ .

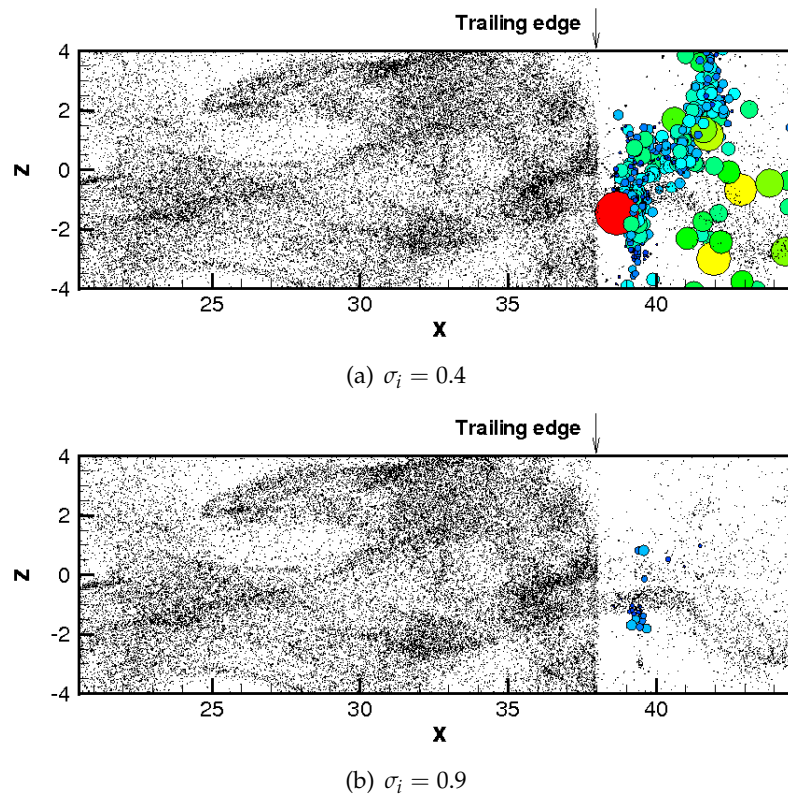


Figure 5.23: Top view of the instantaneous snapshot of bubbles above in the shear layer and near the trailing edge: (a) absolute value of outside pressure based on  $\sigma_i = 0.4$ , (b) outside pressure based on  $\sigma_i = 0.9$ .

occurs near the trailing edge. As shown later, for this inception index, bubbles inside the shear layer also showed growth in their size. For higher pressure at the upstream ( $\sigma_i = 0.9$ ; figure 5.23b), bubbles cavitate near the trailing edge; however, little change in size of the bubbles was observed inside the shear layers.

### 5.7.3 Bubble Trajectories

Sample trajectories of bubbles on the shear layer are monitored. Figure 5.24 shows the variations in the outside pressure signal ( $C_p$ ) and the corresponding changes in the bubble radius ( $R_b$ ) experienced by the bubble as it moves from its injection location. Two sample bubble trajectories are shown for bubbles released close to the leading edge in the wall-normal direction. The first trajectory (figure 5.24a) is for outside pressure set based on the cavitation index of 0.8. The bubbles show rapid variations in their size as they encounter the trailing edge low pressure region. The second trajectory (figure 5.24b) corresponds to bubble dynamics with a much lower upstream pressure ( $\sigma_i = 0.1$ ). This shows cavitation occurring on the shear layer for this low cavitation index.

### 5.7.4 Data Sampling

To analyze the effect of various model parameters, probability distribution functions (PDFs) of number of bubbles were collected based on their growth ratio  $d/d_{\text{initial}}$ , the pressure coefficient  $C_p$ , and the vorticity  $\omega$  at bubble position. Three different initial bubble sizes were considered (cases C1, C2, C3), and for initial bubbles of 50  $\mu\text{m}$  the cavitation index was varied ( $\sigma_i = 0.4, 0.9, 1.4$ , and 0.1) in cases C2, C4, C5, and C6.

Two different data sampling criteria are used in the following PDF calculations: (i) sampling based on bubble location in domain, and (ii) sampling based on the bubble growth rate. Sampling regions are labeled as zone 1, 2, and 3 in figure 5.22. The criteria for the location are  $-5\text{mm} < y < 5\text{mm}$  in three different zones in stream-wise direction:  $-2\text{mm} < x < 25\text{mm}$ ,  $25\text{mm} < x < 38\text{mm}$ , and  $38\text{mm} < x < 45\text{mm}$ , which are being referred to as zone 1, 2, and 3. We have also performed conditional sampling on the parameters based on bubble growth ratio ( $d/d_{\text{initial}}$ ), and location. For the growth ratio condition three different zones of  $d/d_{\text{initial}} < 0.8$ ,  $0.8 < d/d_{\text{initial}} < 1.25$ , and

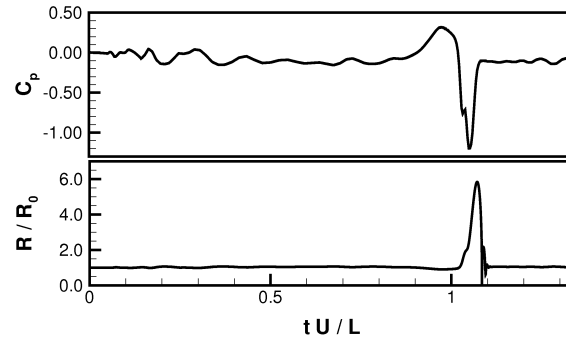
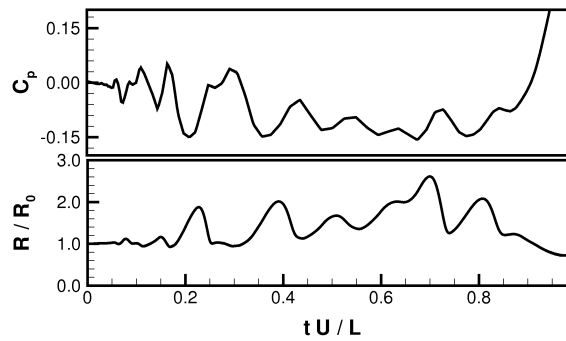
(a)  $y = 0.2 \text{ mm}, \sigma_i = 0.8$ (b)  $y = 0.1 \text{ mm}, \sigma_i = 0.1$ 

Figure 5.24: Temporal evolution of bubble radius (normalized by initial radius) and outside pressure coefficient ( $C_p$ ) seen by the bubbles for two sample trajectories of bubbles released near the leading edge. The upstream pressure level is set based on  $\sigma_i = 0.8$  for the top panel and  $\sigma_i = 0.1$  for the bottom panel: (a) bubble released at  $y = 0.2 \text{ mm}$ , (b) released at  $y = 0.1 \text{ mm}$  from the leading edge surface.

$1.25 < d/d_{\text{initial}}$ , referred to as small, medium, and large, are defined.

For the PDF calculations, data span of each parameter (minimum to maximum) has been divided into 41 different bins which are distributed logarithmically for diameter and linearly for pressure and vorticity. Data bins are logarithmically distributed for growth rate, and linearly distributed for coefficient of pressure and vorticity. Samples collected over several instantaneous snapshots were averaged and these results are discussed below.

### 5.7.5 Effect of Cavitation Index

Figure 5.25 shows the effect of cavitation index on the PDFs and number of bubbles sampled based on the bubble growth ratio ( $d/d_{\text{initial}}$ ) and the pressure at the bubble location in various regions of the shear layer and the trailing edge.

These plots are obtained with fixed initial bubble size of 50  $\mu\text{m}$ . In figure 5.25(a) we can observe that a majority of the bubbles retain their original size and are mostly insensitive to pressure variations ( $d/d_{\text{initial}} \sim 1$ ). With lower cavitation index ( $\sigma_i = 0.1$ ), the maximum bubble growth ratio is higher, and a small number of very large bubbles are observed near the trailing edge (giving rise to cavities on the order of 0.1-0.5 cm). This is due to the effect of lower pressure on the bubbles compared to the cases with  $\sigma_i = 0.9$  and 1.4. The other important difference is on the left tail of PDF (collapse region) where the PDF of growth ratio is almost an order of magnitude larger for  $\sigma_i = 0.9$  compared to  $\sigma_i = 0.4$ . This again indicates violent cavitation for lower cavitation index.

The behavior of bubbles in different regions of the flow, including near the leading edge (zone 1), in the mid-section (zone 2) and over the trailing edge (zone 3), is considered. Figures 5.25c-h show average number of bubbles sampled based on the growth ratio and  $C_p$  values. In zones 1 and 2 (i.e. inside the shear layer figures 5.25(c), and 5.25(e)), there is small change in the average number of bubbles versus a certain growth ratio for different cavitation indices; however, for  $\sigma_i = 0.1$  and 0.4 more variation in bubble sizes were observed in both zones (figures 5.25(c), 5.25(e)). Near the trailing edge, large differences in the number of bubbles with the same growth ratio are observed (figure 5.25(g)). For the lowest  $\sigma_i$  (C6), number of large bubbles observed near the trailing edge is at least an order of magnitude more than other cases (C2, C4, and

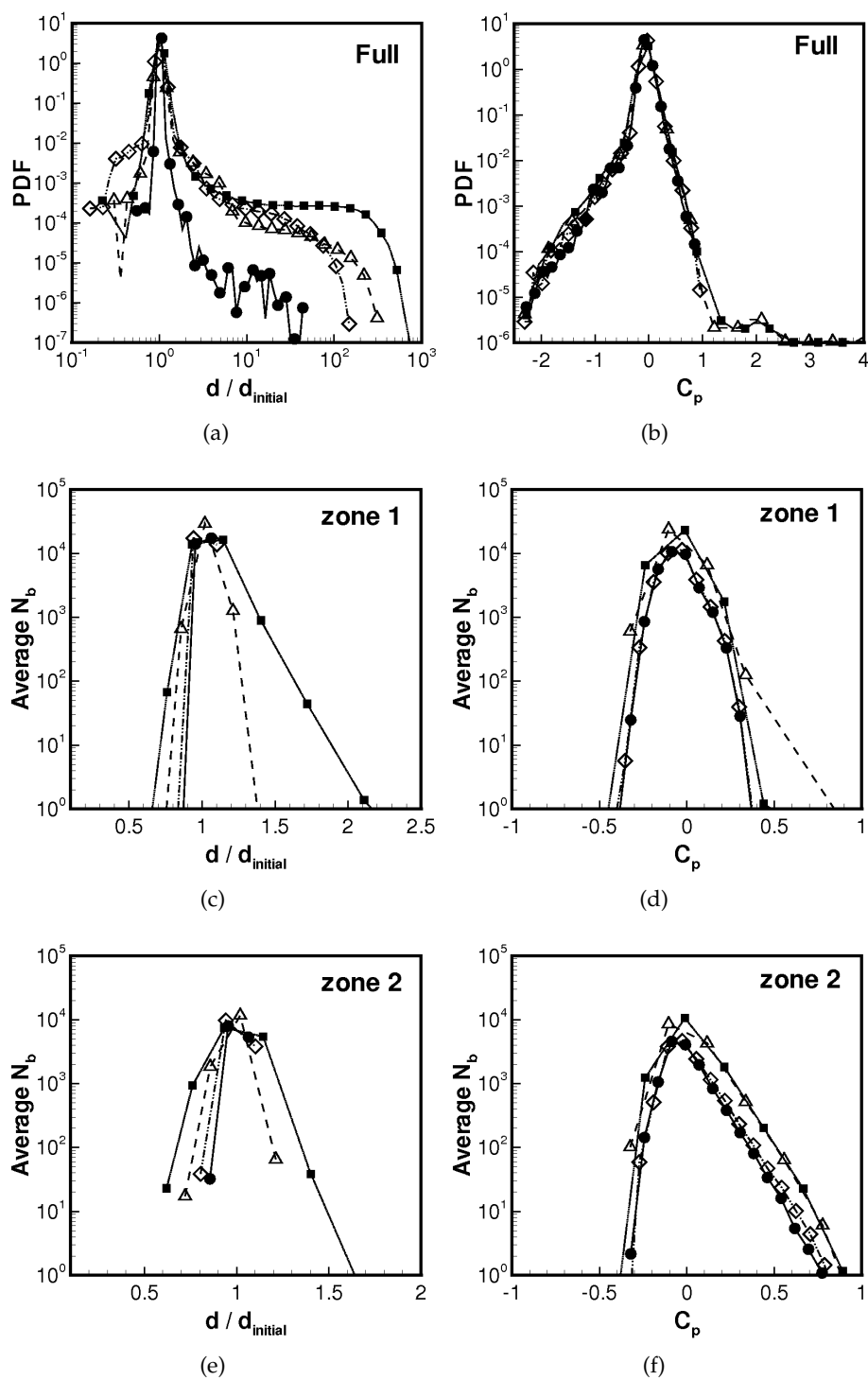


Figure 5.25: Cont'd on next page.

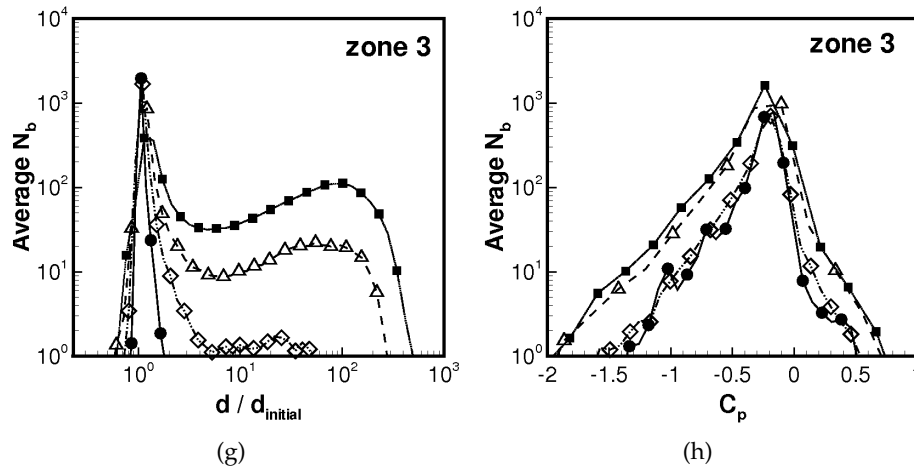


Figure 5.25: Effect of cavitation index  $\sigma_i$  on the PDFs and average number of bubbles ( $N_b$ ) sampled based on the growth ratio ( $d/d_{initial}$ ) and pressure coefficient  $C_p$  for case C2 (triangle symbols), C4 (diamond symbols), C5 (filled circles), and C6 (filled square): (a,b) PDF of all bubbles over the region of interest; (c,d) bubbles in zone 1; (e,f) bubbles in zone 2, and (g,h) bubbles in zone 3.

C5). The highest cavitation index nearly shows no cavitation above trailing edge.

Figure 5.25(b) shows the PDF of  $C_p$  at bubble locations for cases C2, C4, C5, and C6 over the entire region of interest. Changing  $\sigma_i$  doesn't change the PDF curves sampled based on  $C_p$  appreciably; implying that the location of bubbles is not significantly affected by varying  $\sigma_i$ . This can also be observed in the snapshots of bubbles in figure 5.23. Figures 5.25(d), 5.25(f), and 5.25(h) show the average number of bubbles sampled based on  $C_p$  in zones 1 (near leading edge), 2 (mid section), and 3 (near trailing edge), respectively. Noticeable number of bubbles are observed in the range of  $-1 \leq C_p \leq 1$ . This is consistent with the experiments, wherein Liu and Katz (2008) predicted cavitation inception occurs at  $\sigma_i = 0.9$ . These plots also indicate presence of large number of bubbles in the low pressure region for  $\sigma_i = 0.1$  and  $0.4$ . Based on the growth ratios, these are typically larger size bubbles which get attracted toward the low pressure region.

### 5.7.6 Effect of Initial Bubble Size

The effect of initial bubble size is shown in figures 5.26. In these figures we also look at PDFs of growth ratio and  $C_p$  for cases C1, C2, and C3 over the entire region (figure 5.26a,b). The average number of bubbles sampled according to their growth ratio and  $C_p$  are also shown in three different zones (figure 5.26c-h)

Figure 5.26(a) shows that the smaller bubbles (10 micron) are less sensitive to growth. A majority of them grow to about 3-4 times their original size, whereas a very few become 100 times larger. This may be attributed to the fact that smaller bubbles tend to travel with the flow (low Stokes number), and may not get entrained into lower pressure region quickly. Larger bubbles (50 and 100 microns) can grow to very large size (10-100 times the initial size). Based on the growth ratio, 50 and 100 micron bubbles seem to be entrained in the low pressure regions in the shear layer (zones 1 and 2) and show some growth (less than twice the initial size) in these regions for  $\sigma_i = 0.4$ . Near the trailing edge, however, rapid growth in size is observed for these bubbles; some growing up to 50 times their original size. Correspondingly, they create cavities on the order of 0.5 cm also observed in the experiments.

### 5.7.7 Sampling Results Based on Growth Ratio

To further characterize the sensitivity of the bubbles to imposed pressure variations, the bubbles were sampled into three groups based on their growth ratio: small ( $d/d_{\text{initial}} < 0.8$ ), medium ( $0.8 < d/d_{\text{initial}} < 1.25$ ), and large ( $1.25 < d/d_{\text{initial}}$ ) bubbles. Bubbles from each group were then conditionally sampled to obtain PDFs and average number of bubbles based on  $C_p$  (figure 5.27) and vorticity  $\omega$  distributions (not shown). Figures 5.27a,b show that bubbles with initial size 10 micron tend to grow into medium group (i.e.  $0.8 < d/d_{\text{initial}} < 1.25$ ), whereas larger initial size bubbles (50 and 100 micron) exhibit large growth ( $1.25 < d/d_{\text{initial}}$ ). This indicates that bubbles with initial size in the range of 50-100 microns are capable predicting visible cavitation. Similar conclusions were drawn for plots based on vorticity distribution, shown in figure 5.28. This indicates that small initial size bubbles although sensitive to pressure fluctuations, do not tend to cluster in regions of high vorticity or low pressure. To predict cavitation inception, initial bubble sizes on the order of 50-100 micron are best suited for this flow

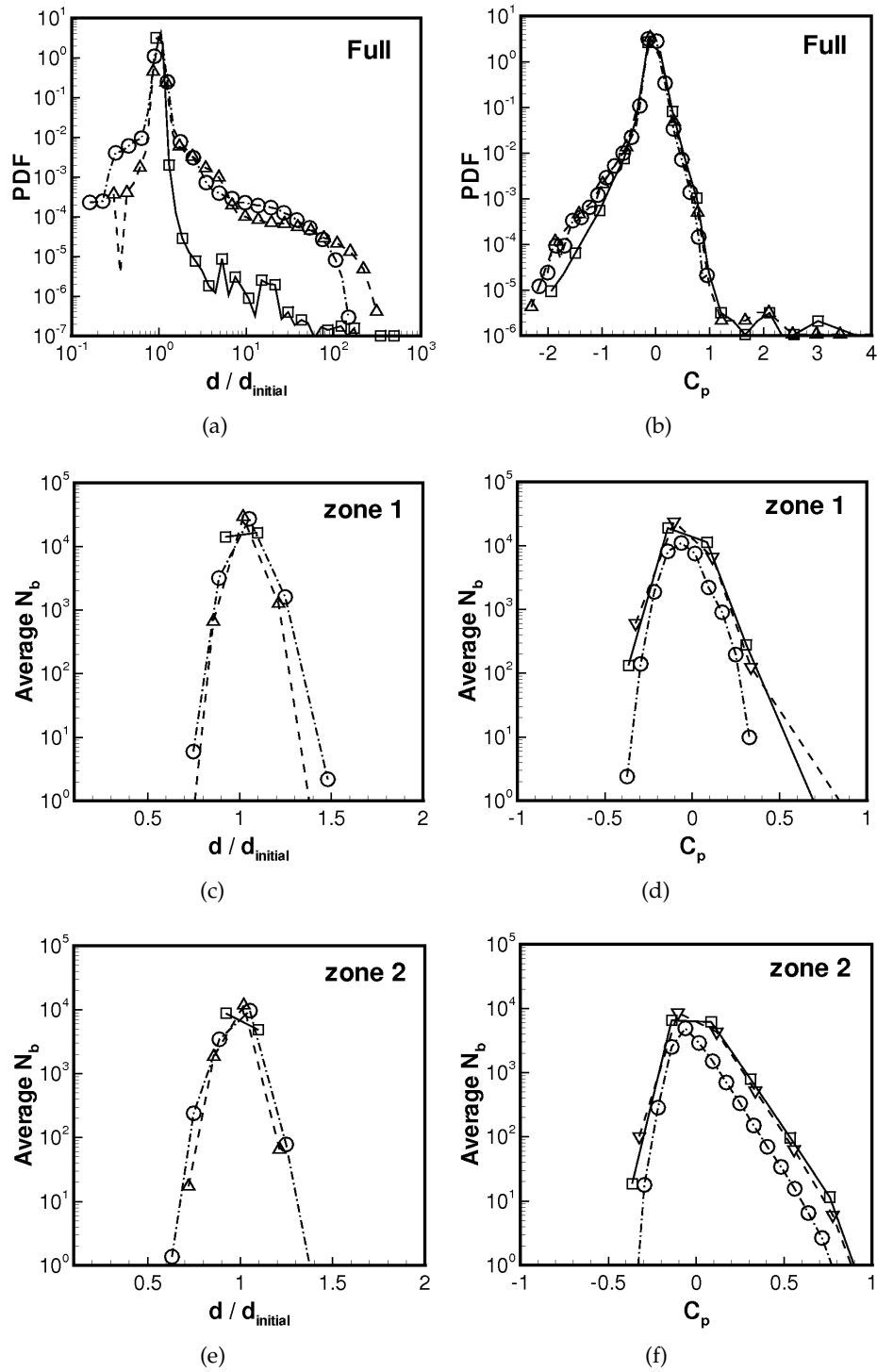


Figure 5.26: Cont'd on next page.

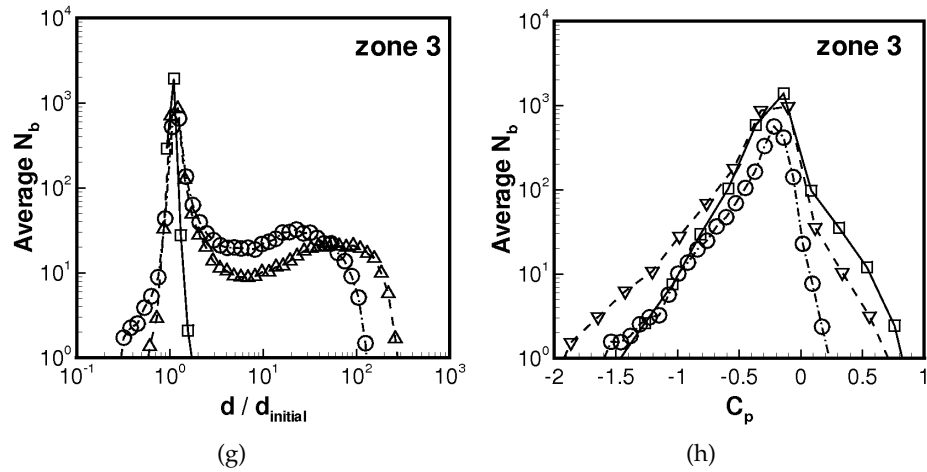


Figure 5.26: Effect of initial bubble size on the PDFs and average number of bubbles sampled based on growth ratio ( $d/d_{initial}$ ) and pressure coefficient  $C_p$  at bubble location for cases C1 (10  $\mu$ m square symbols), C2 (50  $\mu$ m triangle symbols), and C3 (100  $\mu$ m circle symbols): (a,b) PDF for all bubbles over the region of interest; (c,d) bubbles in zone 1; (e,f) bubbles in zone 2, and (g,h) bubbles in zone 3.

as they tend to cluster in low pressure regions and thus can grow to large sizes.

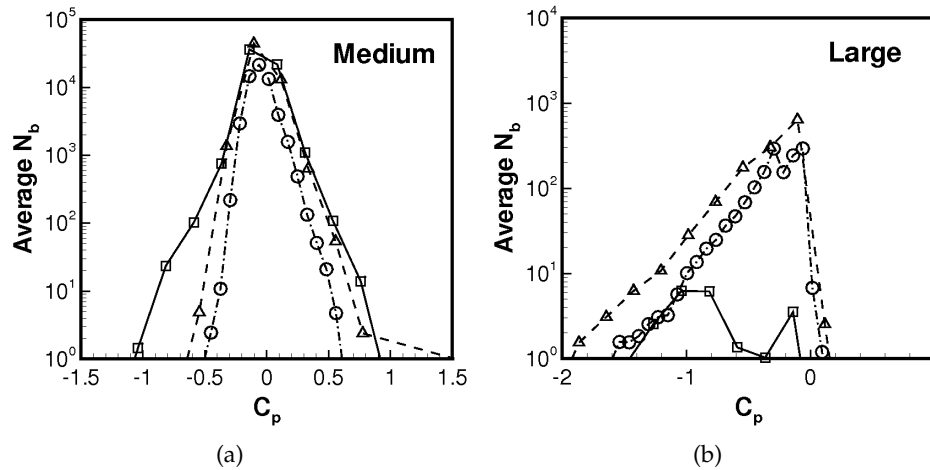


Figure 5.27: Average number of conditionally sampled bubbles based on pressure coefficient at bubble location for case C1 (square), C2 (triangle), and C3 (circle): (a) medium size group ( $0.8 < d/d_{initial} < 1.25$ ), (b) large size group ( $1.25 < d/d_{initial}$ ).

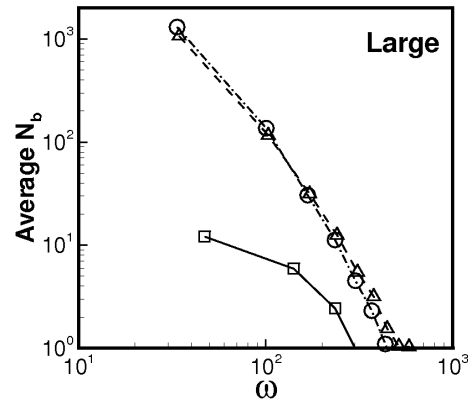


Figure 5.28: Average number of conditionally sampled bubbles for large size group ( $1.25 < d/d_{\text{initial}}$ ) based on vorticity magnitude at bubble location for case C1 (square), C2 (triangle), and C3 (circle).

## 5.8 Scalar Transport Model versus Bubble Cavitation Model

There are some fundamental differences between scalar transport model and bubble cavitation model. Cavity structures in scalar transport model is limited to the grid resolution, however, bubble cavitation model can capture the subgrid scale dynamics of cavitation. Cavitation inception is modeled in scalar transport model using the difference between local pressure and vapor pressure and actual vapor generation is modeled. Whereas, in the bubble cavitation model only the gas dynamics of the non-condensable gas is modeled using ideal gas law. Motion of bubbles and motion of the scalar field also obey different laws. Bubbles move based on the local relative velocity (in drag force), local flow acceleration (added mass force), local pressure gradient (pressure force), etc., whereas the scalar field moves passively according to the flow field.

Figure 5.29 schematically shows the difference in the instantaneous results from two different models. It is obvious how different are the behavior of the two models. There are several locations in this figure in which we can see a huge cluster of bubbles but the scalar does not show a large vapor fraction. Also bubbles do not tend to get trapped in some other regions where the scalar field shows intense cavitation.

In order to make a quantitative comparison between the behavior of two models, a new variable is defined here which is termed *expansion ratio*. It is a volume-averaged

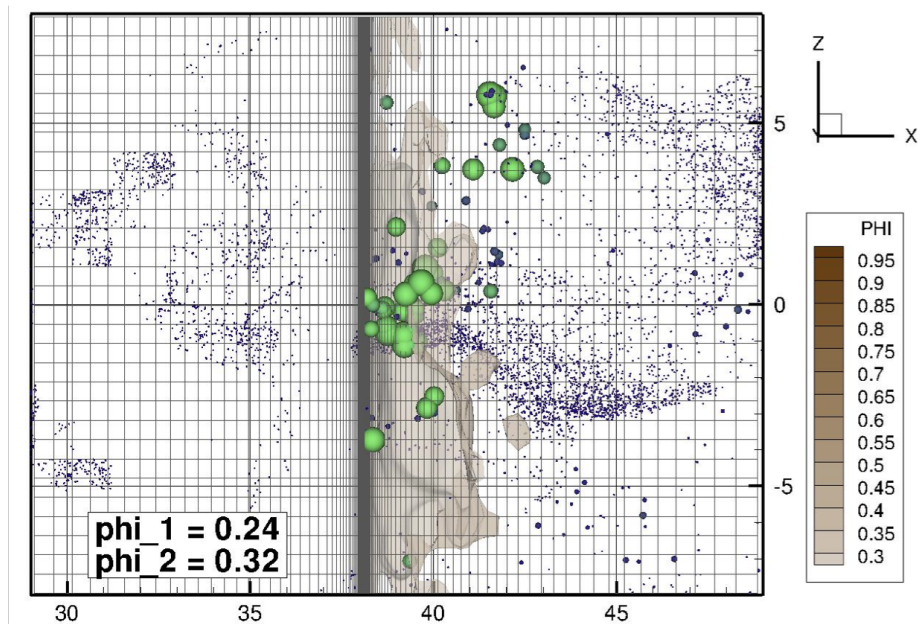


Figure 5.29: Schematic of instantaneous comparison between cavitation prediction from scalar transport model (iso surfaces of vapor fraction) and bubble cavitation model (discrete bubbles).

quantity which, is calculated in the calculation zones (defined and referred to in earlier sections). For the scalar model, expansion ratio is instantaneous volume-averaged vapor fraction at each zone. For the bubble cavitation model it is defined as the total volume of bubbles in the zone, divided by the number of bubbles and the initial bubble volume.

Figure 5.30 shows the expansion ratio signal for two models in the zones 2 and 3. It shows that in zone 2, the ratio changes to almost 5 times lower for the scalar values, but decreases for the bubbles down to almost 50 times (corresponding to 3-4 times in diameter). This shows the effect of high pressure on the shear layer close to the trailing edge. It causes the bubble volume to decrease, but the scalar does not change significantly.

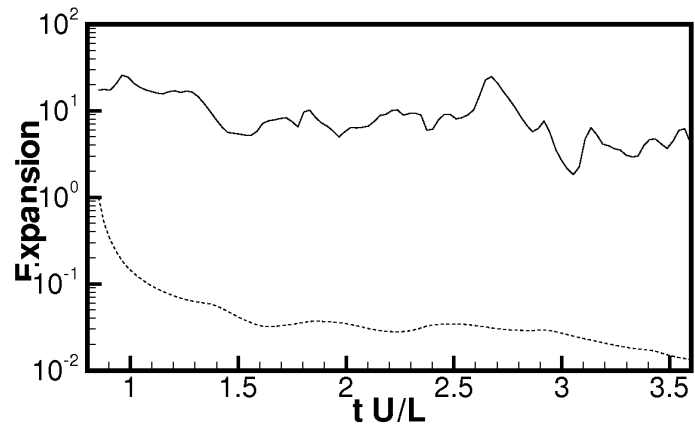
At zone 3, however, the similarities and differences are more interesting. Similar feature that is observed in this zone is the periodical behavior of both signals. They show almost the same frequency of oscillation, however, there is a phase lag in the scalar expansion ratio signal. Also the bubble signal shows more detailed variation for  $tU/L = 2.5 - 3.5$ , possibly obtained from the sub-grid dynamics of the cavitation captured by bubbles.

Similarities and differences showed in the figure, suggest that a combination of the two models could be more useful in study of cavitation. This model can more accurately predict the expansion of vapor phase (using the bubble expansion model), and also the bubble nucleation for the bubble model.

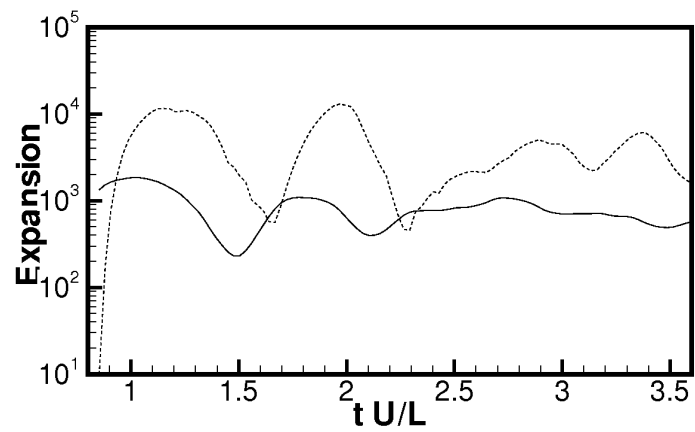
## 5.9 Summary and Conclusion

LES of turbulent flow over an open cavity is performed, corresponding to the experimental setup of Liu and Katz (2008) at the flow Reynolds number of 170,000. The filtered, incompressible Navier-Stokes equations were solved using a co-located grid finite-volume solver (Moin and Apte, 2006) with the dynamic Smagorinsky model on a five million grid with mainly Cartesian hexahedral elements. The mean flowfield at the inlet section is specified from the experimental data in the symmetry plane, whereas, turbulent fluctuations were imposed at the inflow based on resolved computation of a periodic duct flow keeping the mass-flow rate and the Reynolds number the same.

The flow statistics, including mean and rms velocity fields showed reasonable agree-



(a) zone 2



(b) zone 3

Figure 5.30: Average expansion ratio from scalar transport model (solid lines) and bubble cavitation model (dashed line).

ment with the experimental data near the leading and the trailing edges. The mean pressure distribution shows two distinct features near the trailing edge: (i) a high-pressure region just upstream of the trailing edge which extends slightly into the cavity, and (ii) a low pressure region above the trailing edge. The high pressure region just upstream of the trailing edge occurs mainly due to the impingement of the shear layer onto the trailing edge, creating a stagnation point inside the cavity. The flow then has to turn and go around the trailing edge creating a low pressure region above the trailing edge. The shape of contours of the mean  $C_p$  were very similar to those observed in the experiments and predicted that cavitation inception occurs just above the trailing edge in the low pressure region. Variations in local  $C_p$  values above the trailing edge were also investigated and showed correlations with the impingement of the shear layer vortices onto the trailing edge.

Cavitation inception was investigated using two approaches: (i) a discrete bubble model for gaseous cavitation wherein the bubble dynamics is computed by solving the Rayleigh-Plesset and the bubble motion equations using an adaptive time-stepping procedure, and (ii) a scalar transport based model for the liquid volume fraction with source and sink terms for phase change corresponding to vaporous cavitation. In both models, the effect of bubbles or vapor on the flowfield was neglected. Simulations with different values of the outside pressure were performed by changing the cavitation index ( $\sigma_i$ ). Both models predicted that inception occurs above the trailing edge. For  $\sigma_i < 0.4$ , heavy cavitation was observed above the trailing edge. The scalar transport model predicted periodic growth and decay of the liquid vapor fraction above the trailing edge owing to local variations in pressure minima. The frequency of this variation was on the order of 300 Hz similar to those observed in the experiments. The scalar transport model was also able to predict the cavitation inception on the shear layer for lowest cavitation index ( $\sigma_i = 0.1$ ). Inception on the shear layer was found to be mainly due to generation of vapor because of local pressure decrease in the flow.

The discrete bubble model captures the subgrid dynamics of bubbles and also showed cavitation inception occurring above the trailing edge. For low  $\sigma_i$ , rapid variations in bubble sizes were also observed within the shear layer. Discrete bubble model, however, could not predict large amount of cavitation within the shear layer. This is essentially due to lack of source/sink terms for the amount of gas/vapor in the bubble model. Sensitivity of the model parameters was investigated in case of the discrete

bubble model by varying the initial size of the bubbles and by changing the cavitation index. It was found that bubbles with initial sizes on the order of 50-100 micron tend to cluster in low pressure regions and exhibit rapid growth. By examining the probability distribution functions and average number of bubbles, the inception index of 0.9 agrees well with the experimental data.

## Chapter 6 – Summary, Conclusions and Future Directions

### 6.1 Summary

A numerical algorithm was developed for simulation of traveling bubble cavitation for turbulent flows in complex geometries. Filtered variable density Navier-Stokes equations are solved for the continuum liquid phase, using a co-located unstructured grid finite volume solver with dynamic Smagorinsky model (Moin and Apte, 2006). Bubble cavitation is simulated by using a discrete bubble model in Lagrangian framework. Standard models are used to account for the forces acting on bubbles. An adaptive time stepping algorithm, based on the numerical stability, is devised for the efficient solution of Rayleigh-Plesset equation to solve for the bubble size variation.

Combining accurate predictive capability of LES with cavitating discrete bubble model is the essence of this work. Commonly used Reynolds-Averaged Navier-Stokes (RANS) model for turbulence modeling in cavitation studies are known to be artificially dissipative in vortical flows (Hsiao and Pauley, 1998; Moin and Apte, 2006). Efficient and robust numerical solution of Rayleigh-Plesset equation gives a more realistic inception model than algebraic model used by Wienken et al. (2006) for LES. Accounting for subgrid scale dynamics of the cavitation by using bubble model makes more detailed studies on cavitation inception possible. Effect of gas nuclei size distribution and/or pressure fluctuations in the flow field are two examples which can not be studied using the simple inception criteria of  $C_p < -\sigma_i$  (more suitable for potential flows (Rood, 1991)).

The developed technique was verified on different test cases to show the accuracy of the method. Test cases included stationary bubbles with imposed size variation to show the volumetric effect on the flow, rising bubbles, and bubble motion in vortical flows to show the accuracy of trajectory calculation. Error analysis was presented for both fluid flow calculation and bubble trajectory calculation.

Experimental study of cavitation inception in the turbulent flow over an open cavity (Liu and Katz, 2008) was reproduced numerically as the main case study in this work.

Flow field statistics, including mean and rms of velocity and pressure was compared to those of experiment and showed well agreement. Velocity fluctuations at the inlet was reproduced from a periodical channel flow in order to account for turbulent fluctuation in the upcoming flow, more accurately. Cavitation inception was studied using discrete bubble model and scalar transport model. A parametric study was performed to study effect of parameters such as initial gas nuclei size and cavitation number  $\sigma_i$ . The main concluding remarks on this study will be presented in the following section.

## 6.2 Conclusions

Turbulent flow over cavity was accurately predicted using large eddy simulation to investigate cavitation inception. Flow unsteadiness on the leading edge, shear layer, and trailing edge of this geometry is a crucial factor in the cavitation inception. Cavitation is shown to occur near the trailing edge and on the shear layer as a results of large pressure fluctuations. These fluctuations are predicted accurately using LES approach and with minimum input from the experiment (only mean flow profile was used at the inlet). Commonly used RANS simulation techniques may not capture the essential unsteadiness and crucial pressure fluctuations on the shear layer and trailing edge zone. It has also been shown that RANS has difficulty in accurate prediction of the stagnation and separation zones, which are both present in this flow geometry. Numerical study of cavitation inception on this turbulent flow has not been performed by others before. Combining large eddy simulation with the detailed modeling of bubble cavitation in complex geometries is first being done in this study.

Two different approaches were taken to investigate cavitation inception: (i) discrete bubble model to account for gaseous cavitation, based on the bubble dynamics and bubble size variation, and (ii) scalar transport model for vaporous cavitation. Discrete bubble model account for the subgrid scale dynamics of cavitation associated with the small gas nuclei, whereas the scalar transport model accounts for the vapor generation as a function of pressure. Discrete bubble model shows the inception dynamics on the gaseous nuclei in more detailed, since it is being modeled in a Lagrangian framework. Scalar transport equations, however, are solved in the Eulerian grid and account for the vapor generation/destruction via the source terms. Detailed conclusion on both approaches are presented here.

First important conclusion in the cavitation inception studies is that the classical inception model,  $C_p < -\sigma_i$ , is not sufficient for description of inception dynamics in this flow. Discrete bubble model shows that the highest inception index is  $\sigma_i = 0.9$ . At this cavitation number, a few 50  $\mu\text{m}$  bubbles grow up to a few millimeters at the top of trailing edge (see figure 5.23). Effect of proper resolving the dynamics of the flow field fluctuations near the trailing edge, as well as the gaseous nuclei dynamics, on the inception is noticeable in this observation. Based on the classic inception criteria, inception will occur if  $C_p < -\sigma_i$ , whereas in this case  $C_p = -0.63$  on top of trailing edge and  $\sigma_i = 0.9$ . Weak cavitation with low inception frequency was observed from the scalar transport model at this cavitation index (figure 5.18).

PDF analysis showed that cavitation mainly occurs on top of the trailing edge. Parametric studies showed that larger bubbles are more susceptible to cavitation. The number of cavitating bubbles of initial size of 50  $\mu\text{m}$  and larger, was up to three orders of magnitude more than smaller ones (see figure 5.26.) Bubbles with initial size of 10  $\mu\text{m}$  almost did not show any cavitation.

The other interesting observation based on the PDF analysis was the regions in which bubbles show the largest growth rate  $d/d_{initial}$ . Figure 5.27(b) shows that the bubbles which have at least grown 25% are mostly in the negative  $C_p$  regions. More surprisingly, the majority of these bubbles are in a region with  $C_p > -0.4$  ( $\sigma = 0.4$ ).

In order to capture cavitation inception properly in the low cavitation numbers, the bubble dynamics model needs to account for the vapor generation. Experimental studies showed cavitation inception on the shear layer for,  $\sigma < 0.6$ , whereas the traveling bubble cavitation model shows only a few bubbles growing up to twice larger for  $\sigma$  as low as 0.1 (see figure 5.25). Large vapor fraction was also observed from the scalar transport model at  $\sigma < 0.4$ . The important difference between these two models is that the scalar transport model accounts for the vapor generation/destruction, whereas the bubble model does not. Hence, two important factors can be addressed in the accurate behavior of the bubble model in predicting inception: (i) opportunity of being trapped in a low pressure region, and (ii) proper initial size based on the amount of gaseous/vaporous content of the bubble.

Scalar transport model was able to show the inception dynamics near the trailing edge properly. Frequency of inception was comparable with experimental data. For low cavitation indices ( $\sigma < 0.4$ ), the inception occurs on the shear layer and it was captured

by the scalar transport model. One of the drawbacks in the scalar transport modeling is the sensitivity of the model to the model constants for source terms. Different constants are used in different studies (Senocak and Shyy, 2002a). The other issue is that the cavitation scales need to be resolved properly by the computational grid, since it is an Eulerian grid-based technique. Therefore, the small scales of cavitation was not captured by this model, as shown in the contour plots.

Both models were able to capture cavitation inception near the trailing edge. The dynamics of cavitation inception on top of the trailing edge, shown by the inception frequency, was modeled properly by both models. PDF analysis was used to show the effect of different parameters, such as cavitation index  $\sigma$  and initial diameter  $d_{init}$  on the dynamics of cavitation in discrete bubble model. Discrete bubble model shows more details and smaller scales of cavitation inception, whereas, the scalar transport model captures only larger scales based on the grid resolution. Scalar transport model could capture the cavitation inception on the shear layer, whereas discrete bubble cavitation model showed only a few bubbles growing in this region. Two possible reasons can be addressed for this: (i) bubble model does not account for the vaporous bubble generation, (ii) bubbles (initially being injected at the inlet and transported with flow) do not have enough chance of being trapped into low pressure regions on the shear layer. One remedy to this issue can be injecting bubbles at the proper location by using vapor fraction from the scalar transport model. This way, the bubbles will be injected (and removed) at the right position.

Effect of inflow conditioning on the accurate prediction of turbulent flow over cavity was addressed and investigated. The inflow fluctuations extracted from a periodic channel flow and added to the mean inflow velocity, was observed to improve the flow statistics near the leading edge. It significantly improved prediction of velocity rms, especially away from the shear layer.

### 6.3 Future Directions

It will be a great advancement over this work if discrete bubble model was coupled to a model for nucleation. One of the difficulties in using discrete bubble model for the cavitation inception studies was that the bubbles were injected at the inlet and they may not fall into the right position with the low pressure to show the cavitation inception.

This needs a long enough calculation to collect enough data at a certain point with enough number of bubbles.

The other important fact which is addressed in the previous scalar transport modeling approaches (see Senocak and Shyy (2002a) as an example), is the sensitivity of model constants for the vapor generation/destruction to the flow configuration. One suggestion is to combine the gaseous cavitation model, which accounts for the gas dynamics of nuclei, in the source terms of the scalar transport model.

Correlating cavitation from two models in this work with flow features for the turbulent flow over cavity, is suggested as the next step in this work. Some of the suggestions are correlation between pressure, vorticity, and/or flow structures to the large cavitation zones using bubbles density or volume fraction from either models.

Coupling density variations, calculated in the scalar transport model, to the governing equations, i.e. mass and momentum conservation, will be a great improvement over this work. Cavitation effect on the turbulent flow over cavity, and vortical flow structure modification, may be observed. Availability of experimental data on the cavity case will be an advantage in these studies.

## Literature Cited

- Alehossein, H. and Qin, Z. (2007). Numerical analysis of Rayleigh–Plesset equation for cavitating water jets. *Int. J. Numer. Meth. Eng.*, 72(7):780 – 807.
- Apte, S., Mahesh, K., and Lundgren, T. (2003a). A eulerian-lagrangian model to simulate two-phase/particulate flows. *Center for Turbulence Research, Annual Research Briefs*.
- Apte, S. V., Gorokhovski, M., and Moin, P. (2003b). Les of atomizing spray with stochastic modeling of secondary breakup. *Int. J. Multiphase Flow*, 29(9):1503–1522.
- Apte, S. V., Mahesh, K., and Lundgren, T. (2008). Accounting for finite-size effects in simulations of disperse particle-laden flows. *Int. J. Multiphase Flow*, 34(3):260–271.
- Apte, S. V., Mahesh, K., Moin, P., and Oefelein, J. C. (2003c). Large-eddy simulation of swirling particle-laden flows in a coaxial-jet combustor. *Int. J. Multiphase Flow*, 29(8):1311–1331.
- Arndt, R. (2002). Cavitation in vortical flows. *Annu. Rev. Fluid Mech.*, 34(1):143–175.
- Arndt, R. E. A. (1981). Cavitation in fluid machinery and hydraulic structures. *Annu. Rev. Fluid Mech.*, 13(1):273–326.
- Arndt, R. E. A., Arakeri, V. H., and Higuchi, H. (1991). Some observations of tip-vortex cavitation. *J. Fluid Mech.*, 229(-1):269–289.
- Ausoni, P., Farhat, M., Escaler, X., Egusquiza, E., and Avellan, F. (2007). Cavitation influence on von kármán vortex shedding and induced hydrofoil vibrations. *J. Fluid Eng.*, 129(8):966–973.
- Belahadji, B., Franc, J. P., and Michel, J. M. (1995). Cavitation in the rotational structures of a turbulent wake. *J. Fluid Mech.*, 287(-1):383–403.
- Blake, J. R. and Gibson, D. C. (1987). Cavitation bubbles near boundaries. *Annu. Rev. Fluid Mech.*, 19(1):99–123.
- Blake, W. K. (1986). *Mechanics of Flow Induced Sound and Vibration*, volume 1, chapter 6, pages 370–425. Academic Press.
- Brennen, C. E. (1995). *Cavitation and Bubble Dynamics*. Oxford University Press New York.
- Ceccio, S. L. and Brennen, C. E. (1991). Observations of the dynamics and acoustics of travelling bubble cavitation. *J. Fluid Mech.*, 233(-1):633–660.
- Cerutti, S., Knio, O. M., and Katz, J. (2000). Numerical study of cavitation inception in the near field of an axisymmetric jet at high reynolds number. *Phys. Fluids*, 12(10):2444–2460.
- Chahine, G., Delepoule, E., and Hauwaert, P. (1993). Study of the interaction between a bubble and a vortical structure. *ASME-PUBLICATIONS-FED*, 153:39–39.

- Chang, K., Constantinescu, G., and Park, S.-O. (2006). Analysis of the flow and mass transfer processes for the incompressible flow past an open cavity with a laminar and a fully turbulent incoming boundary layer. *J. Fluid Mech.*, 561(-1):113–145.
- Chen, Y. and Heister, S. D. (1994). A numerical treatment for attached cavitation. *J. Fluids Eng.*, 116(3):613–618.
- Cundall, P. and Strack, O. (1979). A discrete numerical model for granular assemblies. *Geotechnique*, 29(1):47–65.
- Darmana, D., Deen, N. G., and Kuipers, J. A. M. (2006). Parallelization of an euler-lagrange model using mixed domain decomposition and a mirror domain technique: Application to dispersed gas-liquid two-phase flow. *J. Comput. Phys.*, 220(1):216–248.
- Deen, N. G., van Sint Annaland, M., and Kuipers, J. A. M. (2004). Multi-scale modeling of dispersed gas-liquid two-phase flow. *Chem. Engng. Sci.*, 59(8-9):1853 – 1861. Complex Systems and Multi-scale Methodology.
- Drew, D. and Passman, S. (1999). *Theory of multicomponent fluids*. Springer New York.
- Druzhinin, O. A. and Elghobashi, S. (1998). Direct numerical simulations of bubble-laden turbulent flows using the two-fluid formulation. *Phys. Fluids*, 10(3):685–697.
- Eldredge, J., Leonard, A., and Colonius, T. (2002). A general deterministic treatment of derivatives in particle methods. *J. Comput. Phys.*, 180(2):686–709.
- Farrell, K. J. (2003). Eulerian/lagrangian analysis for the prediction of cavitation inception. *J. Fluids Eng.*, 125(1):46–52.
- Ferrante, A. and Elghobashi, S. (2005). Reynolds number effect on drag reduction in a microbubble-laden spatially developing turbulent boundary layer. *J. Fluid Mech.*, 543(-1):93–106.
- Ferrante, A. and Elghobashi, S. (2007). On the effects of microbubbles on taylor–green vortex flow. *J. Fluid Mech.*, 572:145–177.
- Germano, M., Piomelli, U., Moin, P., and Cabot, W. H. (1991). A dynamic subgrid-scale eddy viscosity model. *Phys. Fluids*, 3(7):1760–1765.
- Gidaspow, D. (1994). *Multiphase Flow and Fluidization: Continuum and Kinetic Theory Descriptions*. Academic Press.
- Gopalan, S. and Katz, J. (2000). Flow structure and modeling issues in the closure region of attached cavitation. *Phys. Fluids*, 12(4):895–911.
- Gopalan, S., Liu, H., and Katz, J. (2000). On the Flow Structure, Tip Leakage Cavitation Inception and Associated Noise. *Twenty-Third Symposium on Naval Hydrodynamics, France, September*.
- Gullbrand, J. (2000). An evaluation of a conservative fourth order DNS code in turbulent channel flow. *Center for Turbulence Research, Annual Briefs*, pages 211–18.
- Hosangadi, A. and Ahuja, V. (2005). A new unsteady model for dense cloud cavitation. In *Proceedings of FEDSM2005*.
- Hsiao, C. and Chahine, G. (2008). Numerical Study of Cavitation Inception due to

- Vortex/Vortex Interaction in a Ducted Propulsor. *Journal of Ship Research*, 52(2):114–123.
- Hsiao, C., Jain, A., and Chahine, G. (2006). Effect of Gas Diffusion on Bubble Entrainment and Dynamics around a Propeller. In *Proceedings of 26th Symp. Naval Hydrodynamics, Rome, Italy*, volume 26.
- Hsiao, C.-T. and Chahine, G. (2004). Prediction of tip vortex cavitation inception using coupled spherical and nonspherical bubble models and navier–stokes computations. *Journal of Marine Science and Technology*, 8(3):99–108.
- Hsiao, C.-T., Chahine, G. L., and Liu, H.-L. (2003). Scaling effect on prediction of cavitation inception in a line vortex flow. *J. Fluids Eng.*, 125(1):53–60.
- Hsiao, C.-T. and Pauley, L. L. (1998). Numerical study of the steady-state tip vortex flow over a finite-span hydrofoil. *J. Fluids Eng.*, 120(2):345–353.
- Hsiao, C.-T. and Pauley, L. L. (1999). Study of tip vortex cavitation inception using navier-stokes computation and bubble dynamics model. *J. Fluids Eng.*, 121(1):198–204.
- Hutter, K. and Jöhnk, K. (2004). *Continuum methods of physical modeling*. Springer.
- Jackson, R. (1997). Locally averaged equations of motion for a mixture of identical spherical particles and a newtonian fluid. *Chem. Engng. Sci.*, 52(15):2457–2469.
- Johnson, V. and Hsieh, T. (1966). The Influence of the Trajectories of Gas Nuclei on Cavitation Inception. *Sixth Symp. Naval Hydrodynamics*, pages 163–179.
- Joseph, D. D. (1995). Cavitation in a flowing liquid. *Physical Review E*, 51(3).
- Joseph, D. D. (1998). Cavitation and the state of stress in a flowing liquid. *J. Fluid Mech.*, 366(-1):367–378.
- Joseph, D. D., Lundgren, T. S., Jackson, R., and Saville, D. A. (1990). Ensemble averaged and mixture theory equations for incompressible fluid–particle suspensions. *Int. J. Multiphase Flow*, 16(1):35–42.
- Keller, A. (2001). Cavitation scale effects-empirically found relations and the correlation of cavitation number and hydrodynamic coefficients. In *CAV 2001: Fourth International Symposium on Cavitation*.
- Kermeen, R. (1956). Water tunnel tests of NACA 4412 and Walchner profile 7 hydrofoils in noncavitating and cavitating flows. *Calif. Inst. of Tech. Hydro. Lab. Rep.* 47-5.
- Kim, D. and Choi, H. (2000). A second-order time-accurate finite volume method for unsteady incompressible flow on hybrid unstructured grids. *J. Comput. Phys.*, 162(2):411–428.
- Kim, J., Paterson, E. G., and Stern, F. (2006). Rans simulation of ducted marine propulsor flow including subvisual cavitation and acoustic modeling. *J. Fluids Eng.*, 128(4):799–810.
- Kitagawa, A., Murai, Y., and Yamamoto, F. (2001). Two-way coupling of eulerian-lagrangian model for dispersed multiphase flows using filtering functions. *Int. J. Multiphase Flow*, 27(12):2129–2153.

- Knapp, R., Daily, J., and Hammit, F. (1970). *Cavitation*. McGraw-Hill New York.
- Kuipers, J. A. M., van Duin, K. J., van Beckum, F. P. H., and van Swaaij, W. P. M. (1993). Computer simulation of the hydrodynamics of a two-dimensional gas-fluidized bed. *Computers & Chemical Engineering*, 17(8):839–858.
- Kunz, R. F., Boger, D. A., Stinebring, D. R., Chyczewski, T. S., Lindau, J. W., Gibeling, H. J., Venkateswaran, S., and Govindan, T. R. (2000). A preconditioned navier-stokes method for two-phase flows with application to cavitation prediction. *Computers & Fluids*, 29(8):849–875.
- Leger, A. T. and Ceccio, S. L. (1998). Examination of the flow near the leading edge of attached cavitation. part 1. detachment of two-dimensional and axisymmetric cavities. *J. Fluid Mech.*, 376(-1):61–90.
- Lin, J. and Rockwell, D. (2001). Organized Oscillations of Initially Turbulent Flow past a Cavity. *AIAA Journal*, 39(6):1139–1151.
- Lindau, J., Kunz, R., Mulherin, J., Dreyer, J., and Stinebring, D. (2003). Fully coupled, 6-DOF to URANS, modeling of cavitating flows around a supercavitating vehicle. In *Fifth International Symposium on Cavitation*, pages 1–4.
- Liu, X. and Katz, J. (2006). Instantaneous pressure and material acceleration measurements using a four-exposure piv system. *Exp. Fluids*, 41(2):227–240.
- Liu, X. and Katz, J. (2008). Cavitation phenomena occurring due to interaction of shear layer vortices with the trailing corner of a two-dimensional open cavity. *Phys. Fluids*, 20(4).
- Luo, K., Fan, J., and Cen, K. (2007). Pressure-correlated dispersion of inertial particles in free shear flows. *Physical Review E (Statistical, Nonlinear, and Soft Matter Physics)*, 75(4):046309.
- Mahesh, K., Constantinescu, G., Apte, S., Iaccarino, G., Ham, F., and Moin, P. (2006). Large-eddy simulation of reacting turbulent flows in complex geometries. *J. Appl. Mech*, 73:374.
- Mahesh, K., Constantinescu, G., and Moin, P. (2004). A numerical method for large-eddy simulation in complex geometries. *J. Comput. Phys.*, 197(1):215–240.
- Mattson, M. and Mahesh, K. (2008). Towards numerical simulation of cavitating flows in complex geometries. *27th Symposium on Naval Hydrodynamics*.
- McDermott, R. and Pope, S. B. (2008). The parabolic edge reconstruction method (perm) for lagrangian particle advection. *J. Comput. Phys.*, 227(11):5447–5491.
- Moin, P. (2001). *Fundamentals of Engineering Numerical Analysis*. Cambridge University Press.
- Moin, P. and Apte, S. (2006). Large-Eddy Simulation of Realistic Gas Turbine-Combustors. *AIAA Journal*, 44(4):698–708.
- Moin, P., Squires, K., Cabot, W., and Lee, S. (1991). A dynamic subgrid-scale model for compressible turbulence and scalar transport. *Phys. Fluids*, 3(11):2746–2757.
- Panton, R. (2006). *Incompressible Flow*. Wiley-Interscience.

- Pereira, J. C. F. and Sousa, J. M. M. (1995). Experimental and numerical investigation of flow oscillations in a rectangular cavity. *Journal of Fluids Engineering*, 117(1):68–74.
- Pierce, C. and Moin, P. (1998). Large eddy simulation of a confined coaxial jet with swirl and heat release. In *AIAA, Fluid Dynamics Conference, 29 th, Albuquerque, NM*.
- Pierce, C. D. and Moin, P. (2004). Progress-variable approach for large-eddy simulation of non-premixed turbulent combustion. *J. Fluid Mech.*, 504(-1):73–97.
- Plesset, M. (1949). The dynamics of cavitation bubbles. *J. Appl. Mech*, 16(3):227–282.
- Plesset, M. and Prosperetti, A. (1977). Bubble dynamics and cavitation. *Annu. Rev. Fluid Mech.*, 9(1):145–185.
- Rayleigh, L. (1917). On the pressure developed in a liquid during the collapse of a spherical cavity. *Phil. Mag*, 34:94–98.
- Rood, E. P. (1991). Review—mechanisms of cavitation inception. *J. Fluids Eng.*, 113(2):163–175.
- Senocak, I. and Shyy, W. (2002a). Evaluation of Cavitation Models for Navier-Stokes Computations. *FEDSM2002-31011, Proc. of 2002 ASME Fluids Engineering Division Summer Meeting Montreal, CA*.
- Senocak, I. and Shyy, W. (2002b). A pressure-based method for turbulent cavitating flow computations. *J. Comput. Phys.*, 176(2):363–383.
- Senocak, I. and Shyy, W. (2004). Interfacial dynamics-based modelling of turbulent cavitating flows, part-1: Model development and steady-state computations. *Int. J. Numer. Meth. Fluids*, 44:975–995.
- Snider, D. M. (2001). An incompressible three-dimensional multiphase particle-in-cell model for dense particle flows. *J. Comput. Phys.*, 170(2):523–549.
- Sridhar, G. and Katz, J. (1999). Effect of entrained bubbles on the structure of vortex rings. *J. Fluid Mech.*, 397(-1):171–202.
- Thoroddsen, S. T., Etoh, T. G., and Takehara, K. (2008). High-speed imaging of drops and bubbles. *Annu. Rev. Fluid Mech.*, 40(1):257–285.
- Tseng, C.-C. and Shyy, W. (2009). Modeling for isothermal and cryogenic cavitation. *International Journal of Heat and Mass Transfer*.
- Tsuji, Y., Kawaguchi, T., and Tanaka, T. (1993). Discrete particle simulation of two-dimensional fluidized bed. *Powder technology*, 77(1):79–87.
- Wang, G., Senocak, I., Shyy, W., Ikohagi, T., and Cao, S. (2001). Dynamics of attached turbulent cavitating flows. *Progress in Aerospace Sciences*, 37(6):551–581.
- Wienken, W., Stiller, J., and Keller, A. (2006). A method to predict cavitation inception using large-eddy simulation and its application to the flow past a square cylinder. *J. Fluids Eng.*, 128(2):316–325.
- Wosnik, M., Schauer, T., and Arndt, R. (2003). Experimental study of a ventilated super-cavitating vehicle. In *Fifth International Symposium on Cavitation (CAV2003). Osaka, Japan*.

